12-2015

Interface and Morphology Engineering in Solution-Processed Electronic and Optoelectronic Devices

Sanjib Das
University of Tennessee - Knoxville, sdas8@vols.utk.edu

To the Graduate Council:

I am submitting herewith a dissertation written by Sanjib Das entitled "Interface and Morphology Engineering in Solution-Processed Electronic and Optoelectronic Devices." I have examined the final electronic copy of this dissertation for form and content and recommend that it be accepted in partial fulfillment of the requirements for the degree of Doctor of Philosophy, with a major in Electrical Engineering.

Gong Gu, Major Professor

We have read this dissertation and recommend its acceptance:

Kai Xiao, Syed K. Islam, Jayne Wu, Ramakrishnan Kalyanaraman

Accepted for the Council:

Carolyn R. Hodges

Vice Provost and Dean of the Graduate School

(Original signatures are on file with official student records.)

Interface and Morphology Engineering in Solution-Processed Electronic and Optoelectronic Devices

A Dissertation Presented for the
Doctor of Philosophy
Degree
The University of Tennessee, Knoxville

Sanjib Das

December 2015

Dedication

This dissertation is dedicated to -

My better half

Apy Das

My parents

Kajal Das & Shikha Das

My brothers

Raju Das & Jishu Das

Acknowledgements

This dissertation would not have been possible without the help of so many people. First of all, I would like to express my gratitude to my major advisor, Dr. Gong Gu, for giving me the opportunity to work with him. I thank him for his guidance and encouragement, and for showing me a broader perspective of scientific research. He spent a significant amount of his time discussing my research results, academic progress, and scientific writings. I would also like to acknowledge his financial support.

I would like to thank my co-advisor, Dr. Kai Xiao from Center for Nanophase Materials Sciences (CNMS) at Oak Ridge National Laboratory (ORNL), for his constant guidance and supervision during my PhD research works. He provided me the laboratory supports for doing experiments in one of the leading national laboratories in USA. Next, I am grateful to Dr. Pooran Joshi from Materials Science and Technology Division at ORNL for his financial support, and excellent collaboration and insightful discussion.

Special thanks go to my PhD committee members, Dr. Syed K. Islam, Dr. Jayne Wu, and Dr. Ramakrishnan Kalyanaraman for spending their valuable time and giving me important suggestions on my dissertation. I would like to thank –

- – Dr. Jong Keum from ORNL for his excellent collaboration and important scientific discussion,
- – Dr. David Geohegan from ORNL for his valuable suggestions and discussions,
- – Dr. Christopher Rouleau from ORNL for all his technical helps,
- – Dr. Ilia Ivanov and Dr. Jihua Chen from ORNL for their nice collaboration,

Abstract

The first part of this dissertation focuses on interface and morphology engineering in polymer- and small molecule-based organic solar cells. High-performance devices were fabricated, and the device performance was correlated with nanoscale structures using various electrical, spectroscopic and microscopic characterization techniques, providing guidelines for high-efficiency cell design.

The second part focuses on perovskite solar cells (PSCs), an emerging photovoltaic technology with skyrocketing rise in power conversion efficiency (PCE) and currently showing comparable PCEs with those of existing thin film photovoltaic technologies such as CIGS and CdTe. Fabrication of large-area PSCs without compromising reproducibility and device PCE requires formation of dense, pinhole-free and highly uniform perovskite thin films over large area, which remains a big challenge as of today. In this work, a scalable process, called ultrasonic spray-coating (USC), was thoroughly optimized to deposit dense and uniform perovskite thin films for high-efficiency PSCs. In order to realize high-performance flexible PSCs, a unique photonic curing technique was demonstrated to achieve highly conductive TiO_2 as electron transport layer on flexible substrates. Moreover, the effect of processing conditions on perovskite film growth was evaluated and taken into account to increase PCE to more than 15%.

In addition, a series of high-performance organic field-effect transistors (OFETs) were fabricated en route to demonstrate the versatility of the USC process. Several different polymer binders were used to modulate the lateral and vertical phase morphologies in OFETs, significantly improving the device performance.

In summary, this research provides guidelines for the design and fabrication of high-performance solution-processed solar cells and field-effect transistors based on organic materials and hybrid perovskites, while presenting a viable route for large-scale fabrication.

Table of Contents

List of Tables

List of Figures

List of Symbols and Abbreviations

λ	Wavelength
A	Area
AM	Air Mass
AFM	Atomic Force Microscopy
BG/TC	Bottom Gate/Top Contact
CB	Chlorobenzene
C_i	Gate Capacitance
DCB/oDCB	1,2-dichlorobenzene
DIO	1,8-diiodooctane
DMF	N,N-Dimethylformamide
DMSO	Dimethyl Sulfoxide
DSSC	Dye-Sensitized Solar Cell
EA	Electron Acceptor
ED	Electron Donor
E_g	Bandgap
EQE	External Quantum Efficiency
ETL	Electron Transport Layer
FB	Forward Bias
FIB	Focused ion beam
FF	Fill Factor
GIWAXS	Grazing Incidence Wide-Angle X-ray Scattering
GIXD	Grazing Incidence X-ray Diffraction

h	Planck's Constant (6.626×10^{-34} J·s)
HOMO	Highest Occupied Molecular Orbital
HTL	Hole Transport Layer
I	Current
I_0	Reverse Saturation Current
I_{DS}	Drain-Source Current
I_L	Photocurrent
IPA	Isopropyl Alcohol
IQE	Internal Quantum Efficiency
I_{SC}	Short-Circuit Current
ITO	Indium Tin Oxide
J	Current Density
J_0	Reverse Saturation Current Density
J_L	Photocurrent Density
J_{SC}	Short-Circuit Current Density
k	Boltzmann Constant ($8.617 \times 10\text{-}5$ eV/K)
LUMO	Lowest Unoccupied Molecular Orbital
MAI	Methylammonium Iodide
M_w	Molecular Weight
n	Diode Ideality Factor
NR	Neutron Reflectometry/Reflectivity
OFET	Organic Field-Effect Transistor
OSC	Organic Solar Cell
P	Power

PC$_{71}$BM	[6,6]-phenyl C$_{71}$ butyric acid methyl ester
PCBM/PC$_{61}$BM	[6,6]-phenyl C$_{61}$ butyric acid methyl ester
PCE	Power Conversion Efficiency
p-DTS(FBTTh$_2$)$_2$	7,7′ -[4,4-bis (2-ethylhexyl)-4H-silolo[3,2-b:4,5-b′]dithiophene-2,6-diyl] bis[6-fluoro-4-(5′ -hexyl-[2,2′ -bithiophen]-5-yl)benzo[c][1,2,5]thiadiazole])
PEDOT:PSS	Poly(3,4-ethylenedioxythiophene):poly(styrenesulfonate acid)
PET	Polyethylene Terephthalate
PL	Photoluminescence
PFN	Poly-[(9,9-bis(3′-(N,N-dimethylamino)propyl)-2,7-fluorene)-alt-2,7-(9,9–dioctylfluorene)]
PTB7	Poly[thieno[3,4-*b*]thiophene/benzodithiophene]
PTP	Pulse-Thermal Processing
PVP	Poly-4-vinylphenol
R2R	Roll-to-Roll
RB	Reverse Bias
RMS	Room-Mean-Square
R_P	Shunt Resistance
R_S	Series Resistance
SANS	Small-Angle Neutron Scattering
SAXS	Small-Angle X-ray Scattering
SC	Short Circuit
SEM	Scanning Electron Microscopy
SLD	Scattering Length Density
Spiro-OMeTAD	2,2′,7,7′-tetrakis-(N,N-di-pmethoxyphenylamine) 9,9′-spirobifluorene

T	Temperature
TEM	Transmission Electron Microscopy
TIPS-PEN	6,13-bis(trisopropyl-silylethynyl) Pentacene
USC	Ultrasonic Spray-Coating
V	Voltage
V_{DS}	Drain-Source Voltage
V_{GS}	Gate-Source Voltage
V_{OC}	Open-Circuit Voltage

Chapter 1: Introduction

1.1 Research Motivation

The world is experiencing increasing energy demand every day, due to population growth, technology revolution, industry, etc. If we have a look at the energy scenario in USA, in only 2013, the total generated electricity was about 4,058 billion kilowatthours (kWh) as reported by U.S. Energy Information Administration [1]. The energy sources and percent share of total electricity generation were coal 39%, natural gas 27%, nuclear 19%, hydropower 7%, other renewable 6% (biomass 1.48%, geothermal 0.41%, solar 0.23%, wind 4.13%), petroleum 1%, and other gases < 1%. As can be seen, about 67% of the total electricity was generated from fossil fuel (coal, natural gas, and petroleum), with 39% attributed to coal. Apparently, the demand for electricity is going to increase significantly in coming years, and to meet this demand, we need more clean energy-generating sources. Because it is well known that using fossil fuels to produce electricity has many drastic effects on our environment and climate change. For example, carbon emission − a byproduct − is one of the major causes for global warming. That is why many countries are now trying to reduce the dependence on fossil fuels in generating electricity. For instance, in the same year, the gross electric power generation in Germany totaled 631 billion kWh [2]. Although major proportion of the electricity was still generated using lignite (25.5%), hard coal (19.4%), and natural gas (10.6%), renewable sources (wind, water, biomass, photovoltaic) accounted for a significant amount (24.1%) of the total generated electricity.

An alternative to fossil fuel is renewable energy sources, which are naturally replenished. One of the most promising, affordable, inexhaustible, and clean renewable sources is the naturally abundant sunlight. Photovoltaic technology, used to convert sunlight to electricity, is environmentally safe, and can be set up off-grid anywhere in the world that has access to sunlight, without worrying about the national grid.

The effectiveness and vast deployment of a solar power generation or photovoltaic technology, however, depend on the economics, i.e., associated costs for power generation. Based on the efficiency and associated cost/W_p, photovoltaic technologies are usually divided into three categories, as shown in **Figure 1.1**. The first generation technologies include mono- and multi-crystalline silicon (Si) based solar cells, which have power conversion efficiencies (PCEs) in the range of ~25%. Si solar cells dominate the market today, with almost 80-90% of total market share, due to their high performance and excellent stability. But as the used Si must be ultra-pure (99.9999%), the associated processing costs are very high. To reduce the production cost, second generation or thin film photovoltaic technologies such as amorphous Si (a-Si) [3-5], copper indium gallium (di)selenide (CIGS) [6,7], and cadmium telluride (CdTe) [8,9] were developed. One of the advantages of these technologies is their lower costs due to the fact that they don't require expensive Si wafers and material consumption is comparatively low. However, their main drawback is their lower PCEs (~ 15-20%) compared to first generation solar cells. In addition, both the first and second generation PV technologies suffer from a fundamental efficiency limit, called Shockley-Quiesser limit [10], describing the fact that the maximum achievable PCE from a single-junction solar cell is 33.7% assuming a bandgap of 1.34 eV. In order to circumvent this limit and reduce manufacturing cost, third generation

technologies and ideas such as organic solar cells (OSCs) [11], multi-junction/tandem solar cells [12], dye-sensitized solar cells (DSSCs) [13,14], multi-exciton generation [15], and quantum dot based solar cells [16] were developed. Finally, the most recent addition to the family of PV technologies is the emerging perovskite solar cells (PSCs).
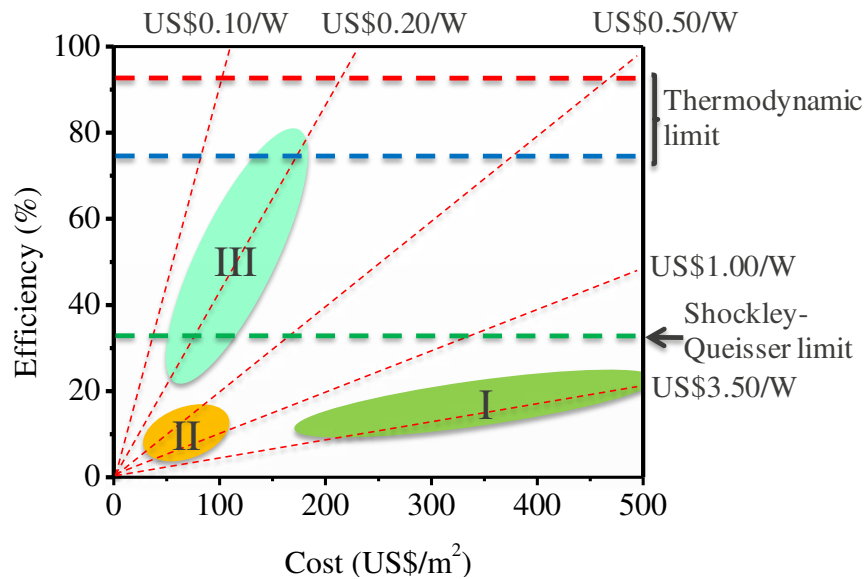
Figure 1.1. Classification of solar cell technologies based on efficiency and per unit cost. The per unit prices shown in the figure are just for comparison. Absolute per unit manufacturing cost and market price have significantly decreased over the last several years.

Due to some notable advantages such as abundance of materials, ease of fabrication, compatibility with fast and inexpensive large-scale fabrication, OSCs and PSCs are the two most promising new-generation technologies. **Figure 1.2** illustrates how the PCEs of these two technologies have evolved compared with other leading thin film technologies such as CIGS, CdTe, and a-Si. As can be seen, over the last decade, the PCE of single-junction OSCs has gradually reached to more than 10%, which is often considered as the manufacturing threshold. PSCs, in comparison, witnessed a very rapid increase in PCEs within a few years. In 2009, when

perovskite materials were used for the first time in photovoltaic devices, the PCE was less than 4% [17]. By the end of 2014, the reported PCE reached ca. 17% [18], and now, the certified PCE is 20.1% [19], which is comparable to that of the dominant silicon solar cells. Though these two technologies experience significant increase in performances, there are some critical issues such as poor stability, presence of environmentally hazardous lead (Pb) and hysteresis in PSCs, etc. that need to be addressed before their large scale production.
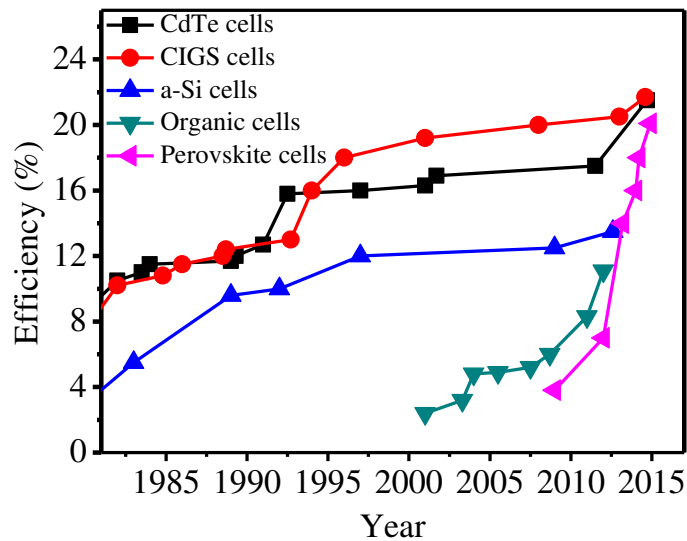
Figure 1.2. Evolution of solar cell efficiencies in different photovoltaic technologies. Data are taken from National Renewable Energy Laboratory efficiency chart [19].

1.2 Solar Cell Working Principle

This section illustrates the basic concept of how a solar cell works. Basically, when the sunlight falls on a cell, the light absorbing layer in the cell absorbs the light, and the incident photons create electron-hole pairs, called excitons. Afterwards, the electrons and holes are separated by

internal electric field between junctions. Under dark conditions, the cell behaves like a diode, and its characteristics can be expressed by the following equation [20]:

$$I = I_0(e^{\frac{qV}{nkT}} - 1)$$

(1.1)

where, I = output current; I_0 = reverse saturation current through diode, q = elementary charge; V = bias (V); n = diode ideality factor (1 for an ideal diode); k = Boltzmann constant $(8.617 \times 10^{-5}$ eV/K); T = absolute temperature (K); and at 25 °C, $kT/q \approx 0.0259$ V.
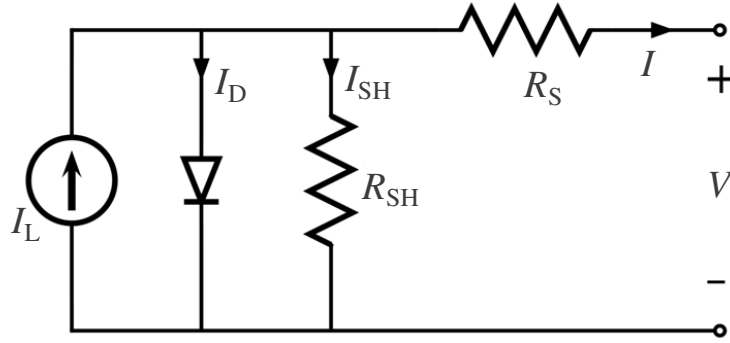
Figure 1.3. Equivalent circuit of a solar cell under illumination.

Under illumination, the solar cell can be modeled as the equivalent circuit shown in **Figure 1.3** [21], and the output current from the cell can be expressed by the following equation:

$$I = I_L - I_0 \left(e^{\frac{q(V+IR_S)}{nkT}} - 1 \right) - \frac{V+IR_S}{R_{SH}}$$

(1.2)

where, R_S is the series resistance due to contacts and junctions, and R_{SH} is the shunt or parallel resistance due to leakage current through the cell.

Taking the cell area into the consideration, the equation can be modified as-

$$J = J_L - J_0 \left(e^{\frac{q(V+JR_S)}{nkT}} - 1 \right) - \frac{V+JR_S}{R_{SH}}$$

(1.3)

where, J denotes current density. The current density and output power of a typical solar cell in the region of power generation are shown in **Figure 1.4**. Here, negative power indicates power generation. The output power of an operating solar cell, P_{out} is

$$P_{out} = V_{OC}J_{SC}FF \tag{1.4}$$

where, V_{OC} is the open circuit voltage of the cell. At V_{OC}, no power is generated, and it directly depends on the bandgap of the absorbing material and the work function difference between the electrodes. J_{SC} is the short-circuit current density of the cell, and no power is generated at J_{SC} either. J_{SC} highly depends on how strongly light is absorbed, i.e., higher J_{SC} corresponds to higher photocurrent generated by the cell. Third important parameter is the fill factor (FF), which indicates the sharpness of the *J-V* curve. It is defined by the ratio of $V_{max}J_{max}$ and $V_{OC}J_{SC}$. Due to the diode-like behavior, the FF of a solar cell is always less than one. In an ideal cell, FF is very high due to very small R_S (≈ 0 Ω) and very high R_{SH} ($\approx \infty$). However, in reality, every solar cell has a small but nonzero R_S and large but finite R_{SH}.
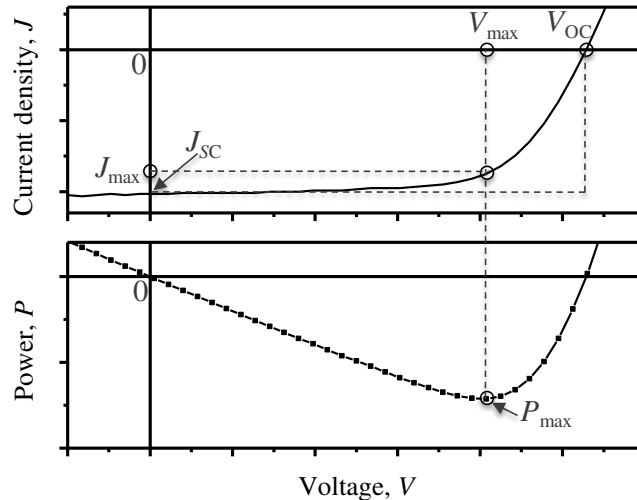
Figure 1.4. Variation of current density and power with voltage in a typical solar cell.

The evaluation of a solar cell's performance is measured by its power conversion efficiency (PCE), which is expressed as-

$$PCE = \frac{P_{out}}{P_{in}} = \frac{V_{OC} J_{SC} FF}{P_{in}} \tag{1.5}$$

where, P_{in} is the incident power and depends on atmosphere. Three different standard solar irradiance spectra are used to measure solar cell performance depending on applications, defined by American Society for Testing and Materials (ASTM), as illustrated in **Figure 1.5** [22]. Air mass 0 (AM 0) is used to measure solar cells used in space applications. The total integrated power for this spectrum is 136.7 mW/cm^2.

Solar cells used in different parts of the world are evaluated based on AM 1.5 Global (G) spectrum, which corresponds to solar radiation incident at an angle of 48° relative to the surface normal, and has an integrated power density of 100 mW/cm^2 [23]. AM 1.5G includes both direct (D) and diffuse radiation, whereas AM 1.5D includes only the direct radiation.
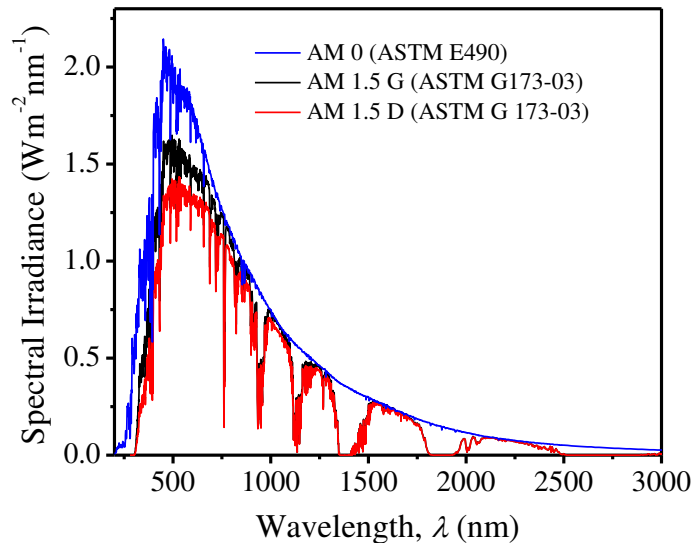
Figure 1.5. ASTM terrestrial reference spectra used for photovoltaic performance evaluation.

1.3 Research Goals and Dissertation Layout

This dissertation mainly focuses on organic and perovskite solar cells (OSCs and PSCs). In order to give an idea of the recent advances, Chapter 2 covers an in-depth literature review on these two fields. The first part of this dissertation focuses on interface and morphology engineering in various polymer- and small molecule-based organic solar cells (OSCs). In Chapter 3, the higher PCEs for inverted organic solar cells (i-OSCs) compared to c-OSCs for a well-established polymer-fullerene bulk-heterojunction system is investigated by correlating the device performance to nanoscale structures using a variety of state-of-the-art characterization techniques including neutron reflectometry (NR), transmission electron microscopy (TEM), small-angle neutron scattering (SANS), and grazing incident wide-angle X-ray scattering (GIWAXS).

In Chapter 4, the effects of processing additive and annealing temperatures on active layer film morphologies and resulting device performance in a high-performing small molecule-based bulk-heterojunction OSCs are demonstrated.

The second part of the dissertation focuses on the design, fabrication, and characterization of high-performance PSCs. In Chapter 5, high-efficiency PSCs were fabricated on glass and flexible substrates using various deposition techniques including scalable ultrasonic spray-coating (USC). A unique rapid thermal annealing technique, called photonic curing, was demonstrated to sinter solgel-deposited electron-transporting TiO_2 films on polyethylene terephthalate (PET) substrates to realize high-efficiency flexible PSCs.

In Chapter 6, the photonic curing was further optimized to sinter TiO_2 films on both glass and flexible substrates. In addition, the effects of various extrinsic and intrinsic parameters on perovskite film growth and device performance are evaluated and discussed.

In order to demonstrate the versatility of the scalable USC technique, a series of high-performance organic field-effect transistors were fabricated with both semiconducting/active and dielectric layers spray-coated, as described in Chapter 7. A well-studied small molecule was used for the active layer, and a polymer was used as dielectric layer to realize devices both on rigid and flexible substrates. Three different derivatives of polystyrene insulating polymer were used to control the crystal growth and orientation of the semiconducting small molecules (Chapter 8), significantly enhancing the device performance.

Finally, Chapter 9 draws the conclusion and emphasizes on scopes for future research and development.

Chapter 2: Literature Review - Organic and Perovskite Solar Cells

2.1 Organic Solar Cells

Organic solar cells (OSCs) have a long history. The oldest type of OSCs used to have a single semiconducting polymer sandwiched between two electrodes - indium tin oxide (ITO) with high work function and aluminum (Al) with low work function, as shown in **Figure 2.1**a. But in practice, these solar cells do not work well as the photoexcited electron remains bound to the created hole in valence band, and they behave like an exciton. Due to the exciton's charge neutrality, it does not drift with electric field, and eventually recombines without being collected.
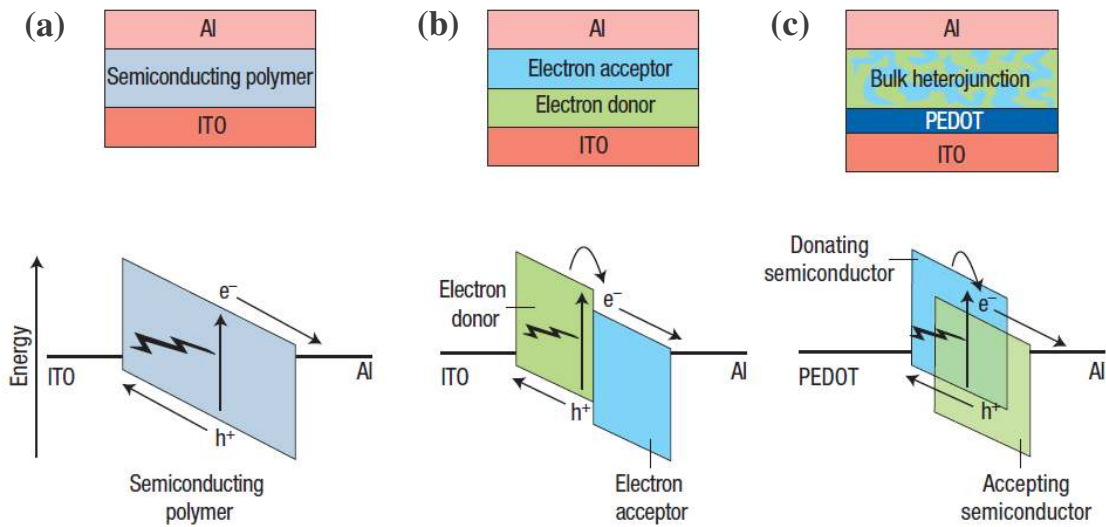
Figure 2.1. a) A single-layer semiconductor-polymer solar cell. b) A planar heterojunction cell. c) A bulk heterojunction solar cell with a hole transport layer [24].

To circumvent this problem, a second semiconductor with electron accepting nature and low-energy conduction band was used, as illustrated in Figure 2.1b. C. W. Tang reported a two-layer or planar heterojunction solar cell with a PCE as high as ~1% under AM2 illumination in 1986,

where he used copper phthalocyanine (CuPc) as the electron donor and a perylene tetracarboxylic derivative (PV) as the electron acceptor in the ITO/CuPc/PV/Ag architecture [25]. In 2001, a PCE of 3.6% was achieved with some modification to this planar heterojunction architecture, where a hole transport layer (HTL), poly(3,4-ethylenedioxylenethiophene): poly(styrenesulphonic acid) (PEDOT:PSS) was used between donor and anode, an electron transport layer (ETL), bathocuproine (BCP) was used between the acceptor and metal cathode, and fullerene (C_{60}) was used as electron acceptor [26]. One of the biggest concerns with planar heterojunction OSCs is that due to extremely short exciton diffusion length (~ 10 nm) in the used absorber materials, electrons and holes recombine before reaching the electrodes. As a result, the active layer needs to be very thin, thus reducing the light absorption, leading to lower efficiency.
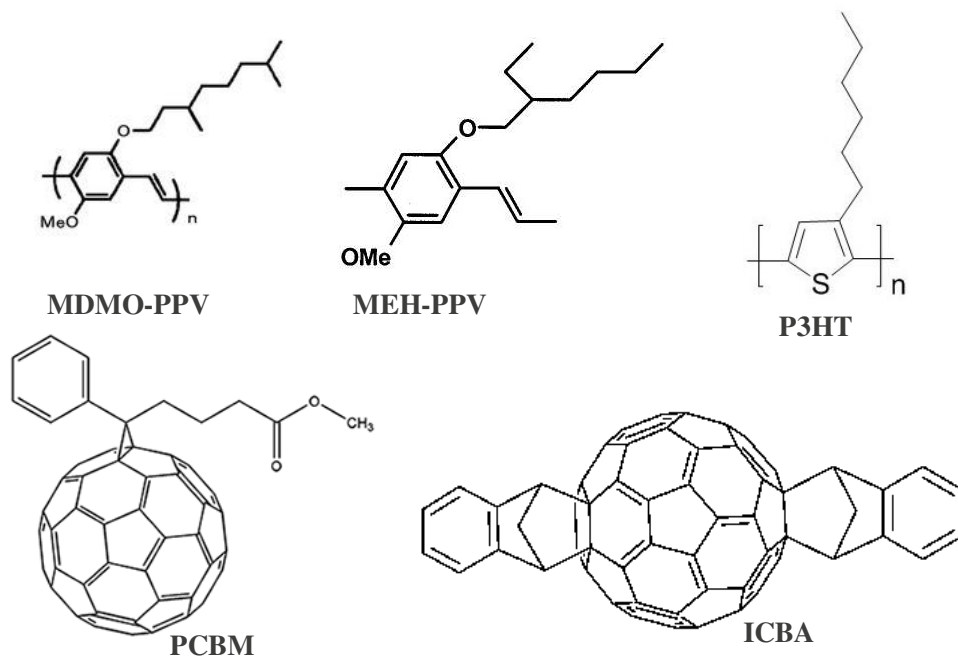
Figure 2.2. Chemical structures commonly used high-bandgap donor polymers (top row) and two mostly used fullerene derivatives (bottom row).

11

In order to avoid this problem, the idea of bulk-heterojunction (BHJ) was proposed in 1993 [27], where both the donor polymer and acceptor fullerene are dissolved in a common solvent and spun-cast, forming a bi-continuous inter-penetrating network, facilitating the charge transport (Figure 2.1c). In 2001, Shaheen et al. reported a PCE of 2.5% under AM 1.5G illumination using a BHJ of poly[2-methoxy-5-(3',7'-dimethyloctyloxy)]-1,4-phenylenevinylene) (MDMO-PPV) (**Figure 2**) and [6,6]-phenyl-C_{61}-butyric acid methyl ester (PCBM of $PC_{61}BM$) blend film incorporated into the ITO/PEDOT:PSS (80 nm)/MDMO-PPV:PCBM (100 nm)/LiF (0.6 nm)/Al (80 nm) architecture [28]. Later on, another donor polymer with similar bandgap, poly[2-methoxy-5-(2-ethylhexyloxy)-1,4-phenylenevinylene] (MEH-PPV, E_g = 2.3 eV) yielded a PCE of ~ 3% when blended with PCBM in BHJ cells [29]. However, due to the rather large bandgap (~2.2-2.3 eV) and low mobility of PPP-based polymers, efficiencies remained at a maximum of ~ 3%.

Poly-3(hexylthiophene) (P3HT) was the next dominant donor polymer in OPV research, which, blended with PCBM, led to improved PCE. This is due to its relatively lower bandgap (~2.0 eV), increasing the absorption in the visible range and its higher mobility. Schilinsky et al. reported the first encouraging results on P3HT:PCBM solar cells in 2002, with a PCE of 2.8% [30]. Over the next couple of years, huge research efforts were expended on improving the performance of P3HT:PCBM OSCs. Morphology engineering of the active layer by thermal annealing [31-33], solvent vapor annealing [34,35], and bilayer inter-diffusion [36,37], and the use of various hole transport layers [38] led to PCEs of more than 5%. However, due to PCBM's lower lowest unoccupied molecular orbital (LUMO), the open circuit voltage (V_{OC}) in these solar cells is relatively low – in the range 0.55-0.65 V. To increase the efficiency further, it is very

important to have higher V_{OC}. One easier way to increase V_{OC} is to move up the LUMO level in fullerene derivative. For example, using indene–C_{60} bisadduct (ICBA) instead of PCBM increased the V_{OC} by ~ 0.2V and PCE to more than 6% [39,40]. Another way of increasing PCE in P3HT:PCBM solar cells is adding a processing additive to P3HT:PCBM solution, which enhances the P3HT hole mobility, and charge-carrier lifetimes [41].

Most of the earlier high-efficiency P3HT:PCBM solar cells incorporated PEDOT:PSS on top of indium tin oxide (ITO) as hole transport layer, and low work function metals such as Al as the top electrode in ITO/PEDOT:PSS/P3HT:PCBM/Ca or BCP or LiF/Al architecture, also known as regular architecture. Both these materials are highly reactive with moisture, and hence quickly degrade the device performance. To overcome this issue, an alternative architecture, also called inverted architecture – ITO/ETL/P3HT:PCBM/HTL/electrode – was developed where, a metal oxide such as ZnO, TiO_2, aluminum doped zinc oxide (AZO) or Cs_2CO_3 is coated on top of ITO as ETL, molybdenum (III) oxide (MoO_3) or vanadium (V) oxide (V_2O_5) is used as HTL, and a high work function metal such as Ag or Au is used as the top electrode [42-45]. Incorporating inverted device architecture led to the realization of highly stable OSCs.

Another way to increase the device efficiency is bandgap engineering. For instance, if the highest occupied molecular orbital (HOMO) of the conjugated donor polymer can be moved down while keeping the bandgap fixed, the V_{OC} can be increased. Using poly[N-9′-hepta-decanyl-2,7-carbazole-alt-5,5-(4′,7′-di-2-thienyl-2′,1′,3′-benzothiadiazole)] (PCDTBT, **Figure 2.3**) conjugated polymer with [6,6]-phenyl C_{71}-butyric acid methyl ester ($PC_{71}BM$) can yield PCE as high as 7% [46-48]. Here, it should be noted that $PC_{71}BM$ has higher absorption than $PC_{61}BM$ in the visible range [49]. The low absorption of $PC_{61}BM$ can be attributed to its high

degree of symmetry, whereas $PC_{71}BM$ is less symmetric, making the lowest-transitions easier and dramatically enhancing the light absorption.
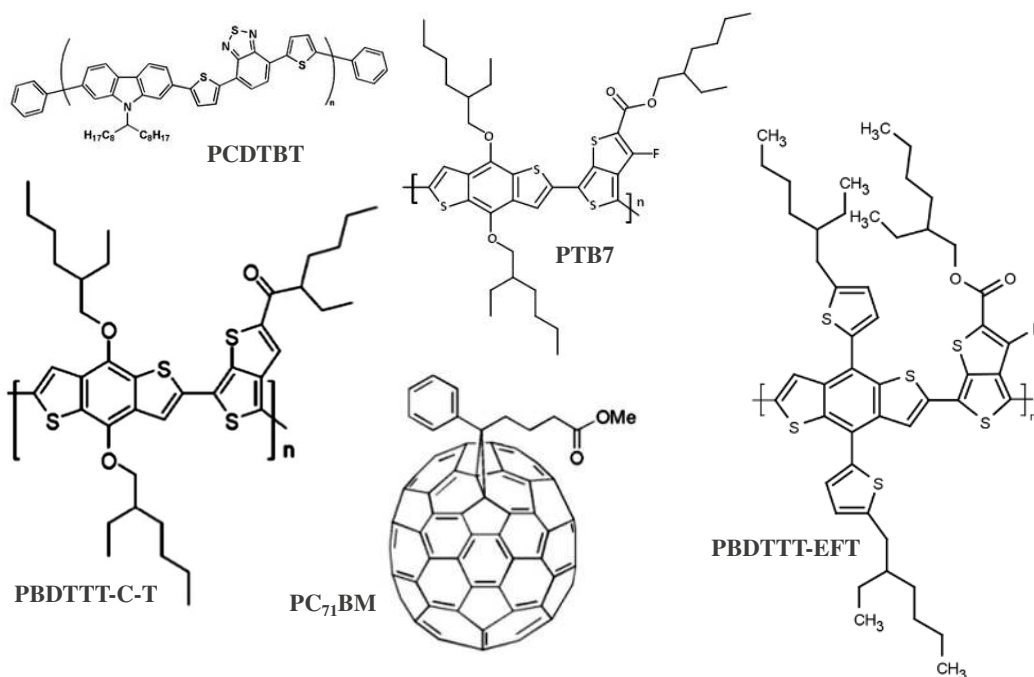
Figure 2.3. A few low-band gap polymers and a high-absorbing fullerene derivative.

Over the years, a series of low band gap polymers have been developed. Benzo[1,2-b:4,5-b']dithiophene (BDT) based conjugated polymer PBDTTT-C-T (poly(4,8-bis(5-(2-ethylhexyl)-thiophene-2-yl)-benzo[1,2-b:4,5-b′]dithiophene-alt-alkylcarbonyl-thieno[3,4-b]thiophene)), when blended with $PC_{71}BM$, exhibited 7.5% PCE with regular architecture, and more than 9% PCE with inverted architecture [50,51]. Another low-bandgap semiconducting polymer, poly[[4,8-bis[(2-ethylhexyl)oxy]benzo[1,2-b:4,5-b′]dithiophene-2,6-diyl][3-fluoro-2-   [(2-ethylhexyl)car-bonyl]thieno[3,4-b]thiophenediyl]] (PTB7) was shown to exhibit similar performance when blended with $PC_{71}BM$ [46,52,53]. The most recent low band gap conjugated polymer is poly[4,8-bis(5-(2-ethylhexyl)thiophen-2-yl)-benzo[1,2- b ;4,5- b ′]dithiophene-2,6-

diyl-alt-(4-(2-ethyl-hexyl)-3-fluorothieno[3,4-b]thiophene-)-2-carboxylate-2-6-diyl)] (PBDTTT-EFT), which, also known as PTB7-Th, is a derivative of PTB7. Recently, Liao et al. reported more than 10% PCE with a single-junction inverted organic solar cell based on this polymer [54]. The latest encouraging results on OPVs have been reported by He et al. [55] based on the same polymer. The authors achieved 10% certified PCE. It is worth noting here that most of the BHJs based on the abovementioned low bandgap polymers incorporate a small amount of processing additive such as 1,8-diiodoctane [46,52], 1,8-octanedithiol [56], 1,8-dibromooctane [57], etc. in the casting solution. Use of additive helps tuning the nanoscale morphology of active layer film, and significantly improves device efficiency [51-55].
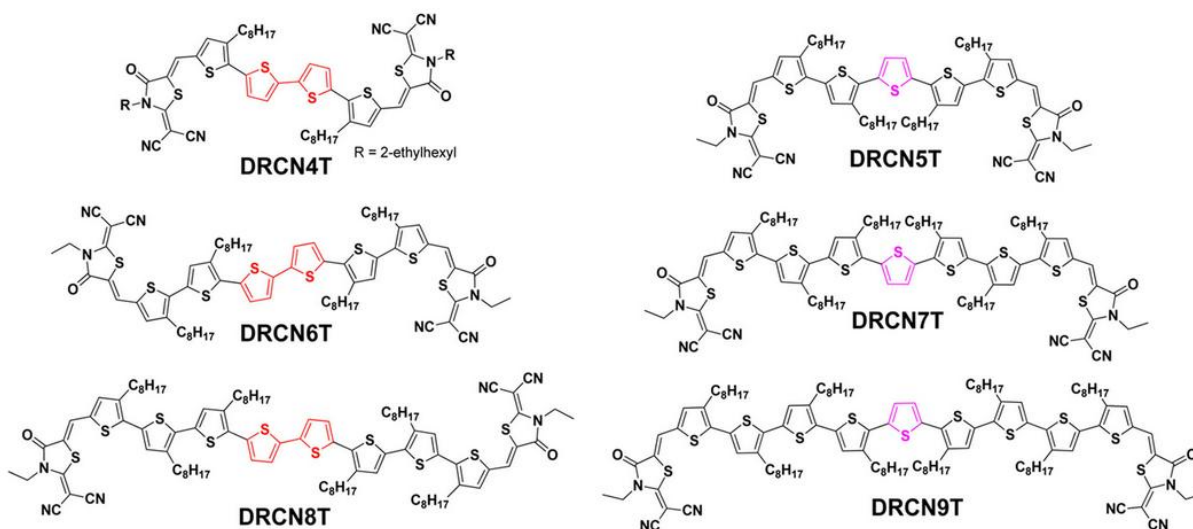
Figure 2.4. Chemical structures of a series of oligomer-like small molecules based on oligothiophenes [60].

In addition to conjugated polymer based OSCs, several research groups also reported high-efficiency small molecule-based OSCs. For instance, Sun et al. reported that solution-processed small-molecule donor, 5,5'-bis{(4-(7-hexylthiophen-2-yl)thiophen-2-yl)-[1,2,5]thiadiazolo[3,4-

c]pyridine}-3,3'-di-2-ethylhexylsilylene-2,2'-bithiophene (DTS(PTTh$_2$)$_2$) exhibits PCE as high as 6.7% [58]. Another small molecule donor, 7,7′-(4,4-bis(2-ethylhexyl)-4H-silolo[3,2-b:4,5-b′]dithiophene-2,6-diyl)bis(6-fluoro-4-(5′-hexyl-[2,2′-bithiophen]-5-yl)benzo-[c]-[1,2,5] thiadiazole) (p-DTS(FBTTh$_2$)$_2$) was reported to exhibit ~ 9% PCE with the use of a thin ZnO film as optical spacer [59]. Most recently, Kan et al. designed and synthesized a series of oligomer-like small molecules (**Figure 2.4**), achieving a record certified PCE of 10.08% [60].

2.2 Perovskite Solar Cells

Compared to OSCs, perovskite solar cells (PSCs) are a very new photovoltaic technology. This section covers a review of the current status of this technology. Before going into details, it is necessary to define the perovskite materials or perovskites. Calcium titanate (CaTiO$_3$), a calcium titanium oxide material, is called perovskite, and it was named after Russian mineralogist, Lev Perovski. Perovskites are usually considered to be a family of chemical compounds that have a general nomenclature of **ABX$_3$**, similar to that of CaTiO$_3$. In case of organometallic tri-halide perovskite materials that are used in solar cell applications, **A** stands for a larger organic cation, mostly methylammonium (CH$_3$NH$_3^+$) or formamidinium (NH$_2$CH=NH$_2^+$), **B** for smaller metal cation (mostly Pb^{2+} or Sn^{2+}), and **X** for monovalent halide anion (Cl$^-$, Br$^-$, or I$^-$) that binds the other two (**Figure 2.5**a). Perovskites can have cubic/orthorhombic/tetragonal phase depending on temperature and combination of ions in the compound [17,61]. Two members of the organometallic tri-halide perovskite family – pure halide perovskite (CH$_3$NH$_3$PbI$_3$) and mixed halide perovskite (CH$_3$NH$_3$PbI$_{3-x}$Cl$_x$) – are dominating the field of PSCs so far. However, there are a series of other derivatives such as CH$_3$NH$_3$PbBr$_3$, CH$_3$NH$_3$PbI$_{3-x}$Br$_x$, etc. being used as the absorber layer.

16

Both $CH_3NH_3PbI_3$ and $CH_3NH_3PbI_{3-x}Cl_x$ have tetragonal crystal structure as shown in Figure 2.5a. Strong Bragg peaks in X-ray diffraction (XRD) pattern (Figure 2.5b) of perovskite ($CH_3NH_3PbI_{3-x}Cl_x$) films, irrespective of processing technique, at $\sim$ 14.1° and 28.4°, corresponding to (110) and (220) planes, respectively, indicate the formation of a highly crystalline tetragonal perovskite film.
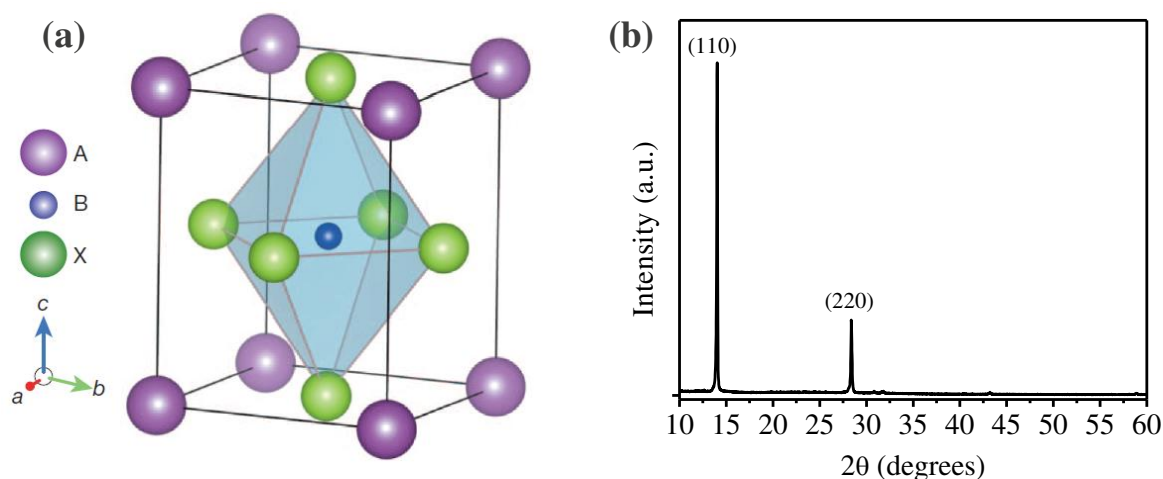
Figure 2.5. a) Single unit cell of an ABX_3 perovskite crystal [61]. b) X-ray diffraction (XRD) pattern of a $CH_3NH_3PbI_{3-x}Cl_x$ film.

Perovskite materials came under extreme focus of photovoltaic research communities after they were first used as light absorbers in solar cells by Kojima et al. in 2009 [17]. Their incorporated device architecture was very similar to the conventional architecture of DSSCs. In a DSSC (**Figure 2.6**a,b), a dye such as 1-ethyl-3 methylimidazolium tetrocyanoborate [$EMIB(CN)_4$] and copper-diselenium [$Cu(In,GA)Se_2$] is used as the light-absorbing layer deposited on top of a porous TiO_2-coated fluorine-doped tin oxide (FTO) electrode. Then, an electrolyte solution is incorporated onto dye, and a back contact, usually made of platinum-

coated FTO glass, is sealed to complete the device. Kojima et al. basically replaced the dye layer by each of these perovskites – $CH_3NH_3PbI_3$ or $CH_3NH_3PbBr_3$, leaving the other layers as same as in DSSCs. They achieved encouraging PCEs of 3.81 and 3.13%, respectively, comparable to PCEs of most of the contemporary OSCs.
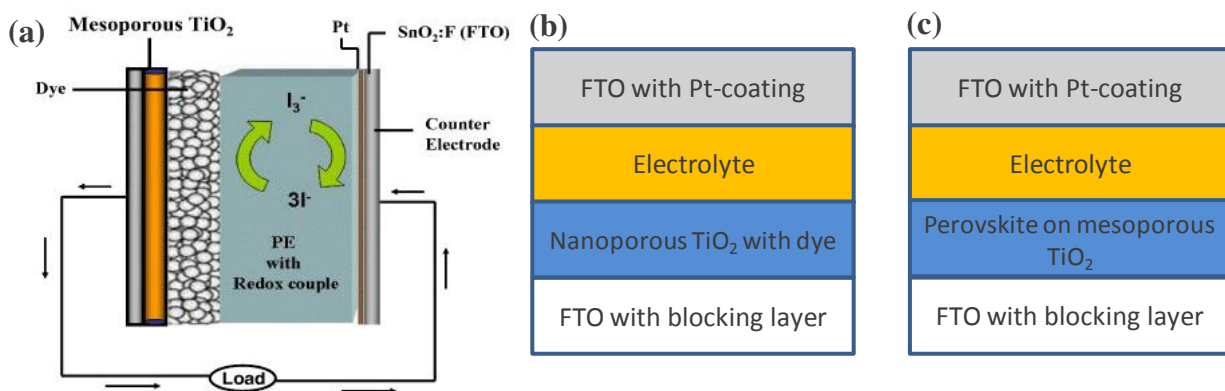
Figure 2.6. a) A typical DSSC [62]. b) Simple schematic representation of device in (a). c) Schematic representation of device architecture used by Kojima et al. [17].

This seminal work on application of perovskite materials in solar cells grew tremendous interests in PV communities all over the world. In 2011, Im et al. reported a 6.5% PCE for perovskite-based quantum dot solar cells [63]. In 2012, several groups reported around 10% efficiencies using a nanostructured (or mesostructured) architecture, where perovskite layer was coated on a mesoporous semiconducting TiO_2 or insulating Al_2O_3 layer, as shown in **Figure 2.7**. This rapid increase in PCEs was possible due to some of the excellent properties of perovskite materials - long carrier diffusion lengths [64], high carrier mobility [65], small exciton binding energy [66], and large absorption coefficients [67], etc.
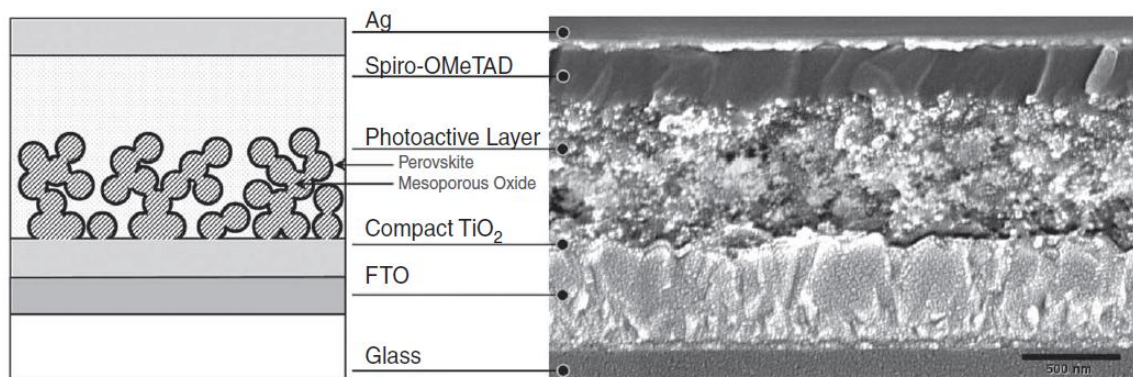
Figure 2.7. Schematic and cross-section SEM of a typical perovskite-sensitized mesoscopic solar cell [67].

In 2013, it was shown by Liu et al. that the nanostructuring using a mesoporous (mp) oxide is not necessary to achieve high-efficiency devices [61]. They achieved a record PCE of 15.4% using a vapor deposition technique, where the organic and inorganic precursors were co-evaporated with a certain stoichiometric ratio. In comparison, their solution-processed cells, with the same stoichiometric ratio, exhibited an average PCE of only ~9%. The higher PCE from vapor deposition was due to the high and extremely uniform perovskite film coverage, and thus reduced leakage paths. The reason of lower and rough film coverage from solution-processed technique is the faster crystallization of perovskites. In order to solve this problem, Burschka et al. came up with a layer-by-layer deposition technique, where they separately coated inorganic and organic precursor solutions [68]. They first spin-coated inorganic lead iodide (PbI_2) solution and annealed the obtained films at 70 °C for 30 min. Subsequently, the PbI_2 films were dipped into the methylammonium iodide (MAI) solution in isopropanol, followed by an annealing at 70 °C for 30 min to drive the interdiffusion between PbI_2 and MAI to form perovskite. By this approach, they were able to achieve very uniform perovskite films, and the resulting devices exhibited a PCE as high as 15%.

It should be noted at this point that all the PSCs discussed above incorporated either a mesostructured architecture, i.e., ITO/TiO$_2$/mp-oxide/perovskite/HTL/back contact or planar heterojunction architecture avoiding the use of mesoporous oxide layer, i.e., ITO/TiO$_2$/perovskite/HTL/back contact. This architecture is also known as *n-i-p* architecture (**Figure 2.8**a) in the sense that light passes through *n*-type layer first. The PCE of PSCs with this architecture gradually reached above 20% [69-71], achieved through compositional and process engineering.

The *n-i-p* architecture is similar to the inverted architecture of OSCs. The mostly used *n*-type or electron transport layer (ETL) is TiO$_2$ [67,68,70] and ZnO [72,73], and *p*-type or hole transport layer (HTL) is 2,2′,7,7′-tetrakis-(N,N-di-pmethoxyphenylamine) 9,9′-spirobifluorene (Spiro-OMeTAD) [67,70,73] However, use of polymeric hole conductor such as P3HT [74], poly-triarylamine (PTAA) [18], poly-[[9-(1-octylnonyl)-9H-carbazole-2,7-diyl]-2,5-thiophenediyl-2,1,3-benzothiadiazole-4,7-diyl-2,5-thiophenediyl] (PCDTBT) [75], etc. also led to high-efficiency devices. To increase the hole conductivity, each of these HTLs is usually doped with lithium-bis(trifluoromethanesulfonyl)imide (Li-TFSI) and 4-tert-butylpyridine (*t*BP) [67,68,70,71].

Perovskite solar cells can also be fabricated in *p-i-n* or inverted architecture [76,77], similar to OSC regular architecture (Figure 2.8b), where mostly PEDOT:PSS is used as HTL, PCBM or ZnO is used as ETL, and Al or Ag is used as back contact [78,79]. Inverted PSCs exhibit comparable device performance to that of conventional PSCs [78-80].
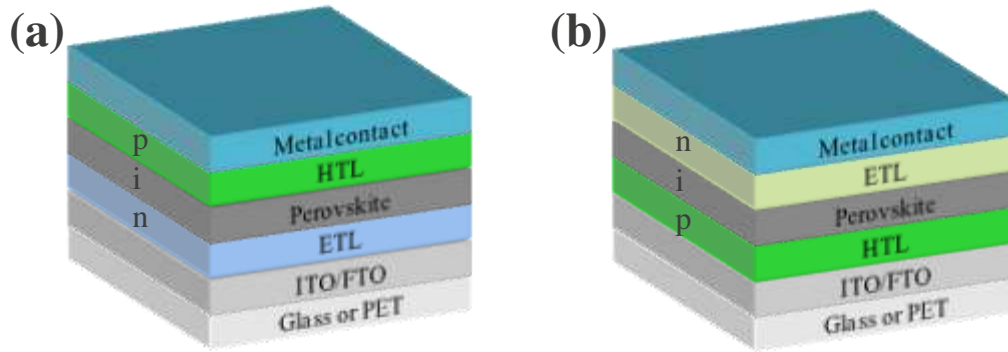
Figure 2.8. Planar perovskite solar cells with a) *p-i-n* and b) *n-i-p* architectures.

Although PSCs show very promising performance, there are some issues that need to be addressed before their commercialization. One of the major concerns with these solar cells is the presence of hysteresis in *J-V* characteristics. The cell shows different efficiencies depending on scanning direction, which makes it difficult to accurately quantify the performance. While there have already been several studies on the origin of hysteresis [18,81,82], the root cause is so far unclear. However, in devices based on *p-i-n* structures, the hysteresis effect is less pronounced [79,83]. The second big concern about PSCs is their poor air stability due to their high moisture sensitivity, which expedites the decomposition [70,84]. Finally, the presence of environmentally hazardous lead (Pb) in PSCs is another major concern. In order to develop environmentally clean and friendly perovskite solar cells, it is necessary to replace Pb by tin (Sn) or germanium (Ge), which are also the members of group-14 metals in periodic table. Several research groups have already reported tin (Sn) based perovskite ($CH_3NH_3SnI_3$ and $CH_3NH_3SnI_{3-x}Br_x$) solar cells [85,86] with encouraging efficiency of ~6%. However, Sn-based perovskites are well-known for their poor atmospheric stability. Improved processing technique and engineering to increase the PCE and more advanced sealing technique to enhance the atmospheric stability of these solar cells could expedite the commercialization of this new technology in future.

Chapter 3: Interface and Morphology Engineering in Polymer-Based Organic Solar Cells

3.1 Research Goal

In this chapter, a very important question regarding a state-of-the-art bulk-heterojunction (BHJ) OSC system is addressed – why inverted OSCs (i-OSC) exhibit superior performance compared to conventional OSCs (c-OSCs)? The BHJ consists of a low bandgap conjugated polymer, poly[[4,8-bis[(2-ethylhexyl)oxy]benzo[1,2-b:4,5-b′]dithiophene-2,6-diyl][3-fluoro-2-[(2-ethylhexyl)car-bonyl]thieno[3,4-b]thiophenediyl]] (PTB7) as the electron donor and [6,6]-phenyl C_{71}-butyric acid methyl ester (PC$_{71}$BM) as the electron acceptor (**Figure 3.1**).

As of today, most of the c-OSCs incorporate PEDOT:PSS as the hole transport layer and low work-function metals as such as Al as top electrodes. Both of these materials are highly reactive with air and hence, quickly degrade the device performance [87,88]. This has been one of the major concerns for the current OSC research, necessitating the fabrication of inverted organic solar cells (i-OSCs). It is well-known that i-OSCs demonstrate excellent stability in ambient conditions, which is realized by avoiding the use of PEDOT:PSS and low work-function electrodes [89,90]. Despite the outstanding long-term device stability, however, early i-OSCs suffered from lower PCE as compared with c-OSCs [91]. Moreover, most early i-OSCs used an *n*-type metal oxide such as TiO$_2$ as hole blocking layer that involves high temperature sintering (> 300 °C) in the device fabrication process [44,92], thus making them incompatible with flexible substrates preferred for roll-to-roll manufacturing. A breakthrough research overcoming such low PCE and incompatibility has recently been made by He *et al*. [53]. They fabricated PTB7:PC$_{71}$BM i-OSCs, where conjugated poly[(9,9-bis(3′-(N,N-dimethylamino)propyl)-2,7-

fluorene)-alt-2,7-(9,9–dioctylfluorene)] (PFN, Figure 3.1) layer was used as an ITO-cathode surface modifying layer that reduces the energy gap between $PC_{71}BM$ and ITO, facilitating easier electron transport to the cathode. From these i-OSCs, the authors achieved a record PCE of 9.2% and excellent ambient device stability. The PCEs of PFN-incorporated i-OSCs were reported to be higher than those of their counterparts with regular device architecture (PCE = ~8%) fabricated using the same casting solution. Room-temperature, solution-processed PFN is favorable for flexible and large-scale roll-to-roll production [93].
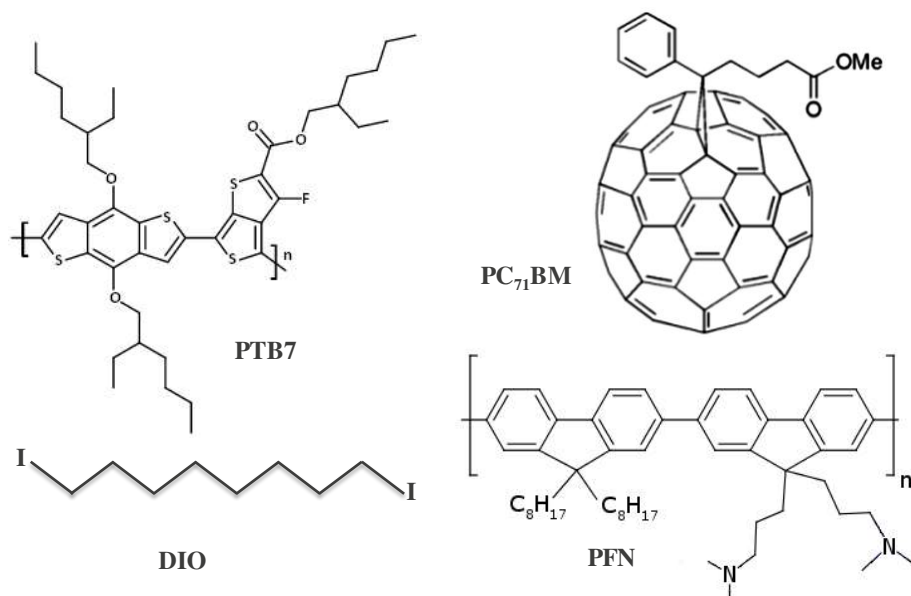
Figure 3.1. Chemical structures of PTB7, $PC_{71}BM$, DIO, and PFN.

While the origin for the long-term ambient stability of i-OSCs has been well understood, the underlying morphological mechanism for their high PCE has so far remained to be investigated. The focus of this part of the research [94] is on understanding how the incorporated PFN layer interacts with PTB7 and $PC_{71}BM$ at the interface, affects the active layer morphologies, and

enhances the PCEs of the i-OSCs. The lateral and vertical phase morphologies of PTB7:PC$_{71}$BM/PFN were studied by a combination of neutron reflectometry (NR) and cross-section TEM. Grazing incidence wide-angle X-ray scattering (GIWAXS) was used to study the relative crystallinity and crystal orientation. In addition, small-angle neutron scattering (SANS) was used to study the precursor structures of PTB7 and PC$_{71}$BM in the casting solution, as well as the effect of the solvent additive 1,8-diiodooctane (DIO, Figure 3.1) additive on the structures of precursors. The obtained structural information was linked to the measured device performances, providing important guidance to the design of more efficient i-OSCs.

3.2 Experimental Section

3.2.1 Device Fabrication

PTB7 and PFN were purchased from 1-Material, and PC$_{71}$BM was purchased from Lumtec, and used as received. DIO was purchased from Sigma Aldrich. The casting solution was prepared by dissolving PTB7 and PC$_{71}$BM (with 1:1.5 weight ratio and 25 mg/ml total concentration) in dichlorobenzene (DCB) with or without 3% DIO additive, and heating at 70 °C for couple of hours under stirring. ITO substrates were first cleaned by using detergent and subsequently by sonication in deionized (DI) water, acetone, and isopropyl alcohol (IPA), followed by baking at 80 °C for one hour.

For i-OSC fabrication, the PFN solution was prepared by dissolving PFN in methanol (2 mg/ml) in the presence of a small amount of acetic acid (2 µl/ml), and the solution was spun-cast onto UV-treated ITO substrates at 2000 rpm for 60 s in air. The PTB7:PC$_{71}$BM active layers were then spun-cast on top of PFN-coated ITO at 1000 rpm for 90 s, followed by drying for 30

minutes in inert ambient. Finally, devices were completed by thermally depositing 8 nm-thick MoO_3 and 100 nm-thick Ag layers under a vacuum level of 5×10^{-6} mbar.

For c-OSCs, PEDOT:PSS solution was spun-cast onto UV-treated ITO substrates, followed by baking at 135 °C in air for 30 minutes. The active layer was spun-cast using same recipe as in i-OSCs, and devices were completed by thermally depositing 15 nm-thick Ca and 85 nm-thick Al layers. The device area of 23.7 mm^2 was calculated by a high-resolution optical microscope.

3.2.2 Device, Solution, and Thin Film Characterization

The current density-voltage (*J-V*) curves of the fabricated solar cells were recorded using a source meter (Keithley 2400, USA) and a solar simulator (Radiant Source Technology, 300 W, Class A) under the AM 1.5G (100 mW cm^{-2}) conditions. The intensity of the solar simulator was calibrated by a NIST-certified Newport Si reference cell.

The external quantum efficiency (EQE) spectra were measured in air using a Newport QE measurement kit under short circuit conditions. Both UV-Vis absorption spectroscopy and reflective absorption spectra were recorded using a Varian Cary UV-Vis-NIR spectrophotometer. Reflective absorption was measured in diffuse mode with an integration sphere. In this case, the incident light through the ITO electrode was reflected from the metal electrode back into the active layer for secondary absorption. Atomic force microscope (AFM) images were acquired with a Bruker Dimension Icon operating in a tapping mode.

Films for NR, cross-section TEM, and GIWAXS were prepared on PFN-coated or bare Si-substrates. SANS measurements for the solutions were conducted at the EQ-SANS beamline in the Spallation Neutron Source (SNS), Oak Ridge National Laboratory (ORNL). 10 mg/ml PTB7/DCB and PTB7/DCB:DIO, and 15 mg/ml $PC_{71}BM$/DCB and $PC_{71}BM$/DCB:DIO

solutions were loaded into 1mm-thick quartz cells, and the scattered beams were collected at each SANS configuration. The raw two-dimensional (2D) SANS data were corrected for detector response, dark current, and scattering from background, before being azimuthally averaged to produce the 1D SANS profiles, i.e., scattered intensity, $I(q)$ versus scattering vector, q profile, where $q = 4\pi\sin\theta/\lambda$ with λ and θ being the wavelength of the incident neutron beam and the half of scattering angle, respectively. The data were placed on an absolute scale (cm^{-1}) by the use of measured direct beam. The scattered neutrons were collected using a 2D position sensitive He detector with 1×1 m^2 active area, composed of tube detectors providing 256×192 pixels.

NR data were collected on the Liquids Reflectometer at the SNS, ORNL using a neutron beam with a bandwidth of 3.5 Å (2.5 Å$<\lambda<$6.0 Å), where λ is the wavelength of incident neutron. The reduced data were in the format of absolute neutron reflectometry (R) vs. Out-of-plane neutron momentum transfer (q_z), where $q_z = (4\pi/\lambda) \sin\alpha_i$ with α_i being the incidence angle of neutron beam. In order to account for the instrumental smearing of NR data, the instrumental resolution provided at the beamline was convolved with the calculated NR curves. GIWAXS patterns were measured on the beamline 8ID-E at Advanced Photon Source (APS), Argonne National Laboratory (ANL). In the GIWAXS measurements, the used wavelength of the X-ray beam was 1.6868 Å, and the grazing incidence angle was 0.2°.

Samples for cross-section TEM measurements were prepared by a focused ion beam (FIB) milling in a Zeiss Auriga dual beam SEM FIB. TEM imaging was performed at the University of Tennessee using a Zeiss Libra 200 MC operated at 200 kV. For EF-TEM imaging, an energy slit width of 8 eV was used, centered at 19 and 30 eV, to generate contrast between the PTB7 and $PC_{71}BM$. The contrast in the images was adjusted to maximize the intensity variations within the

PTB7:PC$_{71}$BM layer. The two complementary images were artificially colored blue and yellow, and superimposed to clearly show the morphological structure within the bulk-heterojunction.

3.3 Results and Discussion

Figure 3.2a shows the current density versus voltage (*J-V*) curvess for a typical solar cell of each of the following architecture-processing combinations: ITO/PFN (10 nm)/active layer/MoO$_3$(8 nm)/Ag i-OSCs with and without 3 wt.% DIO additive in the PTB7:PC$_{71}$BM-in-DCB solution for spin-casting the active layer; and ITO/PEDOT:PSS (40 nm)/active layer/Ca (15 nm)/Al c-OSCs with and without 3 wt.% DIO additive when spin-casting the PTB7:PC$_{71}$BM active layer. The device parameters (averaged over 20 devices in each type), i.e., short-circuit current density (J_{SC}), open circuit voltage (V_{OC}), fill factor (FF), and PCE are tabulated in **Table 3.1**.
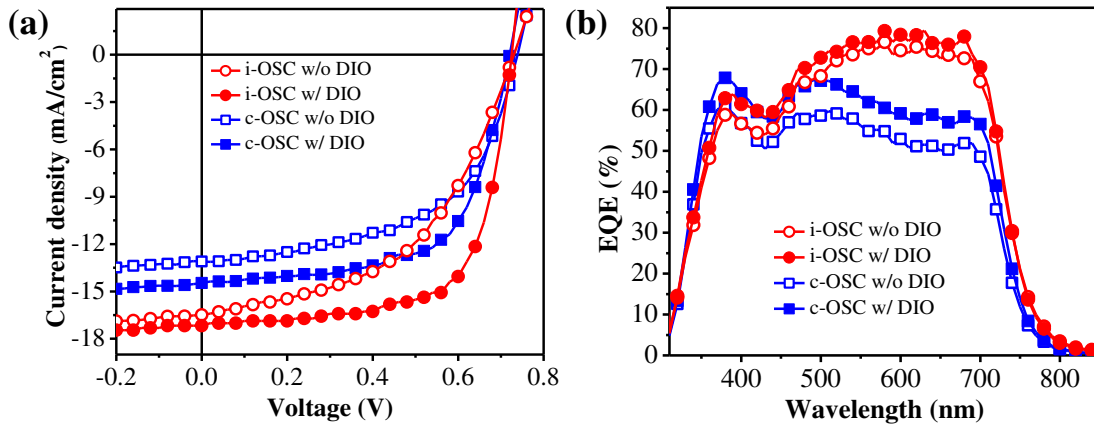
Figure 3.2. a) *J-V* curves for four different devices. b) External quantum efficiency (EQE) spectra for the corresponding devices.

As can be seen from Table 3.1, i-OSCs with and without DIO, exhibit higher PCEs than their c-OSC counterparts and that the DIO additive increases PCEs for both i-OSCs and c-OSCs. The

superior performance for the i-OSCs is attributed to efficient charge extraction by the ITO cathode the effective work function of which is drastically modified by PFN [53,55]. Here, PTB7:PC$_{71}$BM i-OSCs fabricated with 3 wt% DIO exhibit PCE as high as 9.3%, much higher than the c-OSCs fabricated using the same solution showing a maximum PCE of 7.2% (**Figure 3.3**a). Also, the i-OSCs retain ~94% of their initial PCEs up to more than 26 days when stored in air while OSCs lose 30% of their initial PCE in just 5 days (Figure 3.3b). The higher PCEs of i-OSCs, compared to those of c-OSCs, are due to their higher J_{SC} values, confirming that this is the result of efficient electron extraction. The EQE spectra for the same devices in Figure 3.2a, measured under short circuit conditions in air without encapsulations, are shown in Figure 3.2b. The integrated J_{SC} values for i-OSCs, with and without DIO, are 16.6 and 15.9 mA/cm^2, respectively, while those for c-OSCs are 14.1 and 12.4 mA/cm^2, reasonably well-consistent with the J_{SC} values, measured from J-V curves in the inert ambient.

Table 3.1. Summary of device parameters, i.e., J_{SC}, V_{OC}, FF, and PCE of the OPV devices fabricated with different device architectures.

Device Type	J_{SC} [mA/cm^2]	V_{OC} [V]	FF [%]	PCE$_{avg}$ [%]	PCE$_{max}$ [%]
i-OSC w/o DIO	15.3	0.72	47.8	5.3 ± 0.3	5.8
i-OSC w/ DIO	16.9	0.72	67.0	8.2 ± 0.5	9.3
c-OSC w/o DIO	12.9	0.74	52.7	5.0 ± 0.3	5.5
c-OSC w/ DIO	14.4	0.72	62.3	6.5 ± 0.3	7.2

To estimate the internal quantum efficiency (IQE) spectra, the reflective absorption spectrum for each architecture-processing combination (**Figure 3.4**a) was first measured mimicking the light absorption process in an actual device. Here it should be noted that IQE is defined as the

percentage of absorbed photons that are converted into charges and collected at the electrodes at zero bias. The IQE spectra (Figure 3.4b) were estimated by following the procedures reported elsewhere [95]. Irrespective of the presence of DIO, i-OSCs show higher IQE compared to c-OSCs. The DIO additive increases the IQEs for both the i-OSCs and c-OSCs, and more importantly, the i-OSC using DIO shows an IQE approaching 95% in the 500 to 700 nm spectral range. In principle, the high IQE is originated from highly efficient exciton generation and dissociation, and charge collection.
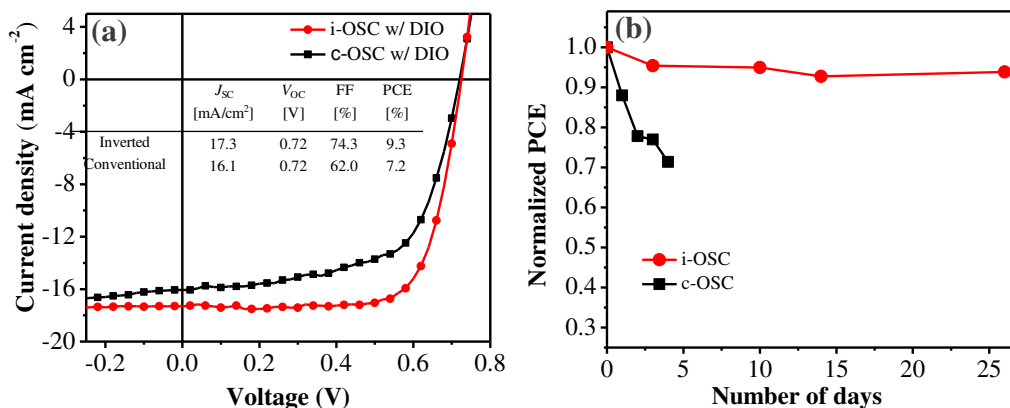
Figure 3.3. a) *J-V* curves for the champion i-OSC and c-OSC, measured under AM 1.5G (100 mW/cm^2) illumination. b) Stability comparison of c-OSCs and i-OSCs stored in air without encapsulation- the normalized PCE as a function of time.

To understand the origin of the near-unity IQE, a variety of characterization techniques were employed to systematically examine the PTB7:PC$_{71}$BM active film morphology in the i-OSCs as well as processing factors that influence the morphology. It has been shown that the initial precursor structures of electron donor (ED) and acceptor (EA) materials in the casting solution affect the crystallinity and phase morphology of the spun-cast films [96]. Here, small-angle neutron scattering (SANS) measurements were conducted on the PTB7 and PC$_{71}$BM solutions in

DCB with and without DIO, to investigate the structure of PTB7 (ED) and PC$_{71}$BM (EA) in the solutions, and the effect of DIO. As seen from the SANS curves in **Figure 3.5**a, both PC$_{71}$BM solutions in DCB and DCB:DIO merely exhibit flat scattering features, implying complete dissolution. If PC$_{71}$BM forms aggregates or clusters in the solutions, scattering features, showing an asymptotic decay in scattered intensity as a function of the scattering vector q, must be observed. The results are consistent with previously reported work, showing complete dissolution of PC$_{71}$BM in DCB and DCB:DIO [97].
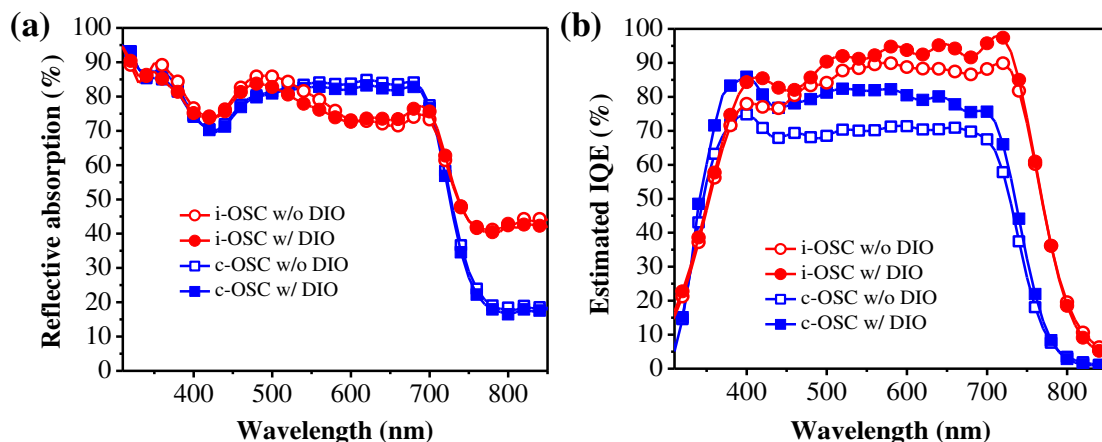
Figure 3.4. a) Spectral reflection spectra, calculated using four different device architectures. b) Estimated internal quantum efficiency (IQE) spectra of devices shown in Figure 3.2a.

There have also been possibly contradicting results reported by Lou *et al* based on the small-angle X-ray scattering (SAXS) [98], indicating that the added DIO selectively increases the solubility of PC$_{71}$BM when mixed with the host solvent, chlorobenzene (CB). In the study, it was proposed that the added DIO selectively increases the solubility of PC$_{71}$BM when mixed with CB, resulting in reduced domain size of PC$_{71}$BM in the spun-cast active layer. In this current and our other previous studies, however, used solvents, DCB and DCB:DIO are found to dissolve

PC$_{71}$BM at the molecular level. The different conclusions might come from the solubility difference between CB and DCB. On the other hand, the SANS patterns of PTB7 solutions in DCB and DCB:DIO appear totally different from those of PC$_{71}$BM solutions. The SANS curves for PTB7 solutions were modeled using a worm-like chain model with excluded volume effect under the assumption that PTB7 assumes a semi-rigid chain nature in good solvents. Since the SANS curves for both PTB7 solutions in DCB and DCB:DIO are almost identical within the error range, a single set of model parameters was applied to fit both curves. The fit parameters, including contour length (*L*), Kuhn length (*b$_i$*), and diameter (*R*), are tabulated in **Table 3.2**. The *L* is about ~395 Å, a molecular dimension much larger than that of PC$_{71}$BM. The molecular diameter of PC$_{71}$BM is known to be ~11 Å [98].
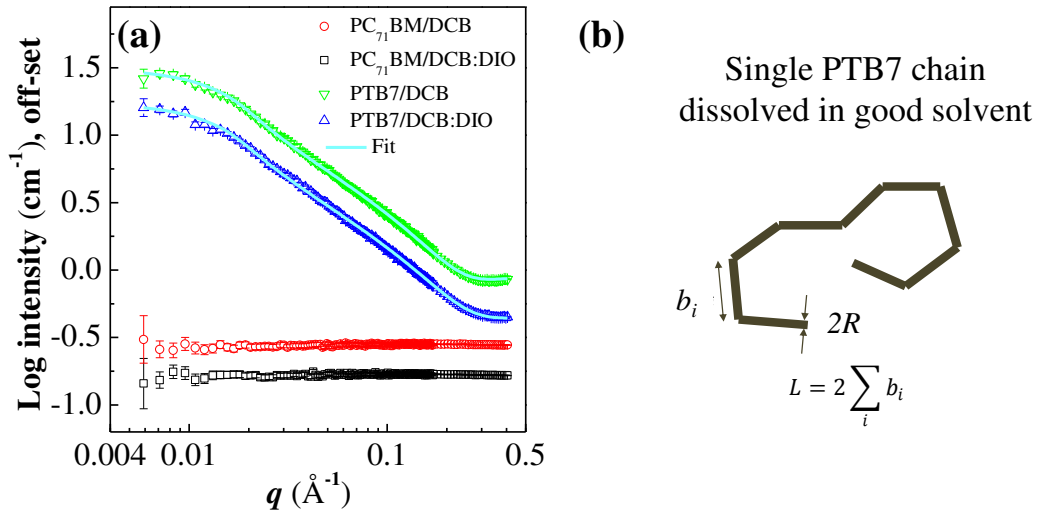
Figure 3.5. a) SANS patterns for PTB7/DCB, PTB7/DCB:DIO, PC$_{71}$BM/DCB, and PC$_{71}$BM/DCB:DIO solutions, where the solid lines indicate model fits by flexible cylinder scattering model with excluded volume effect. b) Schematic illustration of single PTB7 chain dissolved in DCB or DCB-DIO.

Table 3.2. Parameters obtained from the model fits for PTB7 chains dissolved in DCB and DCB:DIO.

	ContourLength, L [Å]	Kuhn Length, b_i [Å]	Radius, R [Å]	Polydispersity
PTB7 in DCB/DCB:DIO	395±5	183±3	10.7±0.3	0.089±0.035

It is apparent that the different scattering features of PTB7 and $PC_{71}BM$ solutions are due to their different molecular sizes and shapes. A schematic diagram showing the possible molecular conformation of PTB7 dissolved in the solvents is shown in Figure 3.5b. The identical SANS curves for both PTB7 solutions indicate that the PTB7 chains have identical swollen or dissolved state regardless of the presence of DIO. Therefore, the SANS results clearly demonstrate that the improved PCEs in both i-OSCs and c-OSCs do not originate from their initial precursor structures in solution.
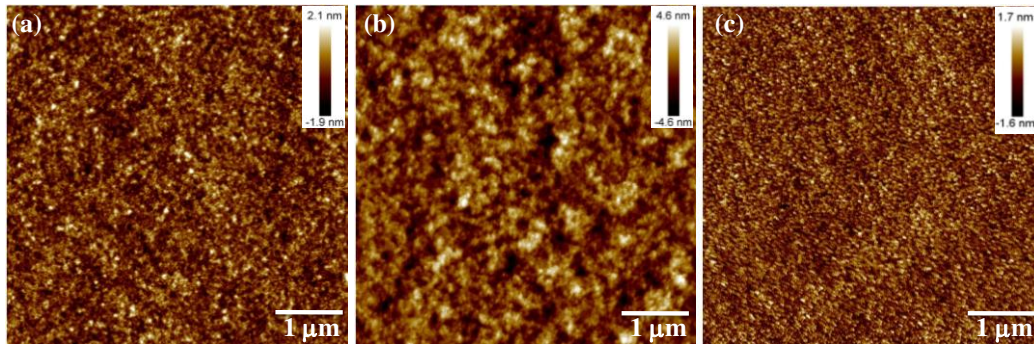
Figure 3.6. AFM images showing film morphology of PTB7:$PC_{71}BM$ active layer on quartz a) without and b) with DIO, and c) PFN film coated on quartz.

Although DIO does not affect the PTB7 and $PC_{71}BM$ structures in solution, it strongly affects the phase separation in spun-cast films as shown in **Figure 3.6**. A pronounced nanophase separation is observed throughout the film with DIO, which is the reason why films with DIO

lead to better device performance irrespective of device architecture. However, no significant difference in absorption was observed from films with and without DIO (**Figure 3.7**).
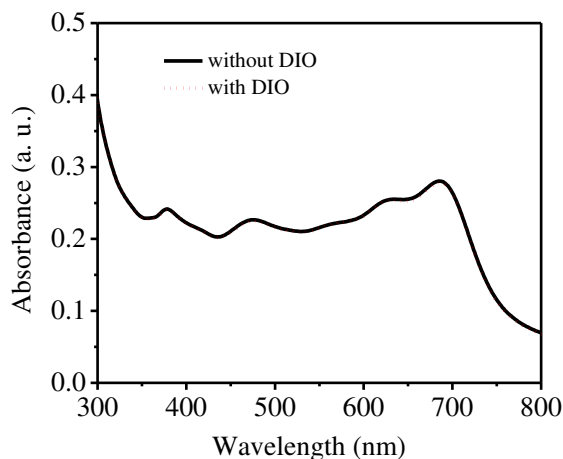
Figure 3.7. UV-Vis absorption spectra for PTB7:PC$_{71}$BM films on quartz substrates with and with DIO additive.

In order to investigate the effect of DIO additive on the phase morphology, PTB7:PC$_{71}$BM films spun-cast from solutions with and without DIO were sectioned using a focusd ion beam (FIB), and the exposed cross-sections were imaged by energy-filtered TEM (EF-TEM). **Figure 3.8** shows the cross-section images for PFN/PTB7:PC$_{71}$BM and PEDOT:PSS/PTB7:PC$_{71}$BM with and without DIO, where the yellow and grey areas indicate PC$_{71}$BM-rich and PTB7-rich regions, respectively. The films exhibit much reduced domain sizes when DIO is used as a processing additive, consistent with the results reported in the literature [52,99]. Nevertheless, in terms of the domain size of PC$_{71}$BM, no clear difference between PFN/PTB7:PC$_{71}$BM and PEDOT:PSS/PTB7:PC$_{71}$BM films, with or without DIO was identified, implying no significant effect of substrate on the sizes of PTB7 and PC$_{71}$BM domains.
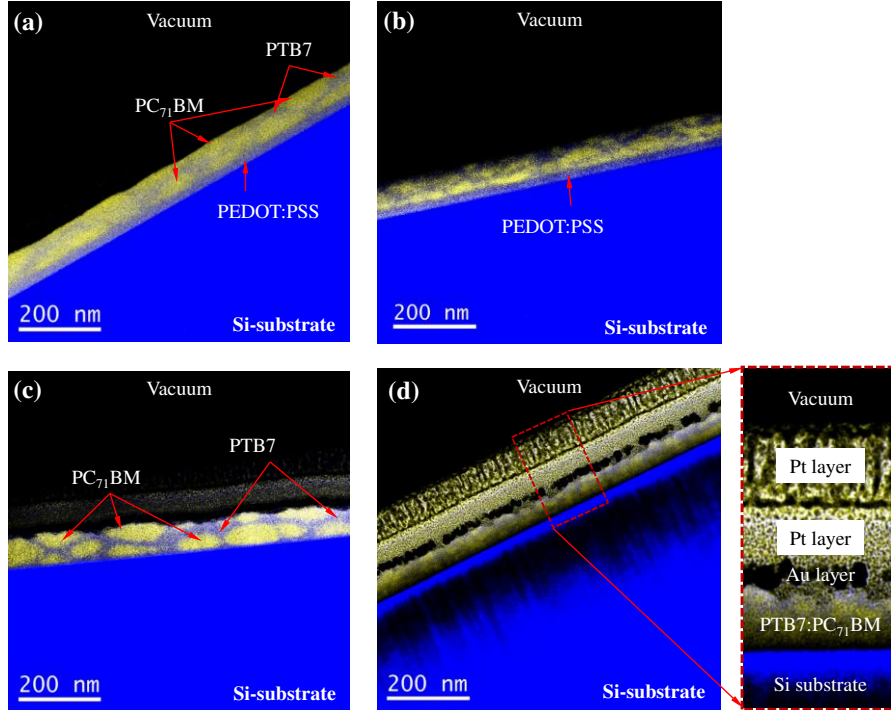
Figure 3.8. Cross-section TEM images for PEDOT:PSS/PTB7:PC$_{71}$BM films (a) without and (b) with 3 wt.% DIO; and PFN/PTB7:PC$_{71}$BM films (c) without and (d) with 3 wt.% DIO.

It is obvious that since the interfacial area between PTB7 and PC$_{71}$BM increases with decreasing domain size, more efficient charge generation is possible as DIO is added to the casting solution resulting in smaller domains. It should be noted that no clear indication of the PFN layer is observed in the TEM images of PFN/PTB7:PC$_{71}$BM regardless of the presence of DIO, while flat interfacial boundaries are clearly identified between PTB7:PC$_{71}$BM and PEDOT:PSS layers in PEDOT:PSS/PTB7:PC$_{71}$BM films both with and without DIO. It is well known that no diffusion of PC$_{71}$BM into PEDOT:PSS layer occurs in spin-casting or thermal annealing [100],which is indeed not preferable, since it would prevent the hole transport to the anode, giving rise to a reduction in PCE. The absence of the PFN layer in the EF-TEM images of the PFN/PTB7:PC$_{71}$BM cross-sections is due to the intermixing between PC$_{71}$BM and PFN, as will be shown in the following section.

34

To investigate the vertical phase morphologies, NR measurements were conducted on PTB7:PC$_{71}$BM films deposited onto PFN-coated Si-substrates. **Figure 3.9**a shows the experimental and fitted NR curves for PFN/PTB7:PC$_{71}$BM films, which were prepared by spin-casting PTB7:PC$_{71}$BM solutions with and without DIO onto PFN-coated Si-substrates. As a reference, experimental and fit NR curves for ~8 nm thick pristine PFN film are also included in Figure 3.9a. Model-fits to the experimental NR curves were performed using Parratt formalism [101], from which the obtained neutron scattering length density (SLD) distributions and the composition distributions or volume fractions of PC$_{71}$BM (V_{PC71BM}), calculated from the SLD distributions, are depicted in Figure 3.9b and c, respectively. V_{PC71BM} of each layer was calculated as follows using equation 3.1 and 3.2 shown below.

$$V_{PC71BM} = (\rho_i - \rho_{PTB7})/(\rho_{PC71BM} - \rho_{PTB7}) \tag{3.1}$$

where, $V_{PC71BM,i}$ is equal to 1-$V_{PTB7,i}$ (volume fraction of PTB7 in i^{th} layer) and varies from 0 to 1 depending on the composition of components. ρ_i is the SLD of ith layer in film, and ρ_{PTB7} and ρ_{PC71BM} are the SLDs of pristine PTB7 and PC$_{71}$BM, respectively. The SLDs of PTB7 and PCBM are obtained by fitting the NR curves for the pristine PTB7 and PC$_{71}$BM films, which are 1.26 ×10^{-6} Å^{-2} and 4.34×10^{-6} Å^{-2}, respectively. Similarly, V_{PC71BM} in PFN layer is calculated as,

$$V_{PC71BM} = (\rho_i - \rho_{PFN})/(\rho_{PC71BM} - \rho_{PFN}) \tag{3.2}$$

where, ρ_{PFN} is the SLDs of pristine PFN, in which the SLD is obtained by fitting the NR curves for the pristine PFN film.
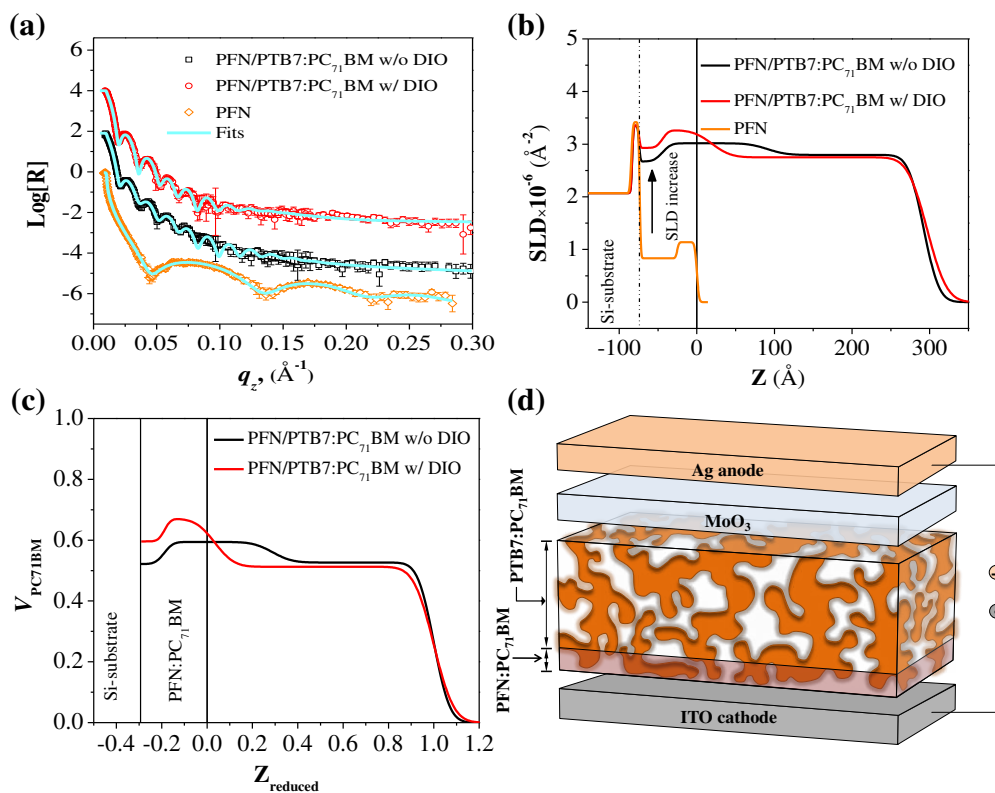
Figure 3.9. a) Experimental and modeled NR curves for PFN/PTB7:PC$_{71}$BM films with and without DIO. b) The SLD profiles used to fit the NR curves shown in (a). c) Volume fraction of PC$_{71}$BM, $Z_{reduced}$ vs. reduced distance from the substrate, calculated from the SLD profiles shown in (b). d) A schematic illustration showing how PC$_{71}$BM diffuses into the PFN layer.

In the case of PFN film, two layers exist, where the layer adjacent to the substrate is enriched by poly(9,9-bis(3'-(N,N-dimethylamino)propyl)-2,7-fluorene) block and the air interfacial layer is enriched by poly(9,9–dioctylfluorene), which are 0.83×10^{-6} Å^{-2} and 1.14×10^{-6} Å^{-2}, respectively (Figure 3.9b). The reason that PFN has two different SLDs could be the phase separation of copolymeric PFN, where the higher SLD could be due to the enrichment of poly [(9,9-bis(3'-(N,N-dimethylamino)propyl)-2,7-fluorene)] with short side chain, and the lower SLD to that of poly[2,7-(9,9–dioctylfluorene)] with its long alkyl side chain.
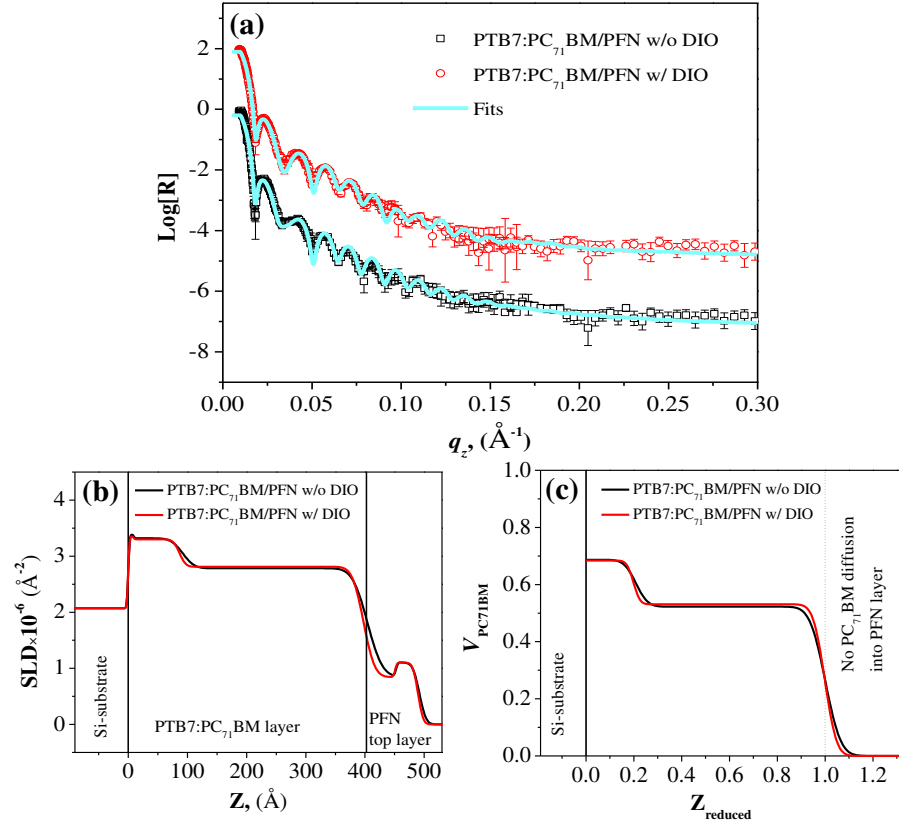
Figure 3.10. a) Experimental and modeled NR curves for PTB7:PC$_{71}$BM/PFN films with and without DIO. b) The SLD profiles used to fit the NR curves shown in (a). c) Volume fraction of PC$_{71}$BM, $Z_{reduced}$ vs. reduced distance from the substrate, calculated from the SLD profiles shown in (b).

The SLDs of PFN increase drastically after spin-casting PTB7:PC$_{71}$BM solutions. In the film spun-cast without DIO, the SLDs of PFN layer increase from $\rho_{PFN} = 0.83 \times 10^{-6}$ and 1.14×10^{-6} Å^{-2} to 2.67×10^{-6} and 3.02×10^{-6} Å^{-2}, respectively. With DIO, the PFN SLDs increase even more to 2.93×10^{-6} and 3.26×10^{-6} Å^{-2}. Since the increased SLDs of PFN after spin-casting are higher than those of PTB7 ($\rho_{PTB7} = 1.26 \times 10^{-6}$ Å^{-2}) and PFN ($\rho_{PFN} = 0.83 \times 10^{-6}$ and 1.14×10^{-6} Å^{-2}), the increases in SLDs should be the results of the diffusion of high-SLD PC$_{71}$BM. The SLD of PC$_{71}$BM is $\rho_{PC71BM} = 4.34 \times 10^{-6}$ Å^{-2}, as shown in **Figure 3.11** and **3.12** . The calculated V_{PC71BM}, with the PFN layer underneath, using Equation 3.2, are 0.52 and 0.59 in PFN/PTB7:PC$_{71}$BM

without using DIO, and are 0.60 and 0.67 with DIO. The diffusion of $PC_{71}BM$ into the PFN layer occurs when the residual solvent molecules remain in the films act as plasticizers and make $PC_{71}BM$ molecules mobile. Based on the TEM images (Figure 3.8) and NR results (Figure 3.9), a schematic illustration of the i-OSC active layer morphology is depicted in Figure 3.9d. Here, the diffusion of $PC_{71}BM$ into PFN layer has a very important implication on the device efficiency, since it can alter the process of electron transport. That is, the diffusion of $PC_{71}BM$ into PFN layer and the phase-separated domain formation of $PC_{71}BM$ can produce much more interfacial contact between $PC_{71}BM$ and PFN. Also, the increased $PC_{71}BM$ diffusion induced by the added DIO facilitates even more interfacial contacts between $PC_{71}BM$ and PFN, resulting in more efficient electron transport to the cathode and electron collection.

To confirm the aforementioned hypothesis, $PTB7:PC_{71}BM$ solutions in DCB with and without DIO were spun-cast onto bare quartz substrates and the films were dried completely, followed by PFN spin-casting. The measured and fitted NR curves for $PTB7:PC_{71}BM$/PFN films spun-cast with and without DIO are depicted in **Figure 3.10**a, from which the acquired SLD and V_{PC71BM} distributions are shown in Figure 3.9b and c, respectively. As can be seen in Figure 3.9b, the SLDs of PFN layers in both $PTB7:PC_{71}BM$/PFN films remain unchanged compared to that of pristine PFN films. Also, the SLDs of $PTB7:PC_{71}BM$ layers in $PTB7:PC_{71}BM$/PFN with and without DIO are identical to those of $PTB7:PC_{71}BM$-only films (Figure 3.11). The results reveal that the diffusion of $PC_{71}BM$ does not occur in $PTB7:PC_{71}BM$/PFN films, since no DCB or DCB:DIO remains in the film. There might be residual methanol after the spin-casting PFN solution; however, it is a nonsolvent for $PC_{71}BM$ and hence, cannot act as a plasticizer.
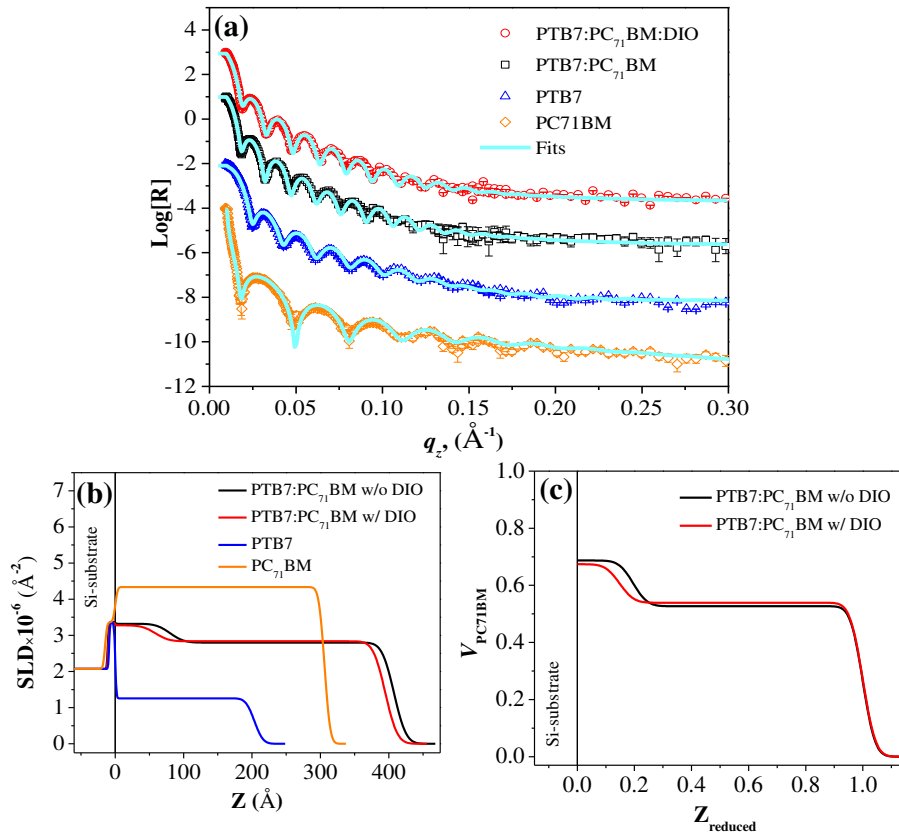
Figure 3.11. a) Experimental and fit neutron reflectivity curves for PTB7:PC$_{71}$BM films with and without DIO, pristine PTB7, and PC$_{71}$BM films spun-cast onto Si-substrates. b) Neutron SLD distributions obtained from the model-fit in (a). c) Volume fraction of PC$_{71}$BM, $Z_{reduced}$ vs. reduced distance from the substrate, calculated from the SLD profiles shown in (b).
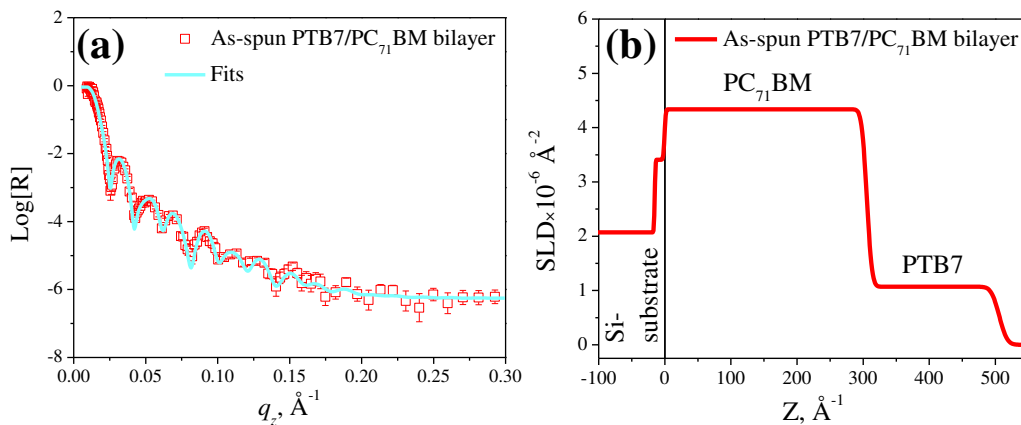
Figure 3.12. (a) Experimental and fit neutron reflectivity curves for PTB7:PC$_{71}$BM bilayer film. (b) SLD distribution obtained from the model-fit in (a).
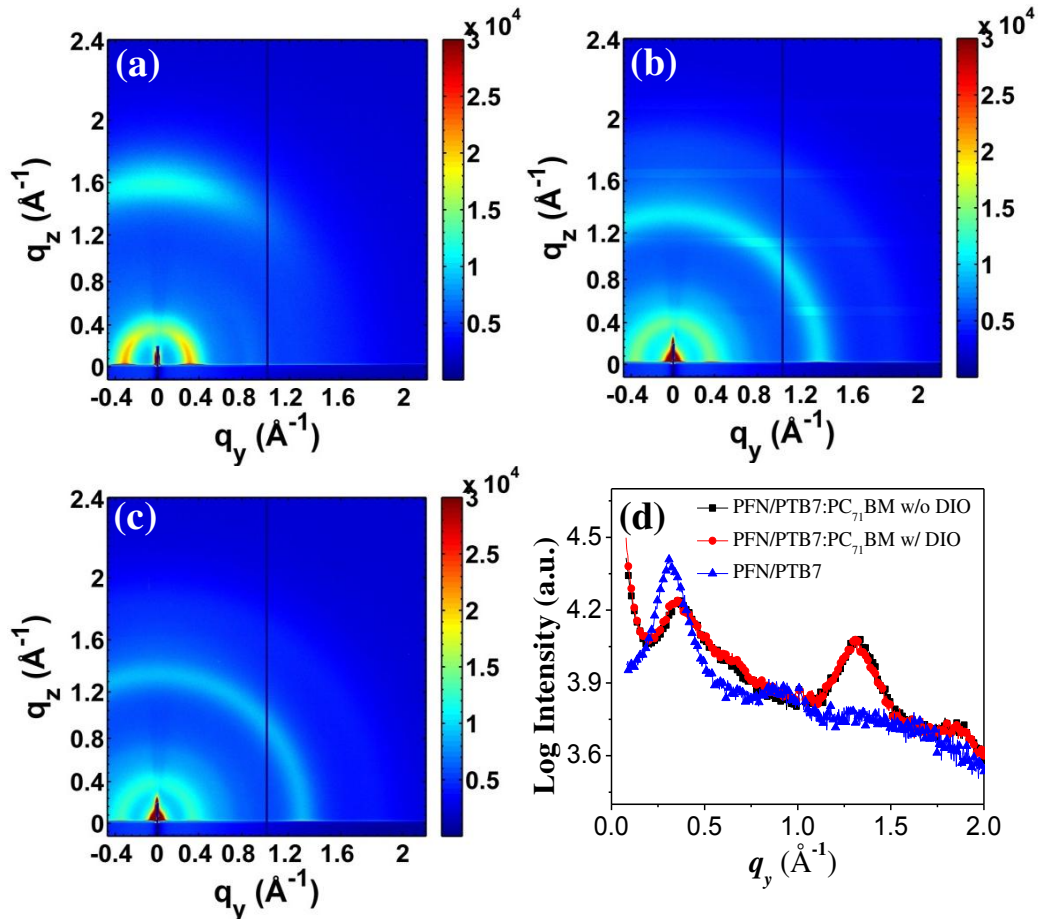
Figure. 3.13. 2D GIWAXS patterns of (a) PFN/PTB7, (b) PFN/PTB7:PC$_{71}$BM without DIO, and (c) PFN/PTB7:PC$_{71}$BM with DIO films. (d) In-plane GIWAXS profiles extracted from the respective 2D GIWAXS patterns.

2D grazing-incidence wide-angle X-ray scattering (GIWAXS) was used to obtain insights into the global orientation, molecular packing and crystallinity of PTB7, and the aggregation of PC$_{71}$BM. A 2D GIWAXS pattern for PFN/PTB7 is first shown in **Figure 3.13**a. Here, q_y is the in-plane scattering vector given by $q_y = 2\pi/\lambda_X[\sin(\psi)\cos(\alpha_f)]$, where λ_X, ψ, and α_f are the wavelength, in-plane exit angle, and out-of-plane exit angle, respectively. In the 2D GIWAXS pattern, the in-plane reflection arcs discerned at $q_y = 0.283 \pm 0.008$ Å^{-1} (*d*-spacing = 22.2 Å) is due to the (100) planes of PTB7 crystal. A broad out-of-plane reflection arc was also observed at

q_z = 1.56 ± 0.05Å^{-1} (*d*-spacing = 4.03 Å), which is indexed by (010) reflection. The broad in-plane (100) and out-of-plane (010) reflection indicates that the planes of PTB7 aromatic backbones are roughly aligned parallel to the surface plane of substrate with the alkyl side chains directed toward the in-plane direction. This orientation is so-called 'face-on' orientation of PTB7 crystals. While the face-on orientation of PTB7 crystal is desired for high PCE, it is not the case in the blend films as addressed in the 2D GIWAXS patterns depicted in Figure 3.13b and c.

In the 2D patterns of the blend films, the observed (100) reflection rings imply random orientation of PTB7 crystals. The broad reflection halos centered at $q \approx$ 1.37 Å^{-1} (*d*-spacing = 4.7 Å), on the other hand, are attributed to the short range ordering of randomly oriented PC$_{71}$BM crystals, i.e., (311) reflection. The random orientation of PTB7 and PC$_{71}$BM crystals could possibly implicate that the growth process of oriented PTB7 and PC$_{71}$BM crystals are impeded by each other during film formation process. One of the most notable features (Figure 3.13d) is that the in-plane GIWAXS slices for PFN/PTB7:PC$_{71}$BM films, cast with and without DIO almost overlap with each other, indicating the same degree of crystallinity. Our results are in agreement with previous reports [99,102]. More importantly, the result indicates that the improved PCEs resulted from the DIO additive in neither the i-OSCs nor the c-OSCs based on PTB7:PC$_{71}$BM active layers are related to crystallinity and orientation morphology.

3.4 Conclusion

In summary, the nanoscale structural aspects of high PCE of PTB7:PC$_{71}$BM i-OSCs using PFN as the ITO modifier were investigated. SANS results of PTB7 and PC$_{71}$BM solutions indicate that both PTB7 and PC$_{71}$BM remain in completely dissolved states in both pristine DCB and DCB:DIO; no effect of DIO on the solution morphologies was identified. In the spun-cast films,

however, DIO was found to play a vital role in the morphological evolution occurring during the film formation process after spin-casting. In both i-OSCs and c-OSCs, the DIO, added to the casting solutions, induces the formation of much smaller PTB7 and $PC_{71}BM$ domains, which were revealed by cross-section TEM. The formation of smaller $PC_{71}BM$ domains form the basis for more efficient exciton transport to the $PTB7/PC_{71}BM$ interface and more effective charge separation at the interface. In i-OSCs, $PC_{71}BM$ was found to diffuse into the PFN layer as the casting solutions are spun-cast on top of the PFN layer, where more $PC_{71}BM$ diffusion occurs when DIO is added to the casting solutions. The increased $PC_{71}BM$ diffusion into the PFN layer increases the interfacial contact between $PC_{71}BM$ and PFN, and hence improves electron transport and collection at the cathode, increased the PCE.

Chapter 4: Morphology Engineering in Small Molecule-Based Organic Solar Cells

4.1 Small Molecule-Based OSCs

In this chapter, morphology engineering in a high-efficiency, small molecule-based bulk-heterojunction (BHJ) OSC system is discussed. Small molecules are known to be easier to purify, and the devices show better batch-to-batch reproducibility, higher crystallinity and better performance compared to their polymer-based counterparts [103-105]. Small molecule/fullerene [58,103,106-112] blends have shown promising results. The incorporated BHJ in this work [113] consists of small molecule (SM) 7,7′ -[4,4-bis (2-ethylhexyl)-4H-silolo[3,2-b:4,5-b′]dithiophene-2,6-diyl] bis[6-fluoro-4-(5′ -hexyl-[2,2′ -bithiophen]-5-yl)benzo[c][1,2,5]thiadiazole]) (p-DTS(FBTTh$_2$)$_2$) and PC$_{71}$BM, and the device structure is ITO/PEDOT:PSS/p-DTS(FBTTh$_2$)$_2$:PC$_{71}$BM/Ca/Al. Recently devices based this system have demonstrated PCEs as high as ~9% [58].

Recent advances in structural study of the polymer/fullerene system have identified the presence of mixed phases containing fullerene molecules dispersed in the donor phase [114,115]. While pure donor and acceptor phases reduce charge recombination by pushing holes away from electrons and, thus, enhancing device performances, the role of a third phase remains unclear [114,115]. Formation of the mixed phases may be expected in SM OSC as well as p-DTS(FBTTh$_2$)$_2$ and PC$_{71}$BM phase-separation during solidification. If one blending component prefers the air/film, bulk or film/substrate interface, it may lead to complex vertical phase stratification, including pure or mixed phases with a morphology different from bulk phase of BHJ. Thus, in addition to the in-plane structure, the vertical structure of the SM OSC should also

43

be investigated in detail. Highly penetrative and nondestructive neutron reflectometry is an ideal tool for profiling the buried phases and interfacial morphology of p-DTS(FBTTh$_2$)$_2$:PC$_{71}$BM blended films in the direction perpendicular to the film surface down to the substrate. The high contrast in neutron scattering length density (nSLD) between p-DTS(FBTTh$_2$)$_2$ (1.33×10^{-6} Å^{-2}) (see Section 4.2) and PC$_{71}$BM (4.3×10^{-6} Å^{-2}) [116] allows clear distinction of the components.

Here, neutron reflectometry was used to unfold the depth phase morphology of p-DTS(FBTTh$_2$)$_2$ and PC$_{71}$BM blend, and complemented with the use of absorption and photoluminescence spectroscopy, atomic force microscopy (AFM) and X-ray diffraction (XRD) characterizations to correlate the morphology to the OSC performance after thermal annealing and DIO additive processing. The obtained results reveal that depth profiles of SM-based systems are different from the polymer-based systems. The described approach here allows correlating the device performance with morphology, as well as to explain origin of various morphologies.

4.2 Experimental Section

4.2.1. Device Fabrication

p-DTS(FBTTh$_2$)$_2$ was purchased from 1-Material Inc., and used as received. A blend of p-DTS(FBTTh$_2$)$_2$ (21 mg) and PC$_{71}$BM (14 mg) was dissolved in CB (1 ml) with and without 0.25 vol.% DIO. Solutions were heated at 60 °C for several hours and at 90 °C for 15 min just before spin-casting. Devices were fabricated as follows: ITO substrates were cleaned as described in previous chapter (Section 3.2). Clean ITO substrates were then coated with PEDOT:PSS. The blend solution with or without DIO was spun-cast onto the PEDOT:PSS-coated substrates at 2000 rpm for 45 s. Films were allowed to dry for 20 min under inert atmosphere, and

subsequently annealed at 80 °C for 10 min. Films without DIO were annealed at either 80° or 100 °C for 10 min. Finally, 20 nm Ca and 80 nm Al were deposited on top of the active layers through a shadow mask by the thermal evaporation to complete the devices. The electrode area of the cells was 22.6 mm^2.

4.2.2. Device and Thin Film Characterization

The J–V characteristics of the prepared devices were measured by a Keithley 4200 semiconductor parameter analyzer under the AM 1.5 illumination. The morphological characterizations were done with blends of p-DTS(FBTTh$_2$)$_2$:PC$_{71}$BM BHJ spun-cast on sapphire (Al$_2$O$_3$) or quartz (SiO$_2$) substrates. To obtain the nSLD of pure p-DTS(FBTTh$_2$)$_2$, a solution of p-DTS(FBTTh$_2$)$_2$ (12 mg/ml) in CB was prepared and spun-cast onto silicon wafers. The NR experiments were performed at the Magnetism Reflectometer (BL 4A) and the Liquid Reflectometer (BL 4B) at the SNS, ORNL. The data were recorded on position sensitive detectors, and the reflected and scattered intensity signals were normalized to the intensity spectrum of the incident beam. The data are presented in 2D maps as a function of p_i and p_f where $p_i = 2\pi \sin\alpha_i/\lambda$ and $p_f = 2\pi \sin\alpha_j/\lambda$ are the perpendicular components of the neutron wave vectors. The specular reflectivities are extracted from these 2D intensity maps as a function of incident momentum transfer normal to the surface, $Q_z = p_i + p_j = 4\pi \sin\alpha_i/\lambda$. The experiential data is used to extract nSLDs.

XRD and XRR measurements were carried out on a high-resolution PANalytical X'Pert Pro MPD diffractometer with a Cu-K$_\alpha$ source ($\lambda = 1.5405$ Å). The XRD measurements were performed at 2.5–35 Å angular range with 0.04° step size and 0.5° scan speed. Standard single crystal silicon single crystal sample was used measured to calibrate the instrument. The

photoluminescence (PL) spectra were collected using a FluoroLog 3T fluorescence spectrometer, where the excitation monochromator was set at 320 nm and 580 nm.
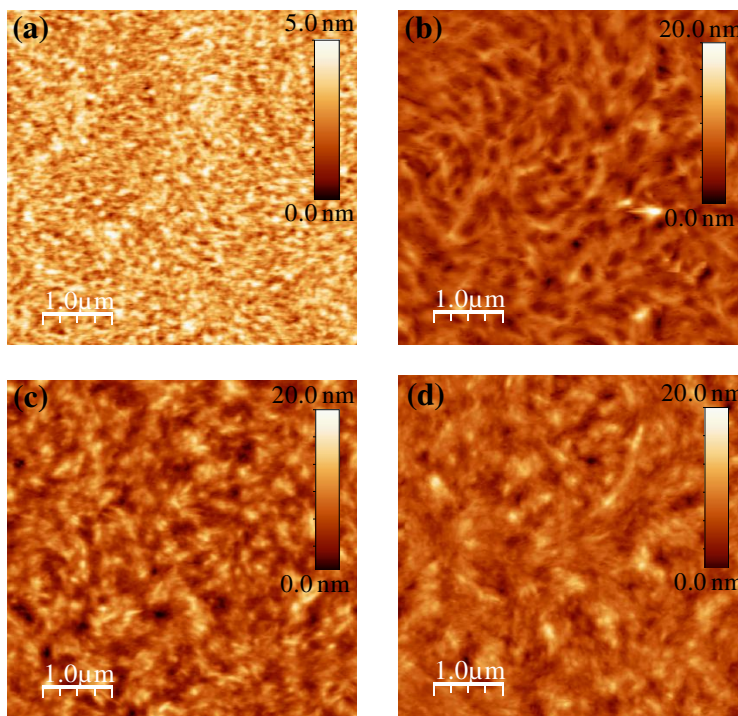
Figure 4.1. AFM images of p-DTS(FBTTh2)2:PC71BM films a) without DIO, b) without DIO annealed at 100 °C, c) with 0.25% DIO, and d) with 0.25% DIO annealed at 80 °C.

4.3 Results and Discussion

Thin films were prepared by spin-casting a solution of p-DTS(FBTTh$_2$)$_2$:PC$_{71}$BM (1.5:1 wt.%)-in-CB onto sapphire (Al$_2$O$_3$) or quartz (SiO$_2$) substrates. The surface morphologies of the coated films were investigated using AFM in tapping mode. As shown in **Figure 4.1**a, the surface of the as-cast sample consists of p-DTS(FBTTh$_2$)$_2$ and PC$_{71}$BM molecules in a random arrangement as a uniform mixture. The root mean square roughness (r_{RMS}) of the sample increases from 0.59 nm to 1.75 nm after thermal treatment (100 °C for 10 min, Figure 4.1b), and the surface of the

annealed film consists of domains approximately 500 nm to 1 μm long. On the other hand, the morphology of the film with 0.25 vol% DIO (Figure 4.1c) is drastically different from films without DIO, consisting of long wire-shape domains extending up to ~200 nm. After the thermal annealing (Figure 4.1d), the r_{RMS} of the film decreases from ~2.39 nm to ~2.27 nm.
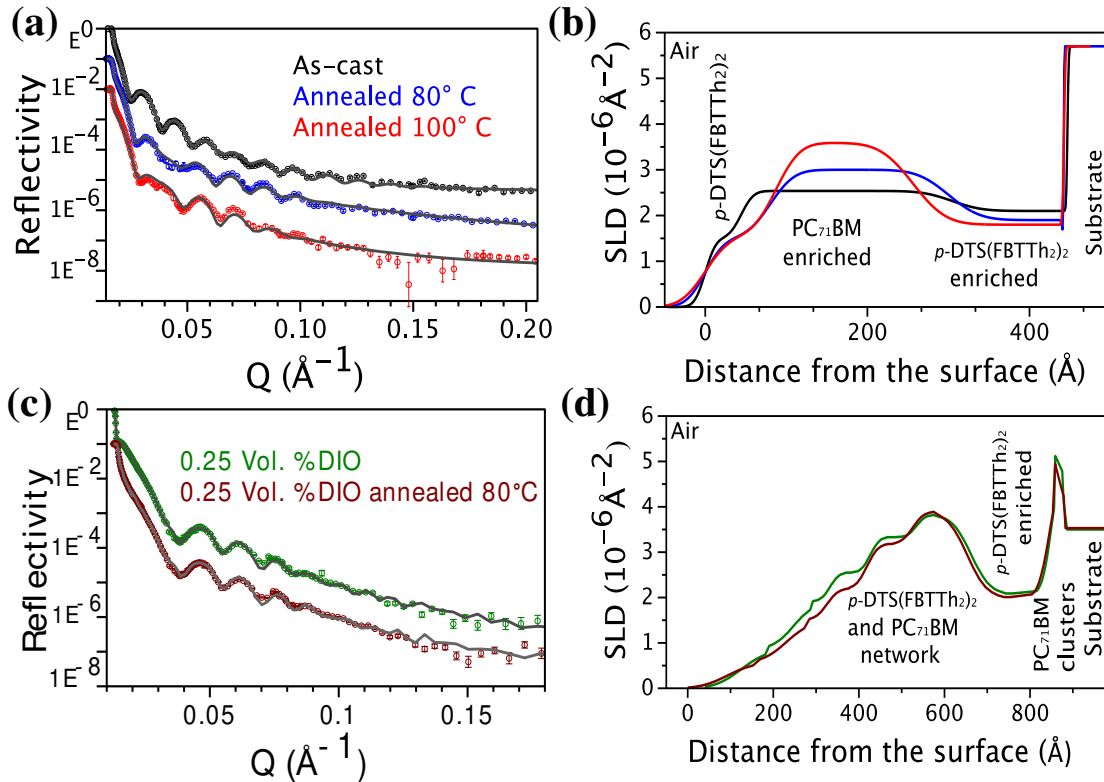
Figure 4.2. a) Experimental (shown as symbols) and modeled (solid lines) NR curves for as-cast and annealed (80 and 100 °C) Al_2O_3/p-DTS(FBTTh$_2$)$_2$:PC$_{71}$BM films without DIO. b) The SLD profiles as a function of distance from the surface obtained after fitting the experimental data shown in (a). c) Experimental (shown as symbols) and modeled (solid lines) NR curves for as-cast and annealed (80 °C) SiO_2/p-DTS(FBTTh$_2$)$_2$:PC$_{71}$BM films with 0.25 vol% DIO. d) The SLD profiles as a function of distance from the surface from fitting the experimental data of (c).

Figure 4.2 shows the NR data of p-DTS(FBTTh$_2$)$_2$:PC$_{71}$BM films, illustrating the vertical phase morphology. For devices, the active layer is usually spun-cast onto amorphous

PEDOT:PSS layers. However, in previously reported literatures, the NR studies have been performed using BHJ films grown directly on the substrates [97,117-119], which have similar surface properties as Al_2O_3 or SiO_2 substrates used in this work. Figure 4.2a shows experimental and modeled NR data for as-cast and thermally annealed films (at 80 °C and 100 °C) without DIO as a function of out-of-plane momentum transfer, Q_z. The associated fit of the data, obtained based on Parratt recursion formalism, is shown as solid line [101]. The value of neutron scattering length density (nSLD) for p-DTS(FBTTh$_2$)$_2$ was estimated to be 1.33×10^{-6} Å^{-2} (see Section 4.2). The nSLD of PC$_{71}$BM was found to be 4.34×10^{-6} Å^{-2} based on the bulk PCBM density of 1.5 g/cm^3 and neutron scattering lengths of the constituent elements [116].

Figure 4.2b shows the nSLD profiles of the best fit to the NR data. From the fits, the total thickness of the as-cast film was found to be ~45 nm. The nSLD profiles in Figure 4.2b reveal three distinct layers with the composition characterized by different nSLDs: 1) top surface layer in contact with the air/film interface, 2) a bottom layer interfacing with the substrate, and 3) a bulk layer sandwiched by the two interfacial layers. It also shows that the nSLD of the sandwiched layer increases with annealing temperature while that of the bottom layer decreases. The changes in nSLDs of the bulk and bottom layer are associated with the interdiffusion of p-DTS(FBTTh$_2$)$_2$ and PC$_{71}$BM. Remarkably, the nSLD of top interfacial layer remained almost unchanged regardless of thermal annealing. These results indicate that p-DTS(FBTTh$_2$)$_2$ prefers two interfacial regions, whereas, PC$_{71}$BM tends to diffuse to the bulk layer.

Figure 4.2c shows the NR profiles of as-cast and annealed p-DTS(FBTTh$_2$)$_2$:PC$_{71}$BM films prepared using 0.25 vol.% DIO. From the NR fits, the nSLD profiles were extracted and are depicted in Figure 4.2d. The nSLD profile of the as-cast film with 0.25 vol.% DIO is remarkably

different from the one without additive. Although it shows the presence of p-DTS(FBTTh$_2$)$_2$ enriched bottom interfacial layer, its width is about 3-4 times thinner than in the samples without DIO. Further thermal annealing of the film with DIO at 80 °C induces only small changes in the nSLD profile. This is different from the change in nSLD profile for as-cast p-DTS(FBTTh$_2$)$_2$:PC$_{71}$BM film and sample annealed at 80 °C (Figure 4.2b). It indicates that no significant interdiffusion of p-DTS(FBTTh$_2$)$_2$ and PC$_{71}$BM occurs by the thermal annealing. This observation is consistent with our AFM data where the films show densely packed structure with reduced surface roughness. Furthermore, at the bottom substrate/film interfaces, NR revealed a ~20 nm thick layer with a high nSLD value of ~6 × 10^{-6} Å^{-2} in both as-cast and annealed samples with DIO. The peaks correspond to high-density PC$_{71}$BM clusters formed in the samples with DIO [120]. Upon thermal annealing, the nSLD of the profile increased, resulting densely packed films.

These results show that presence of DIO results in much more evolved film morphology, which is close to the equilibrium state than that of the film spun-cast without DIO. Hence, thermal annealing only results in small refinement in the structure with negligible difference from as spun-cast film [97]. It is evident from the nSLD profiles that, for as-cast samples, accumulation of the ED material at the air/ film interface was enhanced with thermal annealing, which was previously observed using X-ray photon spectroscopy (XPS) for p-DTS(FBTTh$_2$)$_2$ material [121]. By contrast, polymer:fullerene blend systems exhibit accumulation of PCBM at film/substrate and air/film interfaces, which is believed to be responsible for enhanced electron extraction [117,122]. Hence, the layer morphology of p-DTS(FBTTh$_2$)$_2$:PC$_{71}$BM appears very different from polymer:fullerene blend systems.

The structural evolution of SM in solutions and films can be correlated with the changes in electronic and photoluminescence (PL) spectra. The broad absorption peaks at 390 and 600 nm were assigned to p-DTS(FBTTh$_2$)$_2$ solution in CB, PC$_{71}$BM to π–π* transition of p-DTS(FBTTh$_2$)$_2$, while 370 nm and 460 nm peaks were ascribed to the PC$_{71}$BM (**Figure 4.3**a). Upon spin-casting of the p-DTS(FBTTh$_2$)$_2$:PC$_{71}$BM solution into film, a bathochromic shift of all absorption peaks is observed. As-cast thin film exhibits 550, 615 and 680 nm broad vibronic peaks of π–π stacked p-DTS(FBTTh$_2$)$_2$ aggregates, assigned to A0→2, A0→1 and A0→0 transitions respectively [123]. The ratio of A0→1/A0→0 > 1 is indicative of dominating inter-chain coupling in π–π stacked p-DTS(FBTTh$_2$)$_2$ aggregates [123].
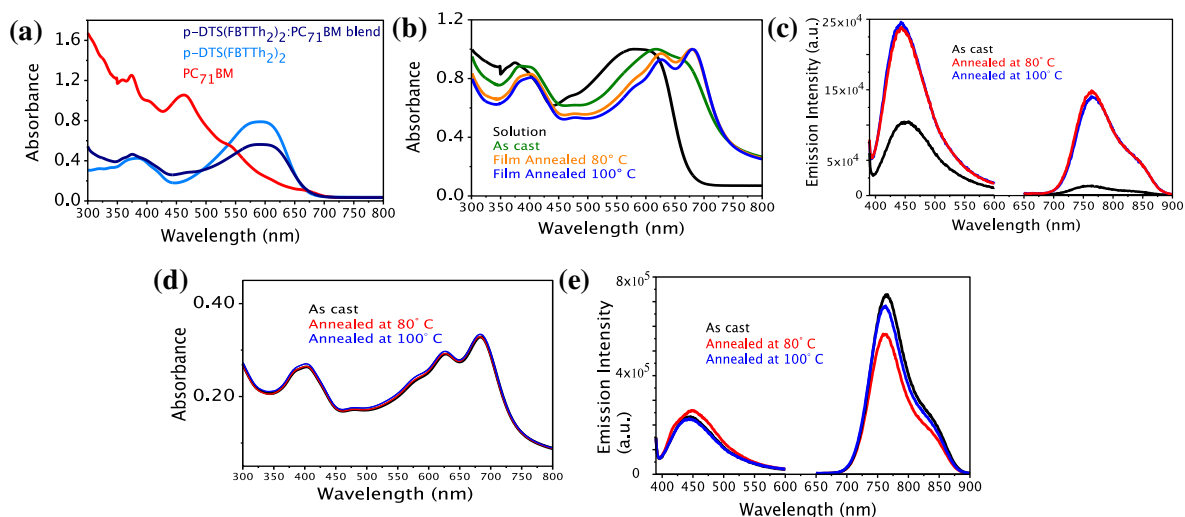
Figure 4.3. a) UV-Visible absorption spectra of pure p-DTS(FBTTh$_2$)$_2$, PC$_{71}$BM and blend of p-DTS(FBTTh$_2$)$_2$:PC$_{71}$BM in CB. b) Absorption spectra of p-DTS(FBTTh$_2$)$_2$:PC$_{71}$BM blend solution and cast films under thermal annealing. The absorption intensities are normalized. c) Photoluminescence spectra of as-cast p-DTS(FBTTh$_2$)$_2$:PC$_{71}$BM film after thermal annealing at 80 °C and 100 °C. d) UV-Visible absorption and e) photoluminescence spectra of p-DTS(FBTTh$_2$)$_2$:PC$_{71}$BM with 0.25 vol.% DIO after thermal annealing at 80 °C.

Upon thermal annealing at 80 °C and 100 °C, the A0→2, A0→1 and A0→0, vibronic peaks become more pronounced and show small bathochromic shift, indicative of an enhanced crystalline ordering in SM aggregates. The reduced intensity of ratio of A0→1/A0→0 < 1 is usually attributed to planarization of p-DTS(FBTTh$_2$)$_2$ molecules, with intra-chain interactions dominating over inter-chain coupling in SM aggregates. The PL spectra of the p-DTS(FBTTh$_2$)$_2$:PC$_{71}$BM film show two broad emission bands with maxima at 460 nm (2.7 eV) and 765 nm (1.6 eV), when excited at 320 nm and 580 nm, respectively. The 1.6 eV emission correlates with the transition between LUMO and HOMO of p-DTS(FBTTh$_2$)$_2$ aggregates, while the 2.7 eV band was assigned to the transition from LUMO$_{p-DTS(FBTTh2)2}$ to HOMO$_{PC71BM}$ [58]. Annealing leads to increased PL intensity of 1.6 eV and 2.7 eV peaks, which correlates well with the changes in absorption spectra, and is probably related to the increase in p-DTS(FBTTh$_2$)$_2$ aggregate π–π stacking and the structure of p-DTS(FBTTh$_2$)$_2$:PC$_{71}$BM interface, respectively.

The absorption spectra of as-cast and annealed p-DTS(FBTTh2)2:PC71BM films are shown in Figure 4.3d. In addition to a broad ~400 nm peak, a progression of vibronic peaks was detected at 580 nm, 625 nm, and 680 nm, which are assigned to A0→2, A0→1, and A0→0 transitions, respectively. The ratio of A0→1 to A0→0 peak intensities was found to be less than one which does not change upon annealing, indicating that high order of π–π stacking and molecular planarization in SM aggregate in the presence of DIO are achieved already at room temperature. PL spectra show same peaks without DIO. However, while the intensity of broad 2.7 eV peak did not change, the intensity of low energy emission peak at 1.6 eV increased by a factor of five compared to annealed p-DTS(FBTTh$_2$)$_2$:PC$_{71}$BM films without DIO. The improved PL intensity indicates that defect-related non-radiative transition is suppressed in the case of DIO

containing films, due to better ordering of SM aggregates. Both electronic absorption and PL spectra of annealed DIO containing p-DTS(FBTTh$_2$)$_2$:PC$_{71}$BM films show that thermodynamically metastable molecular ordering was achieved already at room temperature. This metastable molecular ordering is consistent with the unchanged vertical phase morphology of DIO containing p-DTS(FBTTh$_2$)$_2$:PC$_{71}$BM films observed in NR experiments.
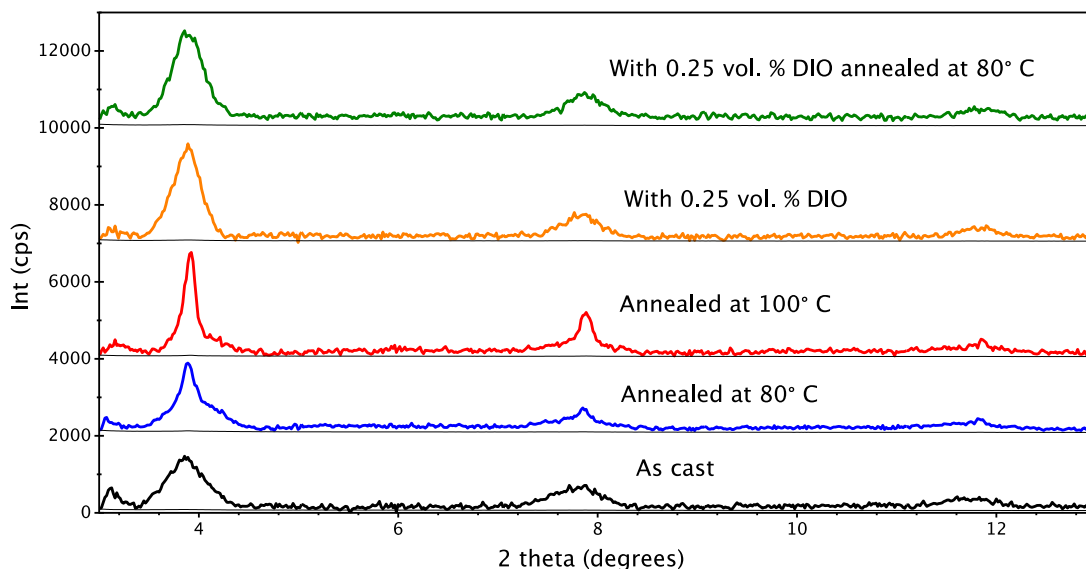
Figure 4.4: Out-of-plane XRD scans of *p*-DTS(FBTTh$_2$)$_2$:PC$_{71}$BM blends with peaks at 2θ = 3.98°, 7.88° and 11.90°. With thermal annealing, the intensity of the peaks is enhanced. Addition of 0.25 vol % DIO generated broader peak with higher intensities.

To gain insights into the effect of DIO and thermal annealing on the molecular packing and crystallinity of p-DTS(FBTTh$_2$)$_2$:PC$_{71}$BM films, we conducted X-ray diffraction (XRD) measurements. **Figure 4.4** shows XRD patterns for as-cast and annealed films with and without DIO. All films exhibit a peak at *2θ* = ~3.90°, which is associated with the (001) reflection of p-DTS(FBTTh$_2$)$_2$ crystal. Higher order (002) and (003) reflections observed at ~7.88°, and ~11.74° manifests that a fraction of p-DTS(FBTTh$_2$)$_2$ chains are highly-ordered aggregates within films

[124]. Upon annealing of thin films, the XRD peak intensity and sharpness increase, indicating an increase in ordering of p-DTS(FBTTh$_2$)$_2$ aggregates. Using the Scherrer equation, the size of crystalline domain of SM aggregate was calculated along with the peak areas for (001) reflection of p-DTS(FBTTh$_2$)$_2$ crystal (**Table 4.1**). The crystalline domain size in as-cast films were found to be ~22.8 nm, which increases to 41.2 nm and 134.7 nm after thermal annealing at 80 °C and 100 °C, respectively. The integrated (001) peak area of the sample annealed at 100 °C is greater than that of the as-cast sample, suggesting an increased population of crystalline domains of p-DTS(FBTTh$_2$)$_2$ in the annealed p-DTS(FBTTh$_2$)$_2$:PC$_{71}$BM film (Table 1). Remarkably the integrated area of (001) peak of as-cast p-DTS(FBTTh$_2$)$_2$:PC$_{71}$BM films with DIO is about three times larger than that without DIO. Interestingly, the crystalline domain size of sample is ~24.6 nm, which is a ~2 nm increase to that of film without DIO. It is concluded that DIO drastically increases the population of p-DTS(FBTTh$_2$)$_2$ crystal domains already in as-cast films, and only slightly increases the crystal domain size. Thermal annealing of DIO-containing p-DTS(FBTTh$_2$)$_2$:PC$_{71}$BM films increases the size and the population of p-DTS(FBTTh$_2$)$_2$ crystalline domains. It was also observed that the size of crystalline domains in annealed (80 °C) DIO-containing p-DTS(FBTTh$_2$)$_2$:PC$_{71}$BM films is smaller by a factor of 1.6 compared to that in annealed p-DTS(FBTTh$_2$)$_2$:PC$_{71}$BM films without DIO while the population of crystals increases by a factor of 3. Larger crystal domain size in annealed p-DTS(FBTTh$_2$)$_2$:PC$_{71}$BM films suggests that excitons have to travel longer distances to reach D/A interface, which is detrimental for achieving high PCEs.

Table 4.1. Peak area and the crystallite sizes for p-DTS(FBTTh$_2$)$_2$ (001) reflection.

Sample	Normalized Peak Area	Crystallite size (nm)
Without DIO As-cast	2205	22.8
Without DIO, annealed at 80° C	2358	41.2
Without DIO, annealed at 100° C	3189	134.7
With 0.25V% DIO, as-cast	6687	24.6
With 0.25V% DIO anneal at 80° C	7386	26.4

Figure 4.5 shows the *J-V* curves of p-DTS(FBTTh$_2$)$_2$:PC$_{71}$BM solar cells under AM 1.5G irradiation. The photovoltaic parameters, i.e., J_{SC}, V_{OC}, FF, and PCE are listed in **Table 2**. The device consisting of p-DTS(FBTTh$_2$)$_2$:PC$_{71}$BM active layer shows relatively low value of PCE, about 2.1%. After thermal annealing, the PCE increases to 3.2% at 80 °C and 3.5% at 100 °C. DIO-containing p-DTS(FBTTh$_2$)$_2$:PC$_{71}$BM devices show higher performance with PCE of 4.9% for as-cast active layer, which increases to 5.3% after annealing at 80 °C. The improved performance of DIO-containing devices is because the additive induces crystallization of size of SM aggregates with better spectral response as indicated by increase in PL [125].
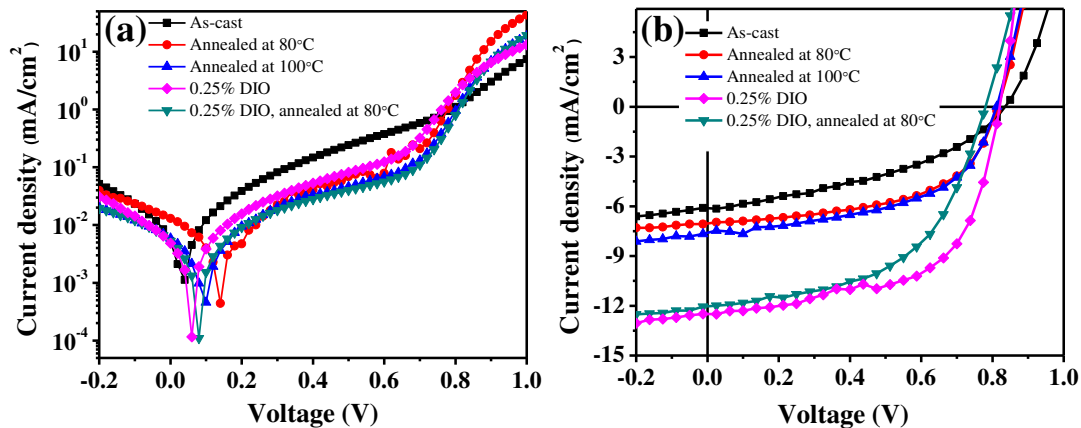
Figure 4.5. *J−V* characteristics of the p-DTS(FBTTh$_2$)$_2$:PC$_{71}$BM solar cells at different processing conditions under a) dark and b) AM 1.5G irradiation (100 mW/cm^2).

Table 4.2. Electrical Parameters of p-DTS(FBTTh$_2$)$_2$:PC$_{71}$BM solar cells at different processing conditions.

Device	J$_{SC}$ (mA/cm^2)	V$_{OC}$ (V)	FF (%)	PCE$_{avg}$ (%)
w/o DIO, as-cast	6.7	0.81	37.9	2.1 ± 0.3
w/o DIO, annealed at 80° C	7.6	0.81	51.4	3.2 ± 0.3
w/o DIO, annealed at 100° C	7.9	0.81	54.6	3.5 ± 0.3
w/ 0.25V% DIO, as-cast	11.7	0.78	54.2	4.9 ± 0.1
w/ 0.25V% DIO annealed 80° C	12.0	0.76	58.2	5.3 ± 0.4

4.4 Conclusion

The thermodynamically stable p-DTS(FBTTh$_2$)$_2$:PC$_{71}$BM BHJs obtained by thermal annealing are different in lateral and depth phase morphology and crystallinity from BHJs obtained with a DIO additive. Through an energy-level analysis on the absorption and emission spectra of the films, the different functions of thermal or DIO treatment to the $\pi-\pi$ stacking in p-DTS(FBTTh$_2$)$_2$ aggregates and the interaction at p-DTS(FBTTh$_2$)$_2$:PC$_{71}$BM interface have also been revealed. The three-layer vertical phase morphology was observed for the films after thermal annealing. By contrast, DIO additive processing generates more evolved film morphology, which is closer to the equilibrium state. nSLD chemical/structural profiles obtained from NR data show more densely packed structures, which are consistent with the AFM images. Formation of well-mixed ED and EA regions at the surface of the film facilitates the efficient charge transfer to the device. According to XRD data, the DIO additive morphology exhibits a high density of small donor nanocrystallites of ~24 nm, whereas thermal annealing generates smaller amount of much larger crystallites (~134 nm). DIO promotes the formation of a large density of p-DTS(FBTTh$_2$)$_2$ small nanocrystals arranged in an elongated network throughout the

thickness of the active layer, which results in the enhancements of solar cell performance due to the formation of nanocrystallites with the domain size comparable to the maximum exciton diffusion length. This is favorable for device efficiencies, since they stimulate efficient exciton diffusion (less probable to recombine) to an ED/EA interface and provide a larger ED/EA interfacial area for exciton dissociation. The findings demonstrate the role and impact of DIO and thermal treatment on the morphology of small molecule BHJ and take us a step closer to fully controlling the performance of photovoltaic devices.

Chapter 5: Perovskite Solar Cells by Ultrasonic Spray-Coating

This chapter describes the fabrication of perovskite solar cells (PSCs) by exploring a high-throughput ultrasonic spray-coating. Perovskite films with high uniformity, crystallinity, and surface coverage were obtained in a single step. The USC processing was also used on TiO_2/ITO-coated polyethylene terephthalate (PET) substrates to realize flexible PSCs that are robust under mechanical stress. In this case, a photonic curing technique was used to achieve a highly-conductive TiO_2 layer on flexible PET substrates for the first time. The high device performance and reliability obtained by the combination of USC processing with optical curing appears very promising for roll-to-roll manufacturing of high-efficiency, flexible PSCs.

5.1 Motivation and Research Goal

The performance of PSCs highly depends on perovskite film quality and morphology. To achieve high-quality perovskite films, a variety of deposition techniques, such as thermal evaporation [61,126,127], single-step spin-coating [77,128], layer-by-layer or two-step coating [68,129], and vapor-assisted [130] processes have been developed. However, one major disadvantage of most laboratory-scale techniques is that they are incompatible with low-cost, roll-to-roll processing envisioned for large-scale manufacturing. Existing scalable processing techniques include ink-jet printing, slot-die coating, blade-coating, screen-printing, and ultrasonic spray-coating [78,131-137].

Among the cost-effective roll-to-roll compatible processes, USC is one of the most promising that has been successfully exploited for the fabrication of various organic electronic devices including light emitting diodes [138], photovoltaics [139-140], photodetectors [141], and field-

effect transistors [142]. The overall advantage of USC is its ability to simultaneously provide high throughput, better directional control, efficient use of materials, uniform film coverage, and compatibility with variety of substrates, with the potential for the deposition of continuous layers without dissolution of underlying layers [139,142-144]. Recently, the USC process was demonstrated to deposit perovskite thin films on glass substrates, and the resulting PSCs showed an average PCE of 7.8% [145]. In this work, a USC processing was developed for the synthesis of highly-crystalline and uniform perovskite ($CH_3NH_3PbI_{3-x}Cl_x$) films. Considering the diverse application potential, it is also highly important to be able to fabricate high-performance devices on light-weight and flexible substrates using scalable techniques. So far, one major challenge for the fabrication of solar cells on plastic substrates is their incompatibility with high temperature. Typically, the fabrication of high-performance PSCs, particularly those based on compact TiO_2 electron-transporting layers, involves a high temperature (~ 500 °C) sintering process to increase the crystallinity of TiO_2 [61,64,71]. In this work [146], to realize flexible solar cells, an optical curing technique that is compatible with roll-to-roll processing was used to achieve conductive TiO_2 layers on ITO-coated PET substrates at low processing temperatures.

5.2 Experimental Section

5.2.1 Material, Solution, and Substrate Preparation

TiO_2 solution for the electron transport layer was synthesized by adding 365 µl of titanium isopropoxide into 5 ml of anhydrous IPA in the presence of 70 µl 1M hydrochloric acid (HCl), and stirring vigorously for 2h, and filtered using a 0.2 µm pore size PTFE filter [77]. $CH_3NH_3PbI_{3-x}Cl_x$ precursors, methylammonium iodide (MAI) and lead chloride ($PbCl_2$) were purchased from 1-Material and Sigma Aldrich, respectively, and used as received. MAI was

mixed with $PbCl_2$ (3:1 molar ratio), and dissolved in anhydrous N,N-dimethylformamide (DMF) for a total concentration of 10 wt%. Hole transport material, 2,2′,7,7′-tetrakis-(N,N-di-pmethoxyphenylamine) 9,9′-spirobifluorene (Spiro-OMeTAD, 1-Material) was dissolved in CB for a concentration of 90 mg/ml, and doped with 45 µl lithium-bis(trifluoromethanesulfonyl)-imide (LiTFSI) solution (170 mg/ml in acetonitrile) and 10 µl of 4-tertbutylpyridine (tBP) solution. Both LiTFSI and tBP were purchased from Sigma-Aldrich, and used as received. ITO-coated glass (15 Ω/□, patterned) and PET (60 Ω/□) were used as substrates. PET substrates were patterned by immersing them into a solution of deionized (DI) water, nitric acid (HNO$_3$), and HCl at a 4:1:3 ratio for 7 min under heavy stirring. Subsequently, they were rinsed with clean DI water. Both glass and PET substrates were cleaned using the previously described procedure.

5.2.2 Device Fabrication

The as-prepared TiO$_2$ solution was spin-coated onto UV-ozone-treated ITO-coated glass and PET substrates at 2000 rpm for 40 s in air. Subsequently, glass substrates were annealed at 500 °C in a muffle furnace for 30 min. For the PET substrates, the TiO$_2$ films were annealed by exposing them to five infrared pulses under a radiant exposure of 17.3 J/cm^2 from a plasma arc lamp for 2 ms pulse dwell time using a PulseForge 3300 processing system from NovaCentrix. The CH$_3$NH$_3$PbI$_{3-x}$Cl$_x$ solution was spray-coated onto TiO$_2$/ITO-coated glass and PET substrates in ambient air using an ExactaCoat system (Sono-Tek Corporation) equipped with a 120-kHz nozzle. Substrates were kept at 75 °C during coating under optimized USC process, i.e., a path speed of 100 mm/s, a nozzle height of 5 cm, an atomizing gas pressure of 2.6 psi, and an infusion rate of 3.2 ml/min. After drying, the films were annealed at 100 °C for 1h in air. For spin-coated devices, a 40 wt% CH$_3$NH$_3$PbI$_{3-x}$Cl$_x$ solution was spin-coated onto TiO$_2$/ITO-coated glass and

PET substrates at 3000 rpm for 45 s, and subsequently annealed at 100°C for 1 h. The as-prepared Spiro-OMeTAD solution was spin-coated at 2000 rpm for 30 s on top of $CH_3NH_3PbI_{3-x}Cl_x$ films, and left in a desiccator overnight for doping. Finally, 100 nm-Ag layer was thermally deposited at 1 Å/s to complete the devices with an area of 6.5 mm^2 each.

5.2.3 Film and Device Characterization

Current-voltage (*J-V*) curves of the fabricated solar cells were measured by scanning from forward bias to reverse bias (1.2 V to -0.2 V) direction and vice versa after ~ 120 s initial light soaking time, under the AM 1.5G conditions. The voltage step during the scan was fixed at 35 mV with a delay time of 50 ms. EQE and XRD were done using previously described procedures. The film morphology was studied by Zeiss Merlin VP scanning electron microscope (SEM). Film thickness measurement was carried out using a KLA-Tencor profilometer.

5.3 Results and Discussion

Figure 5.1a schematically shows the USC process, where the solution is fed through a programmable syringe pump and sprayed using a 120-kHz ultrasonic nozzle. The nozzle atomizes the solution into micrometer-size droplets with the help of an atomizing nitrogen-gas pressure that prevents clogging of the solution in the nozzle-head. In this work, a solution mixture of MAI and $PbCl_2$ was ultrasonically spray-coated on various substrates, and then the obtained films were thermally annealed at 100 °C for 1 h in air to drive the chemical reaction and crystallization. The annealed, spray-coated films show strong and sharp Bragg peaks (Figure 5.1b) at 14.03° and 28.38°, corresponding to (110) and (220) planes, respectively, indicating the formation of highly crystalline tetragonal perovskite film [67,145].
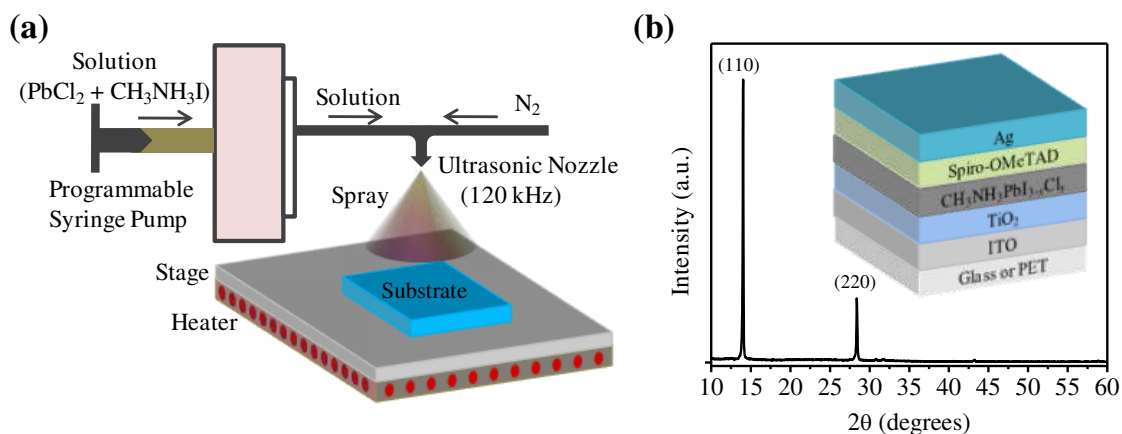
Figure 5.1. a) Schematic diagram of ultrasonic spray-coating process. b) XRD pattern of a spray-coated CH₃NH₃PbI₃₋ₓClₓ film. The inset of b) schematically shows the device architecture.
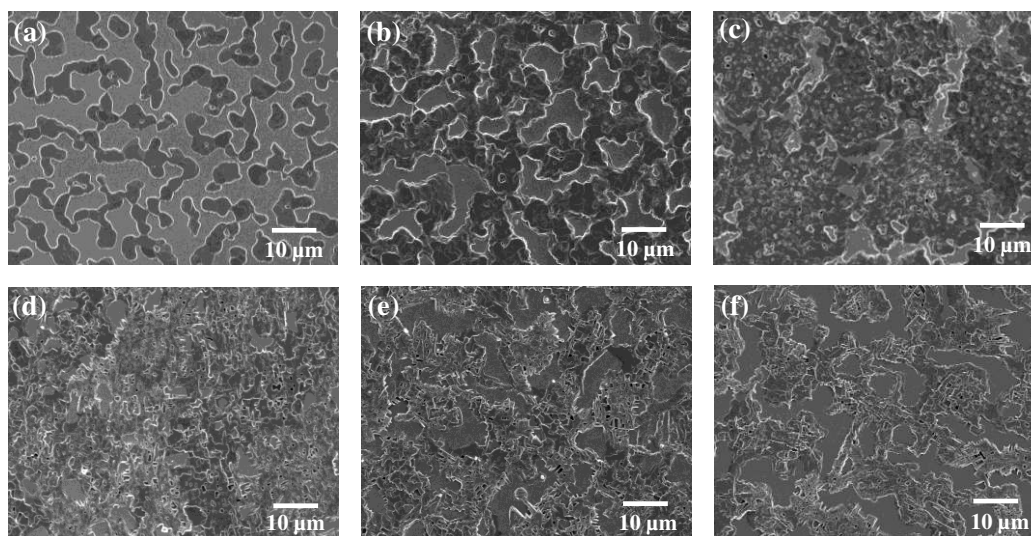
Figure 5.2. SEM images of spray-coated perovskite films on TiO₂/ITO/glass substrates at different substrate temperatures: a) 26 °C, b) 45 °C, c) 60 °C, d) 75 °C, e) 90 °C, and f) 105 °C.

In order to achieve high-quality perovskite films for high-performance devices, the USC process was optimized by comparing different solvents, tuning the substrate temperature, and optimizing the perovskite film thickness. To examine the effect of solvent, two solvents with different boiling points were used: DMF (boiling point = ~153 °C) and dimethyl sulfoxide (DMSO, boiling point = ~189 °C). High boiling points of these solvents result in prolonged

61

drying times (~15 min for DMF and ~25 min for DMSO) for the coated films. To minimize the drying time, elevated substrate temperatures were used in conjunction with lower boiling point solvent, DMF. SEM image (Figure 5.2a) shows that the film, spray-coated on TiO_2/ITO/glass substrate at room temperature (26 °C), exhibits low surface coverage due to the dewetting caused by the prolonged drying time. As shown in Figure 5.2b-f, elevated substrate temperatures result in improved film coverage by reducing the surface tension of the wet film, however temperatures > 90 ℃ again result in lower film coverage due to immediate drying of the solution upon reaching the substrate.
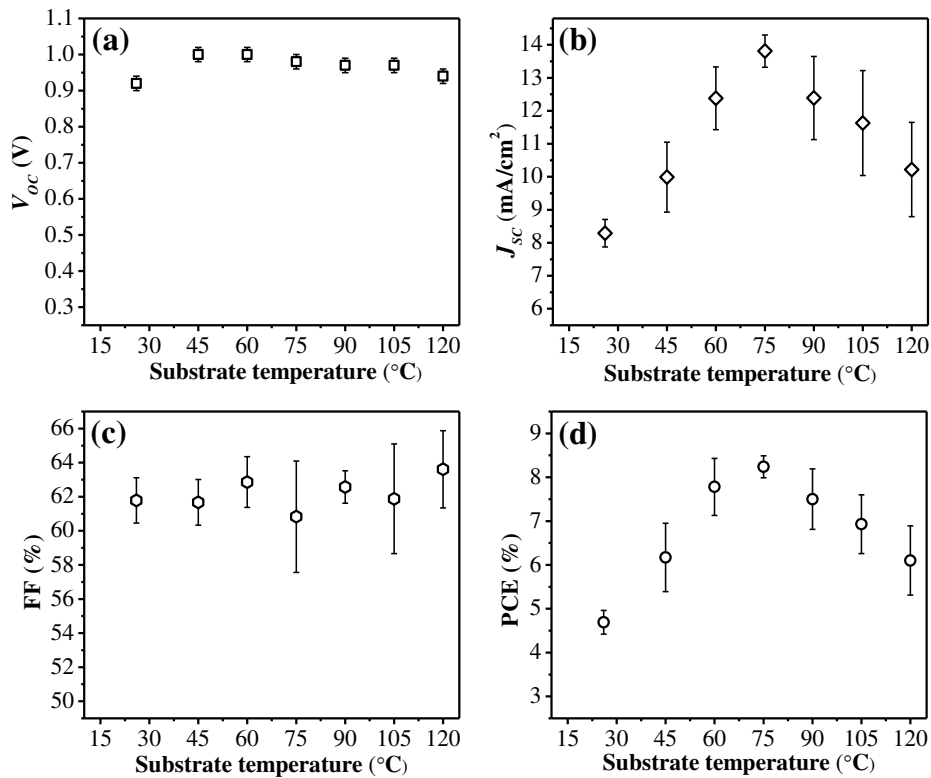
Figure 5.3. Device performance parameters, i.e., a) V_{OC}, b) J_{SC}, c) FF, d) PCE at different substrate temperatures. Device performance from 120 °C is included to illustrate the trend.

Figure 5.3 shows the variation of device performance corresponding to these changing substrate temperatures. Though the V_{OC} and FF exhibit negligible difference with increasing substrate temperature, the J_{SC} reaches the highest, 13.8 mA/cm^2, at 75 °C, which corresponds to the perovskite films with the highest surface coverage on the TiO$_2$ layer.
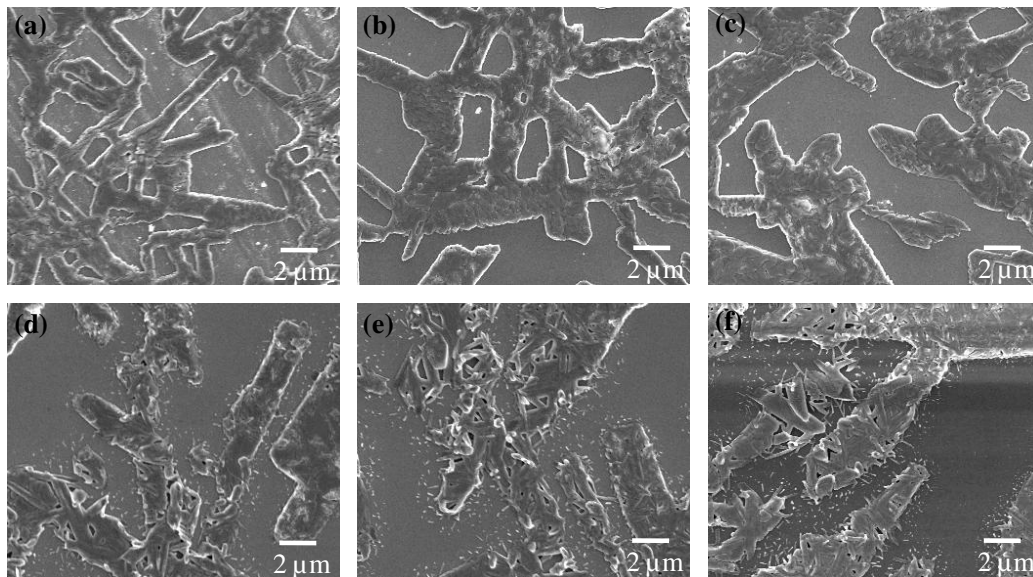
Figure 5.4. SEM images of a perovskite films coated using DMSO on TiO$_2$/ITO/glass substrates at substrate temperature of (a) 60 °C (b) 75 °C, (c) 90 °C, (d) 105 °C, (e) 120 °C, and (f) 130 °C.

By comparison, films coated using a relatively high boiling point solvent DMSO exhibit lower surface coverage (**Figure 5.4**) compared to the films coated using DMF (Figure 5.2). These differences are reflected in the device performance, as shown in **Table 5.1**. The DMSO-solvent-processed perovskite films result in an average PCE of only 4.2%, whereas DMF-processed films show an average PCE of 8.2%, a 95% enhancement. This large efficiency enhancement is mainly ascribed to significant enhancements in J_{SC} and V_{OC} by 59% and 23%, respectively, which result from the fast evaporation of low-boiling-point solvent DMF, leading to

fast crystalliation and better surface coverage of $CH_3NH_3PbI_{3-x}Cl_x$ films [128,145]. For the subsequent optimization of the USC process described below, therefore, the substrate temperature was fixed at 75 °C, and DMF was used as the solvent.

Table 5.1. Comparison of device performance based on perovskite films spray-coated using DMF and DMSO at a substrate temperature of 75 °C.

Solvent	J_{SC} [mA/cm^2]	V_{OC} [V]	FF [%]	PCE$^*_{avg}$ [%]
DMF	13.8 ± 0.5	0.98 ± 0.02	60.8 ± 3.3	8.2 ± 0.3
DMSO	8.7 ± 1.6	0.80 ± 0.06	60.6 ± 3.2	4.2 ± 0.5

*Average is based on eight devices, measured under AM 1.5G illumination conditions.

Table 5.2. Device parameters of the PSCs fabricated with different perovskite film thicknesses.

Infusion rate (ml/min)	Solution Concentration (wt%)	Film thickness (nm)	J_{SC} [mA/cm^2]	V_{OC} [V]	FF [%]	PCE$^*_{avg}$ [%]
2.6	8	15.6 ± 1.9	1.03 ± 0.05	62.0 ± 1.6	10.0 ± 2.0	15.6 ± 1.9
2.6	10	16.0 ± 2.6	0.98 ± 0.07	64.0 ± 1.2	10.1 ± 2.3	16.0 ± 2.6
3.2	10	19.3 ± 0.7	0.97 ± 0.03	60.8 ± 2.2	11.4 ± 0.3	19.3 ± 0.7
2.6	12	16.8 ± 0.9	0.97 ± 0.02	61.4 ± 1.8	10.0 ± 0.2	16.8 ± 0.9
3.2	12	17.1 ± 2.2	0.97 ± 0.10	59.4 ± 8.0	9.9 ± 2.4	17.1 ± 2.2
4.4	12	17.2 ± 1.7	0.95 ± 0.06	59.6 ± 5.0	9.7 ± 2.0	17.2 ± 1.7

*Average PCEs are based on eight devices with each thickness.

To further enhance the device performance, the perovskite film thickness was further optimized by varying the solution concentration and infusion rate. Two important observations are shown as shown in **Table 5.2**. First, the film roughness increases with increasing the thickness of perovskite films. Second, the variation of film thickness primarily impacts the J_{SC}. We found that the J_{SC} steadily increases with increasing the thickness, which is due to enhanced optical absorption. The highest J_{SC} of 19.3 mA/cm^2 and thus the highest PCE of 11.4 ± 0.4 % are

reached when the film thickness is increased to 295 ± 33 nm. However, the J_{SC} decreases with further increasing the thickness, probably due to higher charge recombination [79,129,147].
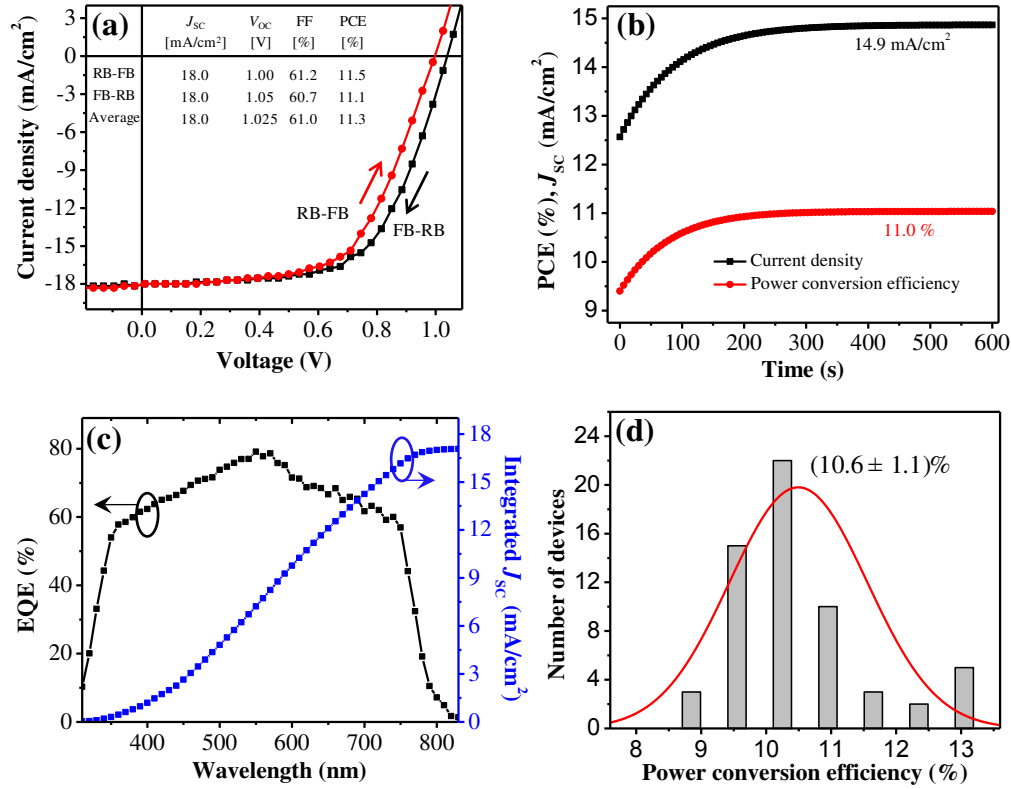
Figure 5.5. (a) *J-V* curve of a typical PSC on glass substrate at different scanning directions. (b) Current density and PCE as a function of time for the same device held at 0.75 V forward bias. (c) EQE spectrum and integrated J_{SC} from the corresponding device under short circuit conditions. (d) Histogram of PCEs measured for 60 devices, fabricated with optimized USC process. Gaussian fit is provided as a guide to eyes.

To correlate the USC process optimization with the device performance and also provide a measure of reproducibility, a series of devices were fabricated on glass substrates. The *J-V* curve of a typical PSC is shown in **Figure 5.5**a, with a J_{SC} of 18 mA/cm^2, V_{OC} of 1.05 V, FF of 60.7%, and PCE of 11.5% at forward bias (FB) to reverse bias (RB) scanning direction and a J_{SC} of 18 mA/cm^2, V_{OC} of 1.00 V, FF of 61.2%, and PCE of 11.1% at RB-FB direction, under AM 1.5G

(100 mW/cm^2) illumination, measured in a nitrogen-filled glovebox. The small hysteresis may be attributed to use of planer device architecture [82,148]. In order to better evaluate the performance, the stabilized current density and power output (Figure 5.5b) of this device were determined by measuring current density at around maximum power point (~ 0.75 V), which gives a similar PCE of 11%. The EQE spectrum of the same device measured in air without encapsulation is shown in Figure 5.5c, where integrating the EQE curve over the spectral range (AM 1.5G) yielded J_{SC} of 17.14 mA/cm^2, ~4.7% lower than the J_{SC} extracted from J-V characteristics, which could be due to the mismatch in two different solar spectra [70] or instability of Spiro-OMeTAD in air [149]. To demonstrate statistical significance of the high device performance obtained by process optimization, Figure 5.5d shows a PCE histogram of 60 devices fabricated on glass substrates using the optimized process. The most efficient cell exhibits a J_{SC} of 20.6 mA/cm^2, V_{OC} of 1.03 V, FF of 61. 6%, and PCE of 13% (**Figure 5.6**a). These devices demonstrate an average PCE of (10.6 ± 1.0)%, which is comparable to that of the devices fabricated by spin-coating (Figure 5.6b).

The excellent device performance discussed above encouraged us to fabricate devices on flexible and light-weight PET substrates. Instead of the high-temperature annealing (~ 500 °C) of the TiO$_2$ films used for glass substrates [61,64,71], we used a photonic curing technique (**Figure 5.7**) to achieve conductive TiO$_2$ films on ITO/PET substrates, where the TiO$_2$ films are exposed to five to ten high-density infrared (HDI) light pulses from a high-intensity plasma arc lamp for short dwell times of 1-2 ms. This technique, also called pulse-thermal processing (PTP), is a HDI processing technology based radiant heat treatment technique that can deliver a peak sintering power up to 20,000 W/cm^2 during a millisecond, and is used to rapidly anneal thin films of

various materials without damaging underlying plastic substrates [150,151].This tool enables reproducible, roll-to-roll, high-temperature processing of thin-film materials on low-temperature substrates. **Figure 5.8**a shows the simulated temperature-versus-time profile for the photonic curing technique used to anneal TiO_2 films on PET substrates. Figure 5.8b shows the *J-V* curves for the best devices with as-casted, thermally-annealed, and photonic-cured TiO_2 films.
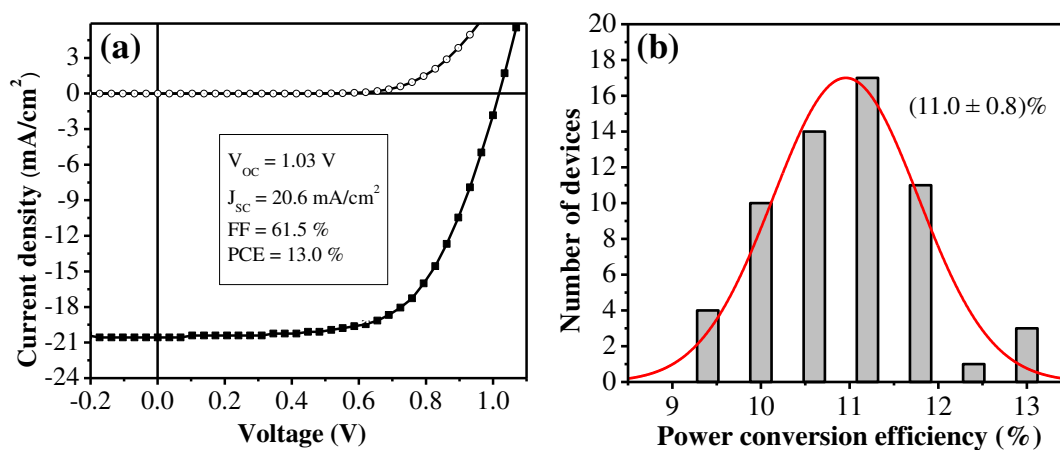
Figure 5.6. (a) *J-V* curves of the champion device under dark and AM 1.5G illumination conditions. (b) Histogram of 60 spin-coated PCEs, showing an average PCE of $(11.0 \pm 0.8)\%$.
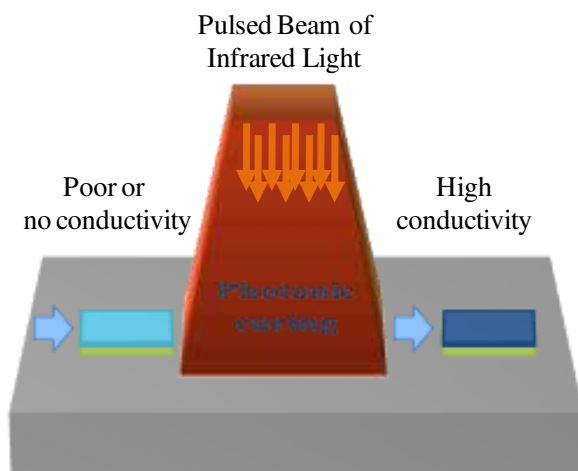
Figure 5.7. Schematic of the photonic curing technique used in this work.
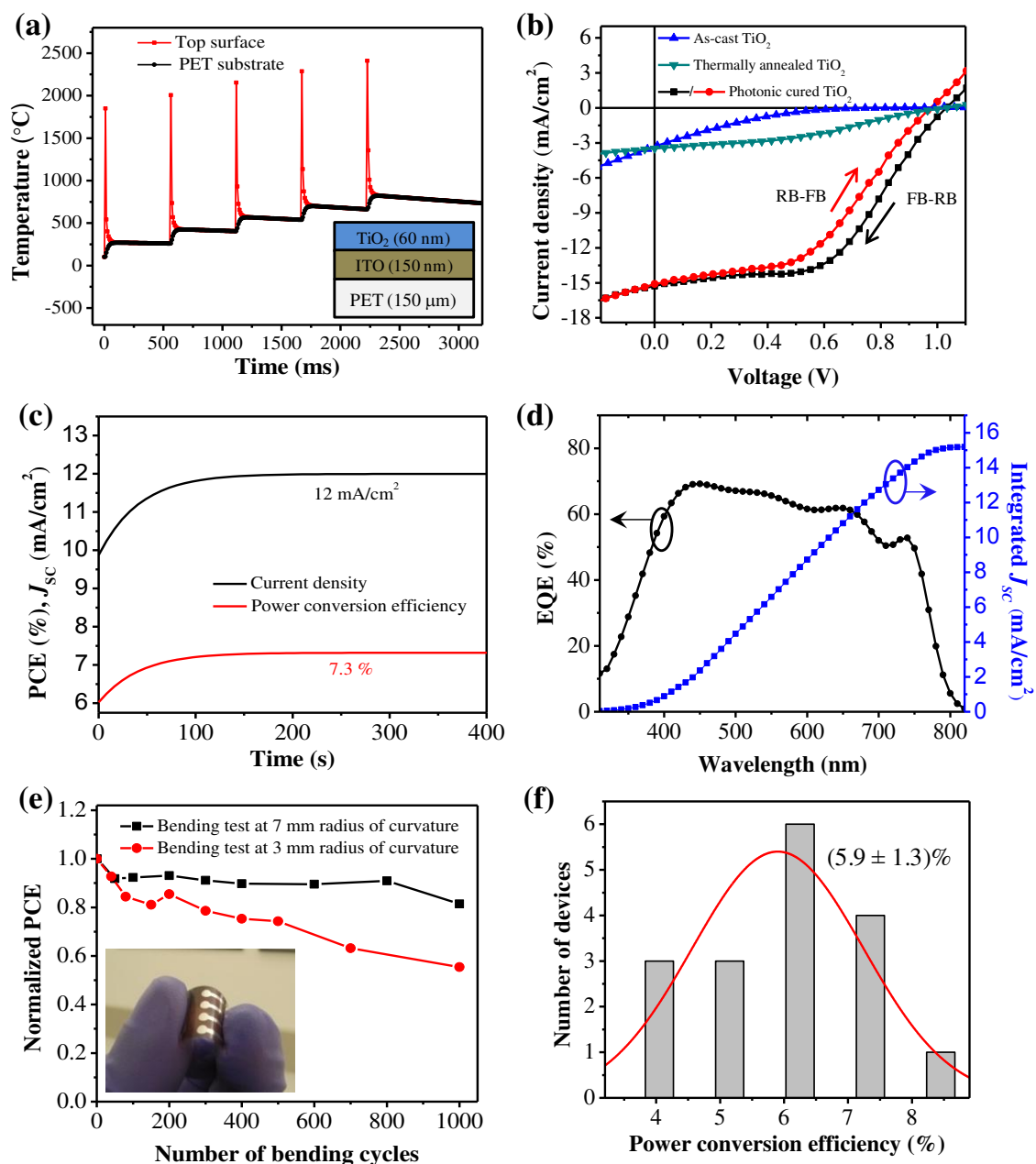
Figure 5.8. (a) Simulated temperature-versus-time profile for the photonic curing procedure used to anneal TiO$_2$ thin films on ITO/PET substrates. (b) Comparison of flexible device performances with as-deposited, thermally-annealed, and photonic-cured TiO$_2$ films. (c) Current density and PCE as a function of time for the same device held at 0.61 V forward bias. (d) EQE and integrated J_{SC} for the flexible device with photonic-cured TiO$_2$. (e) Normalized PCE of flexible devices after bending tests performed at 7 mm and 3 mm radii of curvature. Inset of (e) shows a photograph of the flexible devices. (f) Histogram of PCEs based on 17 flexible devices.

As can be seen, the device with as-coated TiO_2 film shows very poor photovoltaic performance: J_{SC} = 3.2 mA/cm^2, V_{OC} = 0.78 V, FF = 15.1% and PCE = 0.4%. This poor performance, particularly very low J_{SC} and FF, is due to the high interfacial resistance in the device due to poor conductivity of TiO_2 films. Device, using thermally annealed TiO_2, shows a J_{SC} = 3.5 mA/cm^2, V_{OC} = 1.04 V, and FF = 48.7%, and PCE = 1.8%, a five-time improvement. On the other hand, the device with photonic-cured-TiO_2 exhibits excellent performance with a J_{SC} = 15.3 mA/cm^2, V_{OC} = 1.03 V, FF = 51.4%, and PCE of 8.1%, measured at FB-RB scanning direction under AM 1.5G illumination in a nitrogen-filled glovebox. At RB-FB scanning direction, however, the device shows a J_{SC} = 15.1 mA/cm^2, V_{OC} = 0.98 V, FF = 46.9 %, and an overall PCE of only 6.9%, showing pronounced hysteresis, probably due to the use of planar device architecture [82,148]. The stabilized current density and power output from the same device at maximum power point (~ 0.61 V) are 12 mA/cm^2 and 7.3%, respectively (Figure 5.8c), which gives a reasonably accurate estimate of the device performance. The integrated J_{SC} from the EQE spectrum (Figure 5.8d) from the same device is 15.1 mA/cm^2, which is consistent well with the measured J_{SC} from *J-V* characteristics.

To demonstrate the mechanical flexibility, a stringent bending test was performed on four flat flexible devices at 7 mm and 3 mm radii of curvature (Figure 5.8e). The devices retain 60-90% of their initial PCEs after 1000 bending cycles, demonstrating the compatibility of perovskite solar cells with low-cost and light-weight flexible substrates. The small degradation in device performance results from decrease in J_{SC} and FF (**Figure 5.9**) due to cracking of ITO at higher stress (**Figure 5.10**) and increased contact resistance. Overall, flexible devices exhibit an excellent average PCE of 5.9% (Figure 5.8f). Though the average J_{SC} and FF of devices on PET

substrates (**Table 5.3**) are lower than those on glass substrates, due to lower conductivity of the photonic-cured TiO_2 as compared to the thermally-annealed TiO_2 on glass, the reasonably high PCEs of flexible devices fabricated using the combination of USC process and the photonic curing technique represent a substantial step towards the mass production of perovskite solar cells in near future.
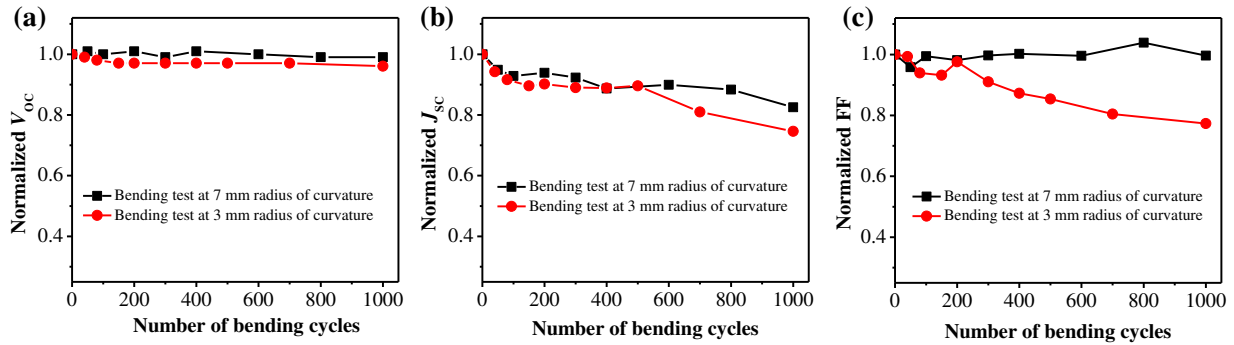
Figure 5.9. Effect of mechanical stress on a) V_{OC}, b) J_{SC}, and c) FF.
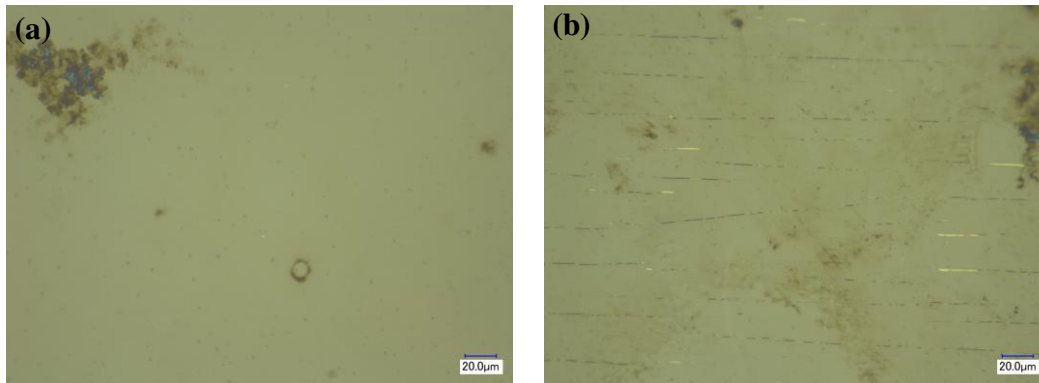
Figure 5.10. Optical microscope images of ITO morphology on PET substrates a) before any bending and b) after 300 bending cycles using a metal cylinder with 3 mm radius.

70

Table 5.3. Summary of device parameters, i.e., J_{SC}, V_{OC}, FF, and PCE of the PSCs fabricated using different deposition techniques and substrates with optimized processing conditions.

Deposition Technique	Substrate Type	J_{SC} [mA/cm^2]	V_{OC} [V]	FF [%]	PCE$^*_{avg}$ [%]	PCE$_{max}$ [%]
Spray Coating	Glass	17.37	0.99	61.41	10.56 ± 1.06	13.04
	PET	13.09	1.01	43.43	5.74 ± 1.60	8.02
Spin-coating	Glass	18.41	0.95	62.72	10.97 ± 0.82	12.96
	PET	16.67	1.02	45.52	7.74 ± 1.04	8.91

*The average device performances are based on 60 devices each in case of glass substrates, and 17 and 10 devices each in case of spray-coated and spin-coated flexible substrates, respectively.
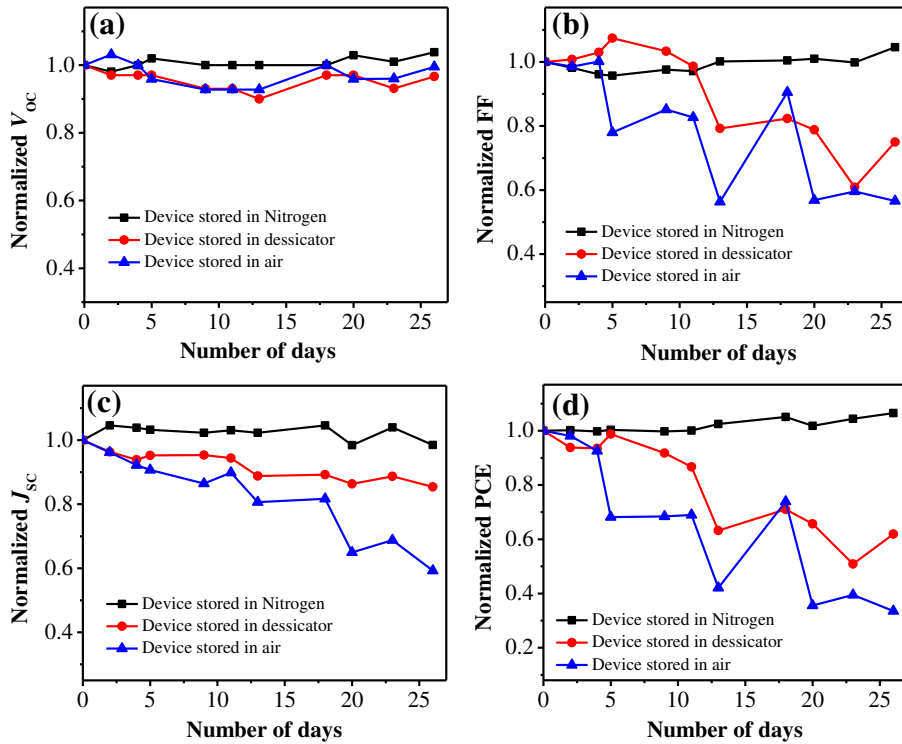
Figure 5.11. Stability measurements on spray-coated perovskite devices while the devices are stored in three different environments over about a month time.

Finally, the stability of spray-coated PSCs was measured as shown in **Figure 5.11**. To better

evaluate, glass substrate based devices were used for measurements. As seen, the devices stored

in inert ambient did not degrade, rather the PCE has increased about 10% of the initial value over time, which is due to the increase in FF. On the other hand, the devices stored in desiccator retained ~60% of their initial PCEs, while the air-stored devices retained 35% of their initial PCEs after 26 days. The fact that air-stored devices still functioned even after a month of time is quite encouraging. It is possible that advanced encapsulation technique can lead to more stable perovskite solar cells for outdoor applications.

5.4 Conclusion

In summary, a high throughput ultrasonic spray-coating process was successfully applied to fabricate high-quality, uniform, and highly crystalline $CH_3NH_3PbI_{3-x}Cl_x$ films on glass substrates for solar cell applications. The best solar cell fabricated on glass exhibited an efficiency of 13%, comparable to that of $CH_3NH_3PbI_{3-x}Cl_x$ device made by spin-coating. The spray-coating process flow has also been successfully translated from glass substrates to plastic PET substrates. Together with a low temperature photonic-cured compact TiO_2 layer, the best flexible $CH_3NH_3PbI_{3-x}Cl_x$ solar cell, fabricated by spray-coating, exhibited PCE as high as 8.1%. The excellent mechanical flexibility of these devices was demonstrated by the minimal degradation in performance after more than 500 bending cycles. The scalability of spray-coating process together with a low thermal budget photonic curing technique used in this work for the development of high-performance flexible perovskite solar cells represent a very unique and viable route for the roll-to-roll manufacturing of new generation solar cells.

Chapter 6: Photonic-Cured Compact TiO$_2$ Layer for Perovskite Solar Cells

In Chapter 5, a low thermal budget photonic curing technique was demonstrated to achieve crystalline TiO$_2$ layer on top of flexible, ITO-coated PET substrates. Here, this technique was optimized to sinter TiO$_2$ compact layers on both glass and PET substrates.

6.1 Motivation and Research Goal

To date, most of the high-efficiency PSCs, especially those with use *n-i-p* architecture, use a compact TiO$_2$ as the electron transport layer (ETL), which requires a high-temperature (~ 500 °C) sintering step and a long (~1-2 h) overall processing time [152-154]. Moreover, due to high temperature, it is incompatible with low-temperature polymer substrates. In contrast, the photonic curing technique can sinter thin films on a variety of substrates, especially on flexible, low-temperature substrates such as PET, polyethylene naphthalate (PEN), etc., within an extremely short period of time (milliseconds to seconds), thus significantly reducing the overall processing time. In this part of the research, the viability of photonic curing technique is evaluated in achieving high-quality sol-gel processed TiO$_2$ films on both ITO-coated glass and PET substrates. In addition, effect of moisture on the perovskite film growth and associated device performance was investigated. PSCs fabricated with optimized growth conditions on photonic-cured TiO$_2$ layers exhibited PCEs as high as 15.0% and 11.2% on glass and flexible PET substrates, respectively, which represents a performance level similar to those reported so far.

6.2 Experimental Section

6.2.1 Device Fabrication

All solution and materials were prepared as described in Chapter 5. For device fabrication, the TiO$_2$ solution was first dispensed onto ITO-coated glass and PET substrates, and spin-coated at 2000 rpm for 40 s. The TiO$_2$ films were then soft-baked at 80 °C for 10 min to drive off the residual solvent before they were either furnace annealed at 500 °C for 30 min or photonic-cured using a PulseForge 3300 processing system from NovaCentrix. For the glass substrates, the TiO$_2$ films were exposed to 25 pulses under a radiant exposure with a voltage of 200 V, pulse frequency of 2 Hz, and pulse duration of 7 ms from a plasma arc lamp. For PET substrates, the films were exposed to 10 pulses of 2 ms dwell time at a voltage of 200 V and pulse frequency of 2 Hz. Subsequently, the heated (70 °C) perovskite solution was spin-coated onto TiO$_2$/ITO-coated glass and PET substrates at 2000 rpm for 50 s in N$_2$-filled glove box, and immediately annealed at 100 °C for 70 min in air. The Spiro-OMeTAD solution was spin-coated at 2000 rpm for 30 s on top of CH$_3$NH$_3$PbI$_{3-x}$Cl$_x$ films, and the coated films were stored in a desiccator for 12 h for oxygen doping. Finally, 100 nm-Ag was thermally deposited at 1 Å/s using a shadow mask to complete the devices with area of 7.5 mm^2 each.

6.2.2 Film and Device Characterization

Current-voltage ($J-V$) curves of the fabricated devices were recorded by scanning from forward bias to reverse bias (1.2 V to -0.2 V) direction and vice versa. The voltage step during the scan was fixed at 35 mV with a delay time of 50 ms. EQE, AFM, SEM, XRD, and UV-Vis absorption measurements were done as described in previous chapters.

6.3 Results and Discussion

The photonic curing technique used in this work is illustrated in Figure 5.7, where a plasma arc lamp, capable of producing extremely high power densities up to 20,000 W/cm^2, is used to produce a broad radiant spectrum with wavelength ranging from 200 nm to 1400 nm. TiO$_2$ films on glass or PET substrates are exposed to 10-50 high-intensity pulses of high-density plasma arc in argon for a very short dwell time (~ 5-10 ms). For device fabrication, an *n-i-p* architecture, ITO/TiO$_2$ (60 nm)/CH$_3$NH$_3$PbI$_{3-x}$Cl$_x$ (300 nm)/Spiro-OMeTAD (200 nm)/Ag was incorporated.
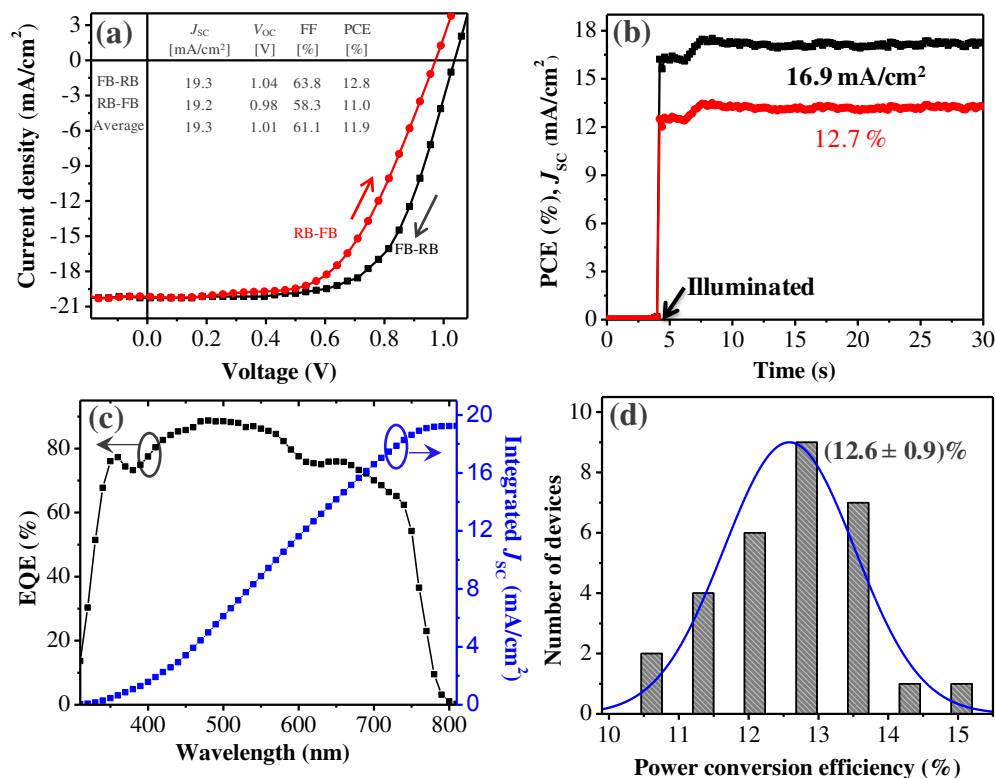
Figure 6.1. (a) *J−V* curve of a typical device scanned at different directions under AM 1.5G illumination. (b) Stabilized power output of the corresponding device at near maximum power point (0.77 V). (c) EQE spectrum and integrated J_{SC} from the corresponding device. (d) Histogram of PCEs measured for 30 devices, fabricated with photonic-cured TiO$_2$ layer.

Figure 6.1a shows the typical $J–V$ characteristics of a PSC with photonic-cured TiO_2 on ITO glass substrate, showing a J_{SC} of 19.3 mA/cm^2, a V_{OC} of 1.04 V, a FF of 63.8%, and an overall PCE of 12.8% at FB-RB scanning direction and a J_{SC} of 19.2 mA/cm^2, V_{OC} of 0.98 V, FF of 58.3%, and PCE of 11.0% at RB-FB direction, under AM 1.5G illumination measured in a nitrogen-filled glovebox. The presence of $J–V$ hysteresis may stem from the use of a planar device architecture or ferroelectric property of the perovskite material [82,155,156]. To better evaluate the performance, the stabilized current density and power output at maximum power point (~0.75 V) of the same device were determined, showing a PCE of 12.7% (Figure 6.1b). The integrated J_{SC} of 19.2 mA/cm^2 from EQE spectrum (Figure 6.1c) of the same device is consistent with the value extracted from the $J–V$ curve. In order to demonstrate the performance reproducibility, a series of PSCs were fabricated with photonic-cured TiO_2 layer, exhibiting an excellent average PCE of 12.6 ± 0.9% (Figure 6.1d and **Table 6.1**).

Table 6.1. Comparison of device performances based on devices with photonic cured and furnace annealed compact TiO_2 layers.

TiO_2	J_{SC} [mA/cm^2]	V_{OC} [V]	FF [%]	PCE$^*_{avg}$ [%]	PCE$_{max}$ [%]
Photonic cured	19.9 ± 0.8	1.04 ± 0.02	60.9 ± 3.5	12.6 ± 0.9	15.0
Furnace-annealed	19.4 ± 0.5	1.04 ± 0.02	65.7 ± 2.7	13.3 ± 0.7	15.1

*Average PCEs are calculated from 30 devices in each case.

For comparison, **Figure 6.2**a shows the $J–V$ curves of a typical device fabricated using furnace annealed (500 °C) TiO_2 layer, exhibiting a J_{SC} of 20.3 mA/cm^2, V_{OC} of 1.03 V, FF of 65.2%, and PCE of 13.6% at FB-RB scan direction, and a J_{SC} of 20.2 mA/cm^2, V_{OC} of 0.97 V, FF of 64.5%, and PCE of 12.6% at RB-FB direction, with an average PCE of 13.1%. The PCE

histogram based on 30 devices with furnace-annealed TiO$_2$ compact layers shows an average PCE of 13.3 ± 0.7% (Figure 6.2b).
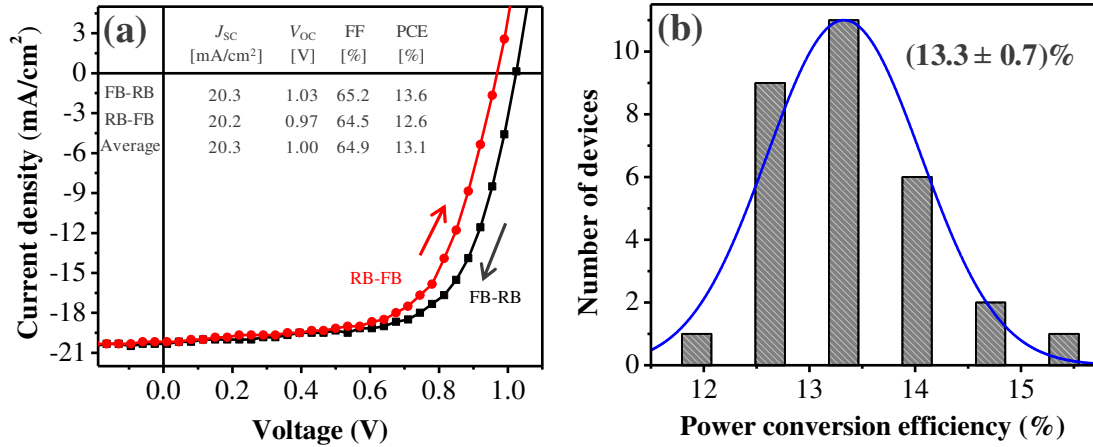
Figure 6.2. *J–V* curve of a typical device with furnace-annealed TiO$_2$ layer scanned at different directions under standard illumination (100 mW/cm^2). (b) Histogram of PCEs measured for 30 devices, fabricated with furnace annealed (500 °C) compact TiO$_2$ as electron transport layer.
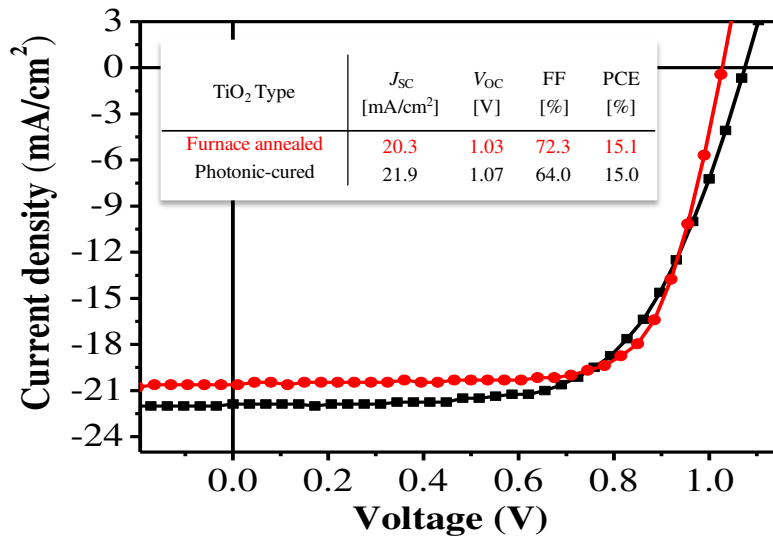
Figure 6.3. *J-V* curves of the champion PSCs with furnace-annealed and photonic-cured TiO$_2$ layers.

In addition, the champion devices with photonic-cured and furnace annealed TiO_2 layers show 15.0 and 15.1% PCEs, respectively (**Figure 6.3**). As can be seen, the devices with photonic-cured TiO_2 show an excellent and comparable performances to those with furnace annealed TiO_2 layers, demonstrating the potential of photonic curing technique to replace high-temperature furnace annealing.
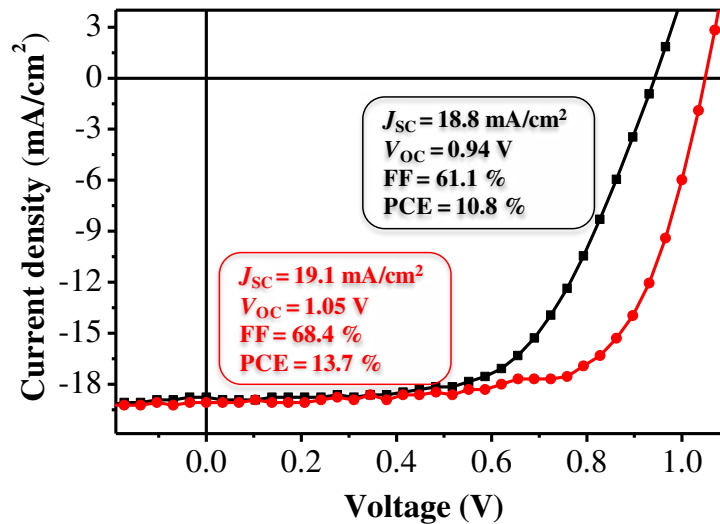
Figure 6.4. Comparison of performances of devices with perovskite film annealed in N2 (black) and air (red).

At this point, it is worth noting that during this study, we took into consideration the effect of humidity as it plays an important role during film growth. The device performance based on perovskite films that are annealed air are superior to those counterparts based on perovskite films annealed in controlled environment, for example, N_2 (**Figure 6.4**). This is due to the fact that N_2-annealed perovskite films have relatively high density of pinholes compared to air-annealed (relative humidity of ~35%) films (**Figure 6.5**). Such pinholes lead to reduction in the volume of

absorber material, thus effectively resulting in relatively less number of photogenerated charges for the N_2-annealed film [157]. Another significant observation is that air-annealed films result in higher V_{OC}, which is most likely associated with the reduced nonradiative recombination [157]. These observations are consistent with previous reports on the effect of moisture on perovskite film growth and device performance [70,158].
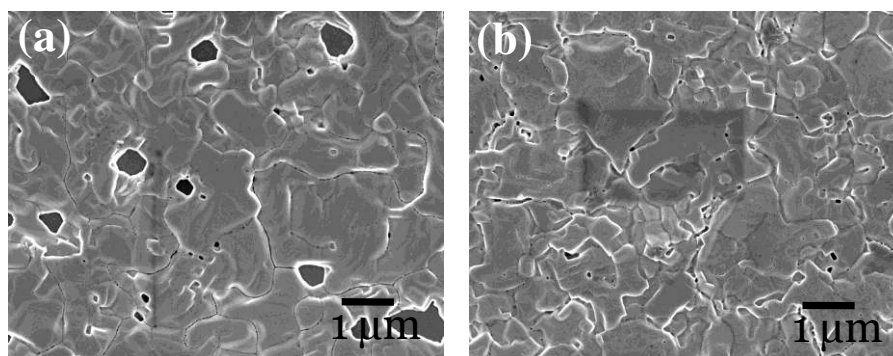
Figure 6.5. SEM image of perovskite film on ITO/TiO$_2$ substrates after annealing for 70 minutes in (a) N$_2$ and (b) air.

In order to understand how photonic curing changes electrical and optical properties of the TiO$_2$ films, the crystallinity and morphology of the films were characterized by XRD and AFM. **Figure 6.5**a shows the XRD spectra obtained on as-cast, photonic-cured, and furnace-annealed TiO$_2$ films. While the as-cast film does not show any characteristic anatase peak reflection at ~25.3°, formation of the desired anatase phase is evident for both the furnace-annealed and photonic-cured films. Figure 6.5b shows the absorption spectra for the same as-cast, photonic-cured, and furnace-annealed ITO/TiO$_2$ films, and the optical bandgaps using Tauc plot are estimated to be 3.82 eV, 3.43 eV, and 3.46 eV, respectively. To provide further insight, as well as to obtain quantitative information about the roughness features, **Figure 6.6** shows how the

TiO$_2$ film morphology changes with various annealing treatments. While the as-cast film shows a smooth and uniform surface morphology with very small crystal sizes, both furnace-annealed and photonic-cured films demonstrated large grains and relatively rougher surface morphologies, indicating an increase in crystallinity and thus conductivity. The average root-mean-square roughness (r_{RMS}) for the as-cast film was 0.24 nm, which gradually increased to 1.1 nm and 0.58 nm for the photonic-cured and furnace-annealed counterparts, respectively.
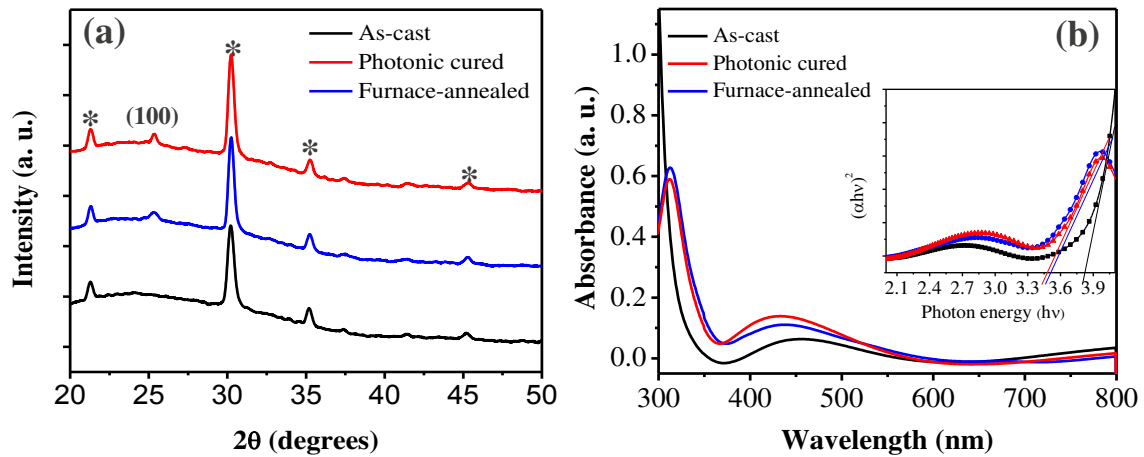
Figure 6.6. (a) XRD spectra for as-cast, photonic-cured, and furnace annealed TiO$_2$ films, where * denotes ITO peaks; (b) Absorption spectra of the corresponding films.
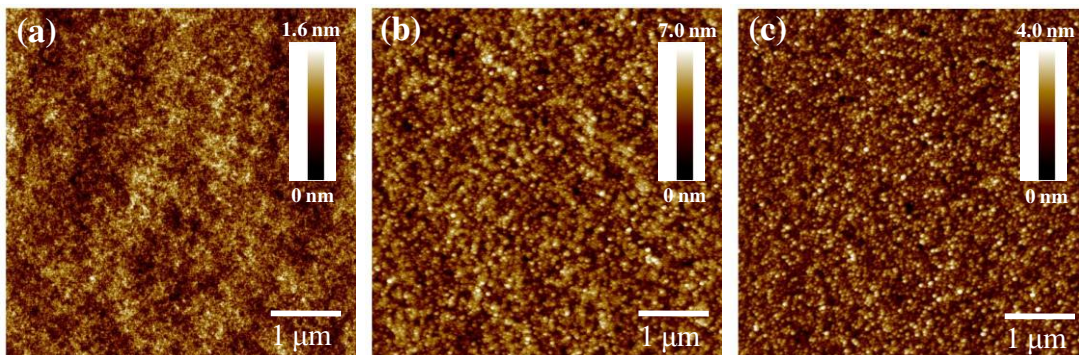
Figure 6.7. AFM images of (a) as-cast, (b) photonic-cured, and (c) furnace annealed TiO$_2$ films.
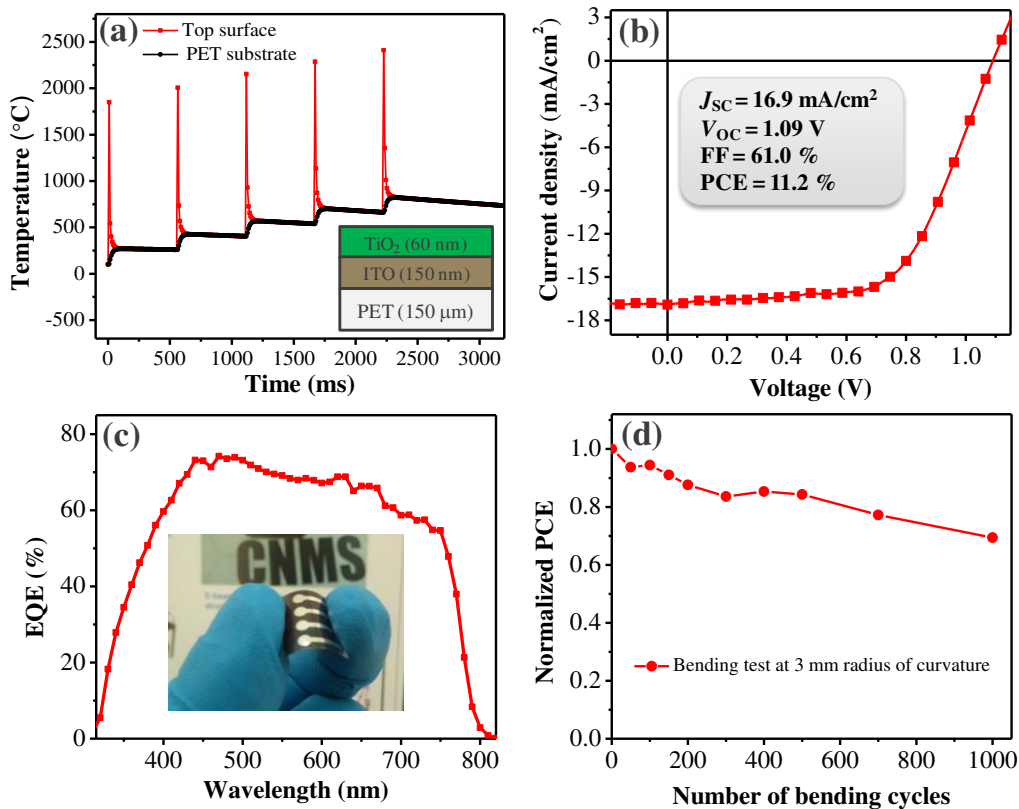
Figure 6.8. (a) Simulated temperature-vs-time profile for the photonic curing procedure used to sinter TiO$_2$ layer on PET substrate. (b) *J−V* curve of a typical device scanned at different directions. (c) EQE spectrum of the corresponding device. Inset to (c) is a photographic image of the flexible devices. (d) Normalized PCE of flexible devices after bending tests performed using a radius of curvature of 3 mm.

After achieving excellent performance from devices on glass substrates, a series of flexible devices were fabricated using photonic-cured TiO$_2$ and optimized perovskite layers. The theoretical temperature vs. time profile of the photonic curing condition used for PET substrates is illustrated in **Figure 6.8**a. Clearly, the TiO$_2$ film can reach temperature levels that are much higher than the PET substrates can sustain. Due to very short pulse dwell time (~2 ms), however, underneath PET substrate remain unaffected. Figure 6.8b shows the *J−V* characteristics of the champion flexible device with a *J*$_{SC}$ of 16.9 mA/cm^2, *V*$_{OC}$ of 1.09 V, FF of 61.0%, and an overall

PCE of 11.2%. Based on the measurements of 10 devices, the average PCE obtained from flexible PSCs is 9.4 ± 0.9%. The measured EQE spectrum of the same device is shown in Figure 6.8c, yielding a J_{SC} value of 16.2 mA/cm^2, reasonable consistent with J_{SC} value obtained from the $J-V$ curve.

In order to investigate the mechanical flexibility of the flexible devices, a stringent and repetitive bending test was carried out on flat devices using a metal cylinder with 3 mm radius of curvature. Devices retain about ~70% of their initial PCEs after 1000 bending cycles, demonstrating their robustness under stress (Figure 6.8d). The small degradation may result from cracking of ITO after repetitive bending (Figure 5.10).

6.4 Conclusion

In summary, a roll-to-roll compatible photonic curing technique was successfully demonstrated and applied as a promising replacement of conventional furnace annealing to achieve high-quality, compact TiO$_2$ films on both glass and flexible substrates, significantly reducing the processing time and thermal budget. Devices fabricated on photonic-cured TiO$_2$ demonstrated excellent photovoltaic device performance, which was comparable to that observed on furnace-annealed TiO$_2$ layers. More importantly, flexible devices exhibited a high reaching to 11.2%, that is on par with most of the reported values on state-of-the-art devices.

Chapter 7: Fabrication of Organic Field-Effect Transistors by Ultrasonic Spray-Coating

This chapter evaluates the USC process in fabricating organic field-effect transistors (OFETs), where both the dielectric and active layers were sequentially spray-coated. A cross-linkable insulator poly-4-vinylphenol (PVP) was incorporated as the dielectric layer, and a soluble small molecule 6,13-bis(trisopropyl-silylethynyl) pentacene (TIPS-PEN) was used as the semiconductor or active layer.

7.1 Motivation and Research Goal

Recent progress in the design and synthesis of organic semiconductor materials have enabled OFETs to achieve high charge carrier mobilities comparable to or exceeding that of a-Si [159-161]. As a result, they have been successfully integrated to enable a wide range of applications including display backplanes, electronic papers, sensors, memories, and radio-frequency (RF) identification tags [162-164]. However, the lack of low-cost and large-scale OFET manufacturing methods remains a major obstacle to their successful commercialization. To this end, solution processing of organic semiconductors for OFETs is attracting tremendous interest because it is suitable for large area processing, is compatible with flexible substrates, and has the potential to take advantage of existing low-cost, high-throughput, roll-to-roll manufacturing technology. Spin-coating and drop-casting are two widely employed solution processing techniques that are simple and effective for producing devices with excellent performance in the research laboratory environment [165,166]. However, these techniques are inherently inefficient, wasting high fractions of solution, and are not readily scalable to industrial scale, large area processing. Intense efforts have been directed toward the development of alternative solution-

based methods such as ink-jet printing, screen printing, doctor blading, and spray coating that can meet the manufacturing requirements for cost-effective, large area processing [167-169].

Due to the key advantages described in Chapter 5, this USC process was demonstrated in this work to fabricate OFETs. Although the USC process has been demonstrated as an alternative method to fabricate organic electronic devices including OLEDs [138,170], OPVs [132,139,140], and organic photodetectors (OPDs) [141], very little work concerning OFET fabrication by this process has been reported [171]. Previous work has mostly focused on the spray coating of soluble conjugated polymers such as poly(3-hexylthiophene) (P3HT) [140,171]. Compared to polymers, however, soluble small molecules are easier to synthesis and purify, and exhibit better charge carrier mobility and chemical stability [172].

A typical, soluble small molecule organic semiconductor that is widely used in organic electronics because of its high mobility and good air stability is 6,13-bis(trisopropyl-silylethynyl) pentacene (TIPS-PEN) [173]. So far, high mobility TIPS-PEN based OFETs have been fabricated by a variety of solution-based methods including spin-coating and drop-casting. TIPS-PEN OFETs prepared by drop-casting have exhibited high mobilities of 0.65 cm^2/Vs while those prepared by spin-coating usually show relatively lower mobilities, ranging between 0.05 to 0.20 cm^2/Vs [174]. Ink-jet printing of TIPS-PEN OFETs with mobilities of 0.12 cm^2/Vs have also been reported [175]. There has so far been no report of TIPS-PEN OFETs prepared by the USC, a process that is compatible for the fabrication of large area, cost-effective OFETs.

In this work [142], a fabrication method for high-performance OFETs was developed based on ultrasonic spray-coated TIPS-PEN active layers, as well as spray-coated poly-4-vinylphenol (PVP) dielectric layers on various substrates. Highly crystalline, aligned TIPS-PEN films were

obtained on SiO_2/n^{++} Si substrates by optimizing ultrasonic spray parameters such as flow-rate, nozzle height and moving speed, resulting in a maximum mobility as high as 0.36 cm^2/Vs and an on/off current ratio over 10^5. Moreover, flexible OFETs were fabricated by sequential spray deposition of a dielectric layer of PVP and an active layer of TIPS-PEN on PET substrates. The flexible TIPS-PEN OFETs exhibit a best mobility up to 0.35 cm^2/Vs and an on/off ratio over 10^4, together with negligible hysteresis in current-voltage characteristics. Ultrasonic spray-coating of OFETs thus provides device performance comparable or superior to similar devices prepared by other solution processing methods.

7.2 Experimental Section

7.2.1 Material, Solution and Film Preparation

The poly(4-vinylphenol) (PVP, M_w = 20 kDa) and a cross-linking agent poly(melamine-co-formaldehyde) (M_w = 432) were purchased from Sigma Aldrich. A 1.5 wt% PVP solution was first prepared with propylene glycol monomethyl ether acetate (PGMEA) as the solvent. Then, the poly(melamine-co-formaldehyde) was added to the solution at a weight ratio of 1:3 to PVP. The blend solution was stirred using a magnetic spin bar at room temperature for 24 h. TIPS-PEN was used as purchased from Sigma Aldrich without further purification. TIPS-PEN was dissolved in toluene at a concentration of 8 mg/ml. In all our experiments the atomizing gas pressure for the spray process was kept at 0.4 psi in order to achieve a reasonable spray rate. Spray-coated films are optimized by varying the solution flow rate, nozzle movement speed, spray nozzle height and substrate temperature. The optimized processing conditions for TIPS-PEN film in this work are: flow rate of 1.2 ml/min, nozzle-to-substrate height of 4.6 cm, and nozzle moving speed of 8 mm/s.

7.2.2 Device Fabrication and Testing

A bottom-gate, top-contact (BG/TC) configuration, as shown in **Figure 7.1**a, was adopted in OFET fabrication. Prior to the spray-deposition of organic thin films, heavily doped n-type silicon substrates with 300 nm thermally grown silicon dioxide (capacitance, $C_i = 12.5$ nF/cm^2), and ITO-coated PET substrates were cleaned with a sequence of detergent, DI water, acetone and IPA in an ultrasonic bath. The PVP solution was spray-coated on the pre-cleaned ITO-coated PET flexible substrates in air. Then, the spray-coated PVP films were cross-linked at 180 °C for 1 h. After the crosslinking of the PVP dielectric layer, the TIPS-PEN was subsequently spray-coated on the top of PVP film in air ambient. For devices using the Si substrate, TIPS-PEN was directly spray-coated onto the SiO$_2$ surface. During spray-coating, the substrates were tilted at a small angle (3°) to align the orientation of TIPS-PEN crystals while the solution is sprayed. Finally, 50 nm thick Au were deposited by thermal evaporation through a shadow mask for source and drain electrodes. Channel lengths of the devices were 25, 50, 75 and 100 μm, while the width was fixed at 2000 μm. In order to compare the OFET devices fabricated with spray process, spin-coated and drop-casted OTFTs were fabricated. For spin-coated and drop-cast OFETs, the same 8 mg/ml TIPS-PEN solution in toluene was spin-coated at 500 rpm for 60 s, or drop-cast onto the SiO$_2$/Si substrates.

Electrical measurements of OFETs were carried out in ambient environment with a Keithley 4200 semiconductor analyzer attached to a probe station. By exploiting the slope of transfer curve ($I_{DS}^{1/2}$-V_{GS}), the field-effect mobility in saturation regime was calculated from the equation $I_{DS} = \mu W C_i (V_{GS}-V_T)^2/2L$, where W and L are channel width and length, C_i is the capacitance per unit area, μ is the field-effect mobility, and V_{GS}, V_T are gate voltage and threshold voltage,

respectively. The capacitance of dielectric layer was measured with an Agilent E4980A precision LCR meter.

7.2.3 Thin Film Characterization

Optical micrographs of thin films were collected using a Nikon OptiPhot2-POL optical microscope with cross-polarizers. Thin film crystallinity was characterized using Philips X'Pert X-ray diffraction. 2D GIXD data were collected as a 2D image map using an image plate that was divided into a component in the plane of the substrate and a component perpendicular to the substrate in an Anton Paar SAXSess mc2 spectrometer (high-resolution grazing incidence scattering with a point x-ray beam). Morphology and roughness of spray-coated films were investigated using a Bruker Dimension Icon AFM operated in tapping mode.

7.3 Results and discussion

Figure 7.1a schematically illustrates the USC process and the structure of fabricated BG/TC OFET devices. Figure 7.1b shows a polarized optical microscopy image of the top view of spray-coated TIPS-PEN film from a 0.8 wt% toluene solution. As the solvent evaporates, long, ribbon-shaped TIPS-PEN polycrystals containing some single-crystalline domains were observed to grow as indicated by their color variation under polarized light. The typical TIPS-PEN crystals observed in the spray-coated films were several hundred micrometers long and tens of micrometers wide. In general, the charge transport in polycrystalline TIPS-PEN films is quite different in two types of regions: the high-mobility large crystalline grains and the low-mobility polycrystalline regions with many grain boundaries. The large-grained, ribbon-shaped TIPS-PEN polycrystals appear to be responsible for the higher field-effect mobilities because the charge carriers encounter fewer grain boundaries in these regions. Figure 7.1c shows an AFM image of

a spray-coated TIPS-PEN film. The well-developed terrace-like multilayered structure indicates

the formation of a highly crystalline film. The mean step height per terrace measured by the

cross-sectional AFM profile in Figure 7.1d is around 1.65 nm, which is in agreement with the

vertical intermolecular spacing in TIPS-PEN single crystals [173,176]. This result suggests that

the TIPS-PEN in the spray-coated film is oriented in a (001) orientation with the pentacene

backbone packed in a face-to-face orientation.
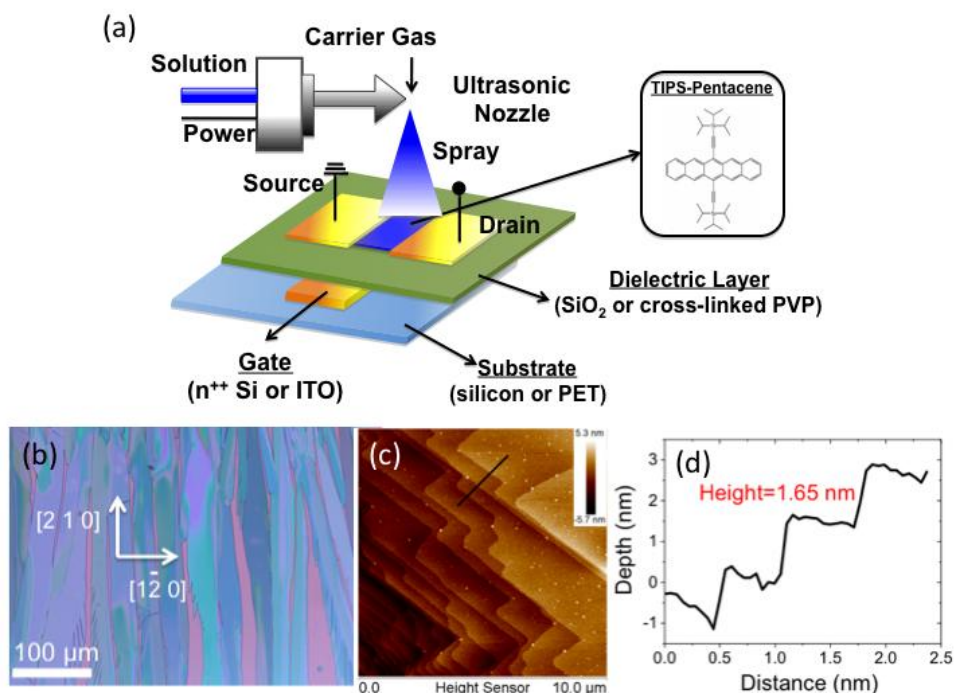
Figure 7.1. (a) Schematic diagram of the USC process and the BG/TC OFET device architecture. The chemical structure of TIPS-PEN is shown in the inset. In the Si substrate case, the n[++] doped Si substrate serves as the unpatterned gate. (b) Polarized optical microscopy image of a spray-coated TIPS-PEN film, (c) AFM image of a terraced structured spray-coated TIPS-PEN film, (d) Line profile taken along the black line segment in (c) crossing three single steps.

The molecular orientation and packing in the spray-coated TIPS-PEN films were further

confirmed by out-of-plane XRD and two-dimensional (2D) grazing-incident X-ray diffraction

(GIXD). **Figure 7.2**a shows the out-of-plane XRD patterns of a spray-coated TIPS-PEN film, consisting only of a series of (00*l*) reflection diffraction peaks, indicating a well-organized molecular crystal structure with a vertical intermolecular spacing of 1.68 nm. This result is consistent with the terrace step height of 16–17 Å measured from AFM images, which is identical to that of the c-axis unit cell [177]. Figure 7.2b shows an in-plane GIXD pattern of a spray-coated TIPS-PEN film on SiO_2, exhibiting many scattering spots along the Q_z and the $Q_{x,y}$ directions. The (01*l*) diffraction peaks, corresponding to the repeating period perpendicular to the direction of crystal growth, and (00*l*) diffraction peaks, corresponding to the repeating period parallel to the direction of crystal growth, were observed, indicating that the crystals are azimuthally oriented. These results demonstrated that well-ordered TIPS-PEN crystals in the lateral and vertical directions are formed in the USC process.
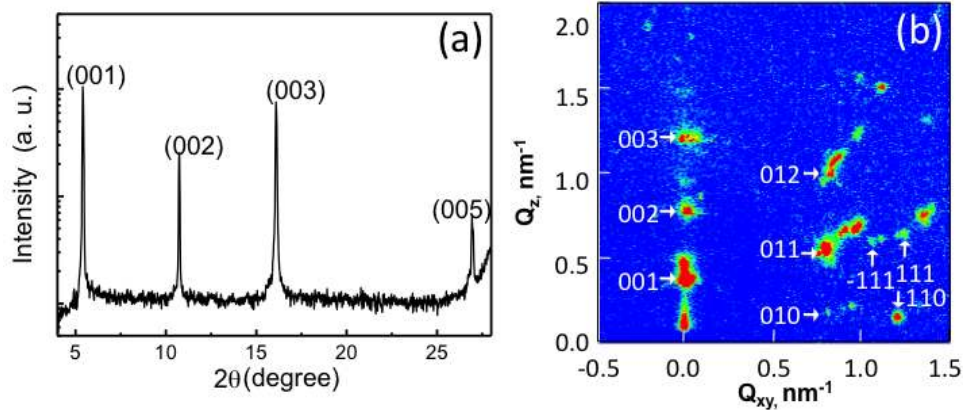
Figure 7.2. (a) Out-of-plane XRD pattern, and (b) 2D GIXD image of a spray-coated TIPS-PEN film on SiO_2. Indices are provided for the most intense Bragg rods.

Figure 7.3 shows the typical transfer and output curves of spray-coated OFETs on SiO_2/n^{++} Si substrates. The average mobility of 20 spray-coated devices is 0.15 ± 0.02 cm^2/Vs, with a maximum of 0.36 cm^2/Vs. The average threshold voltage (V_{Th}) is -0.9 ± 3.8 V and the on/off

current ratio is 1.3×10^5. Negligible current hysteresis was observed in the transfer characteristics, indicating a less number of charge trapping centers between the polycrystalline surface of TIPS-PEN and the gate dielectric layer. The variations in the values of the characteristic parameters of these devices are shown in Figure 7.3c. The mobility, V_{Th}, and on/off ratio fluctuated slightly, but overall, the electrical properties were found to be uniform. These results suggest that the USC technique can be used to fabricate a variety of printed electronic devices that exhibit a high degree of inter-device uniformity. The performance of the spray-coated devices is comparable to that of TIPS-PEN OFETs fabricated by drop-casting process and better than those of devices fabricated by spin-coating process, as shown in Table 7.1.

Table 7.1. Electrical properties of TIPS-PEN OFETs fabricated by different methods. The mobilities were calculated at the saturation region at the drain bias of -40 V.

| Substrate | Insulator | | Active layer | μ_{avg}^{*} | V_{Th} | On/off ratio |
	Materials	Processing	Processing	(cm^2/Vs)	(V)	
Si	SiO$_2$	Thermal oxide	Spin-coating	0.0005	-7.6	1×10^3
			Drop-casting	0.157	7.0	8×10^4
			Spray-coating	0.145	-0.9	1×10^5
	PVP	Spin-coating	Spray-coating	0.117	2.0	6×10^4
		Spray-coating	Spray-coating	0.108	3.6	2×10^4
PET	PVP	Spin-coating	Spray-coating	0.100	1.6	4×10^4
		Spray-coating	Spray-coating	0.122	11.3	1×10^4
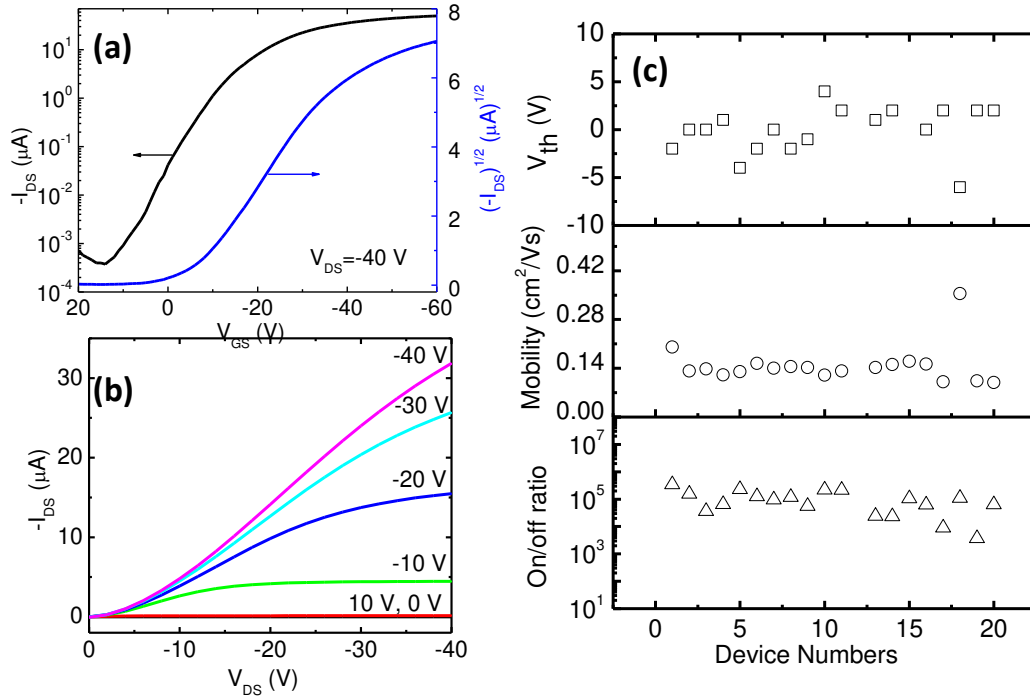
Figure 7.3. (a) Representative transfer (at drain bias of -40 V) and (b) output characteristics of a spray-coated TIPS-PEN OFET on SiO_2/Si substrate with a channel width of 2000 μm and channel length of 100 μm. (c) Variation of device performance parameters including mobility, V_{Th}, and on/off ratio for 20 devices.

The boiling point (bp) and vapor pressure of the solvent could change the drying behavior of droplets in a spray-coating process, and hence significantly affect the morphology and crystallinity of spray-coated TIPS-PEN film. Therefore, TIPS-PEN OFETs were fabricated using three solvents with different boiling points, toluene (bp = 111 °C), CB (bp = 131 °C) and DCB (bp = 180 °C) to investigate their suitability to the USC processing. The lower evaporation rate of these high boiling point solvents makes the coating process less sensitive and easier to control over a large parameter space. The device performances of spray-coated TIPS-PEN OFETs with these solvents are compared in **Figure 7.4**. The mobility is 0.05 cm^2/Vs for films spray-coated from a CB solution, 0.03 cm^2/Vs for DCB, and 0.16 cm^2/Vs for toluene. The results show that

91

the highest boiling point solvent does not necessarily provide the highest mobility, and suggest toluene with medium boiling point to be the most suitable solvent for the TIPS-PEN deposition by USC. This observation is consistent with previously reported results [178,179].

The performance of OFETs strongly depends on the morphology of TIPS-PEN polycrystal films. TIPS-PEN films with high crystallinity and large grain size exhibit the best mobility and on/off ratio. Particularly, in our USC process, balancing the solvent evaporation and diffusion-driven flows of solution droplets is critical to obtain highly ordered TIPS-PEN crystals. The moderate evaporation rate of toluene can improve the morphology uniformity and packing density of the TIPS-PEN molecules, and therefore resulted the best device performance [179].
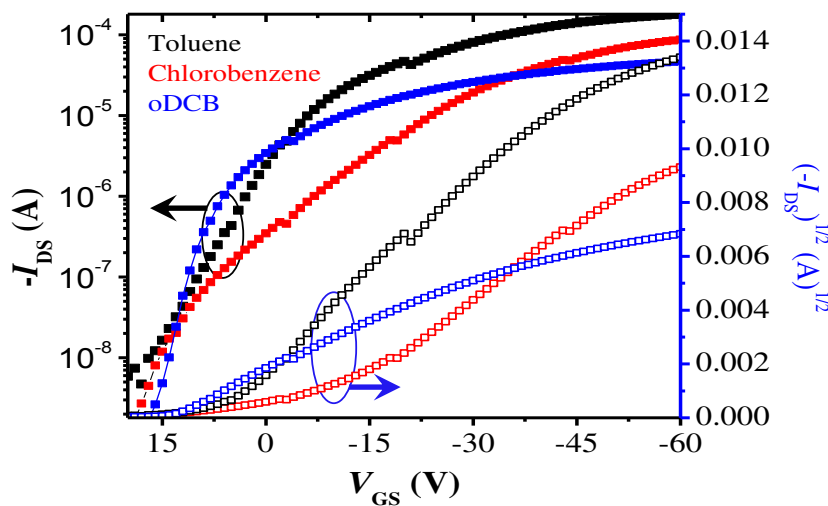
Figure 7.4. Current-voltage characteristics (I_{DS} versus V_{GS} measured in saturation regime at V_{DS} = -40 V) for ultrasonic spray-coated TIPS-PEN devices using toluene, chlorobenzene, and ortho-dichlorobenzene as casting solvents.

In addition, film formation in spray-coating is a complex process that is affected not only by the solvent boiling point but also by other factors such as the infuse rate and nozzle moving speed. **Figure 7.5** shows the relationship of device mobility with the infuse rate, nozzle-substrate

distance, or nozzle path speed while the other parameters were held constant. From this plot, the optimized processing conditions for spray-coated TIPS-PEN film in this work were determined to be an infuse rate of 1.2 ml/min, a nozzle-to-substrate distance of 4.6 cm, and a nozzle path speed of 8 mm/s.
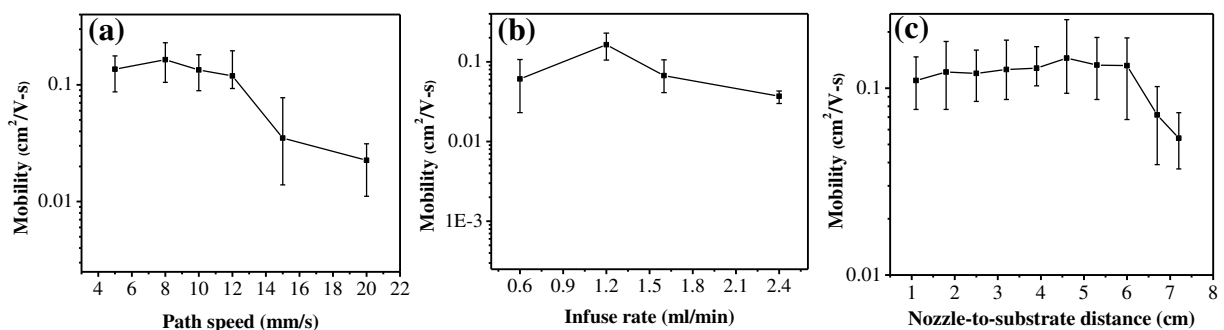
Figure 7.5. Variation in the field-effect mobilities of ultrasonic spray-coated TIPS-PEN OFETs on SiO$_2$/Si substrates (a) at different infuse rates while keeping the path speed (8 mm/s) and nozzle height (4.6 cm) fixed, (b) at different nozzle heights while keeping the infuse rate (1.2 ml/min) and path speed (8 mm/s) fixed. (c) at different path speeds while keeping the infuse rate (1.2 ml/min) and nozzle height (4.6 cm) fixed.
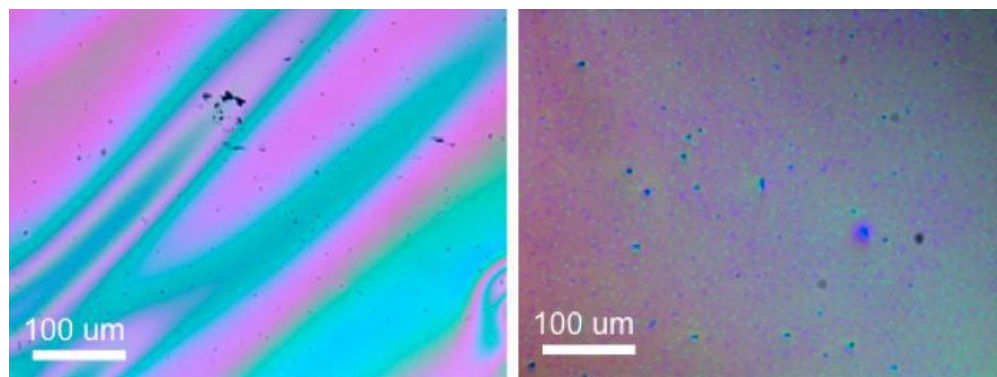
Figure 7.6. Optical images of a cross-linked PVP film on glass prepared by ultrasonic spray at (a) room temperature and (b) 50°C, demonstrating the higher uniformity of the spray-coated PVP film prepared at 50°C.

93

To demonstrate the versatility of ultrasonic spray technique, the deposition of a dielectric layer by USC was also explored to fabricate flexible OFETs. A wide range of insulators with different solvents have been used in various deposition techniques for OFETs [176,177]. In this work, a cross-linkable PVP [180] was selected to improve environmental stability and structural robustness and to enhance chemical stability to minimize potential solubility issues arising from subsequently deposited layers. In order to get a smooth film, a single-pass spray was used to deposit the PVP dielectric layer. During the spray process, the dispersed droplets merged into a single wet surface layer on the substrate before drying. As the solvent evaporates, a uniform PVP film was successfully coated with the additive poly(melamine-co-formaldehyde) in PGMEA on the substrate. Pre-heating the substrate up to 50 °C can facilitate the merging of droplets, speed up the drying process, and improve the homogeneity of the PVP film (**Figure 7.6**). The coating was followed by a heating cycle at 175 °C for an hour to induce crosslinking. At this temperature, crosslinker poly(melamine-co-formaldehyde) efficiently acts as a donor of a formaldehyde moiety by firstly reacting at the activated 3-position of the phenol ring in the PVP. Then, the cross-linking process is completed by reacting with another phenol ring to form a strong covalent-bonded bridge. Crosslinked PVP films are not dissolved in common organic solvents such as chloroform, toluene, or chlorobenzene, allowing for subsequent solution-based deposition of organic semiconductors.

Figure 7.7a shows an optical image of a spray-coated PVP film. A uniform PVP film was obtained over a large area. We also observed some bumps and craters on the film, induced by the impingement of sprayed droplets and convergence on droplet boundaries. Similar phenomenon was reported earlier in other spray-coated films [171]. The resultant spray-coated PVP insulator

layer at optimized spray conditions has a thickness of around 600 nm. The root-mean-square roughness of the local spray-printed PVP film is 0.46 nm (across a 5 μm×5 μm area), determined by AFM measurements (**Figure 7.8**), similar to the roughness of spin-coated films (~ 0.30 nm). The low roughness is mainly due to the small size of droplets atomized by ultrasonic waves.
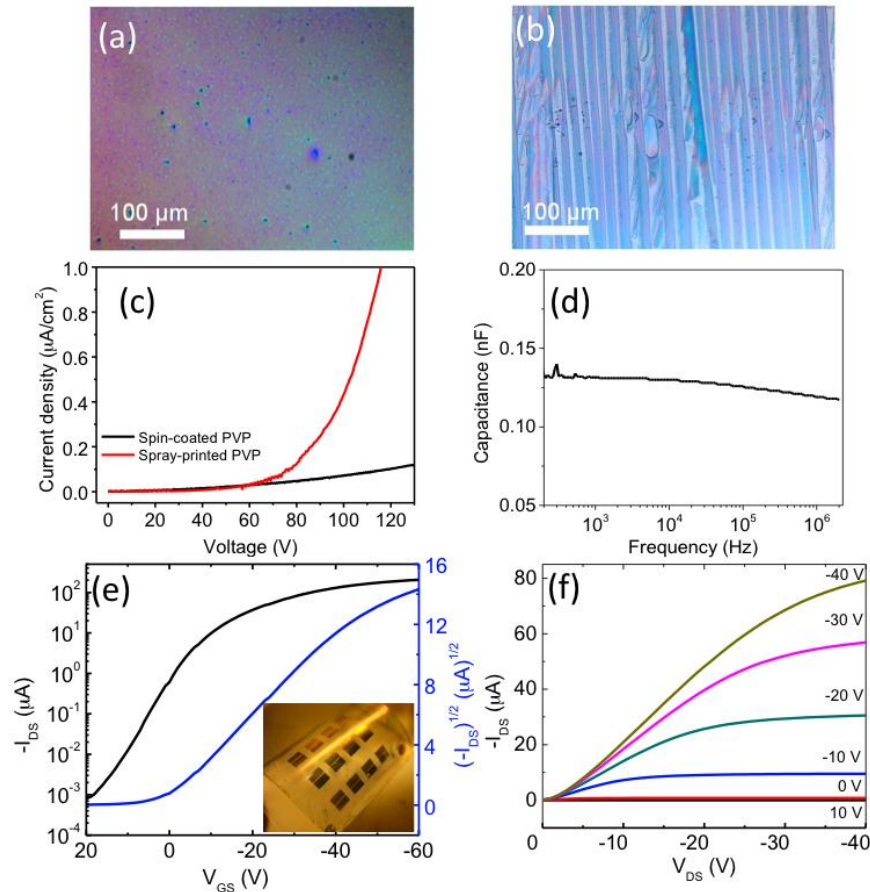
Figure 7.7. (a) Optical microscopy image of a spray-coated PVP film prepared at 50°C, (b) Optical microscopy image of a sequentially spray-coated TIPS-PEN film on a PVP layer, (c) Current leakage versus applied voltage curves of PVP films prepared by ultrasonic spray and spin-coating processes. The electrical measurements were performed using Si/PVP/Al structures fabricated on highly doped silicon substrates. (d) Frequency-dependent capacitance of the spray-coated PVP film measured up to 1MHz. (e) Transfer and (f) output characteristics of ultrasonic spray-coated TIPS-PEN based flexible OFETs with sequentially-deposited dielectric (PVP) and semiconductor (TIPS-PEN) layers, pictured in the inset of (e).

The capacitance per unit area was found to be equal to 6.2 nF/cm^2. The PVP films exhibit excellent dielectric properties with large breakdown voltage over 100 V and sufficiently low leakage current densities in the 10^{-7}-10^{-8} A/cm^2 range at device operating voltages, as shown in Figure 7.7c. The capacitance does not significantly change for wide frequency sweeps (20 Hz - 2 MHz) as shown in Figure 7.7d. These results indicate that the spray-coated PVP films have good film quality and meet the requirement for the gate dielectric of flexible OFETs.
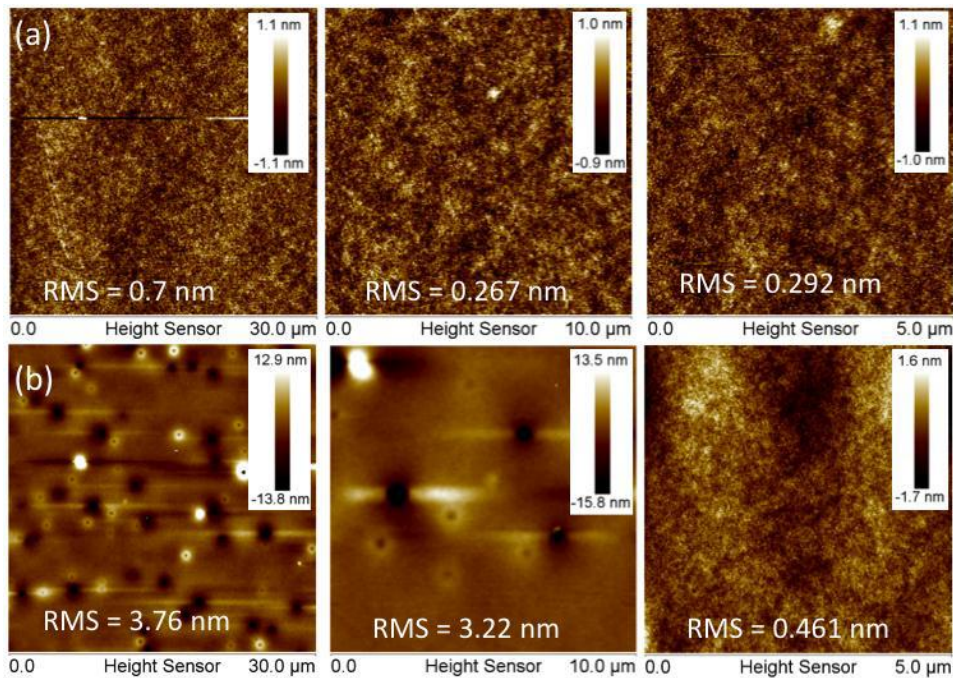
Figure 7.8. AFM morphologies and corresponding RMS roughnesses of (a) spin-coated and (b) ultrasonic spray-coated PVP films on different length scales.

After the formation of the dielectric layer, the TIPS-PEN semiconductor was subsequently spray-coated on top of the PVP film. The spray-coated TIPS-PEN solution does not dissolve the PVP film and long ribbon-shaped TIPS-PEN polycrystals form on the spray-coated PVP layer, as shown in Figure 7.7b, similar to that observed on SiO_2/Si substrate. Devices with spray-coated,

cross-linked PVP on highly doped silicon substrate exhibited an average mobility of 0.11 ± 0.03 cm^2/Vs. This is comparable to the values achieved for devices using spin-coated cross-linked PVP as the insulator layer on silicon substrate (Table 7.1).
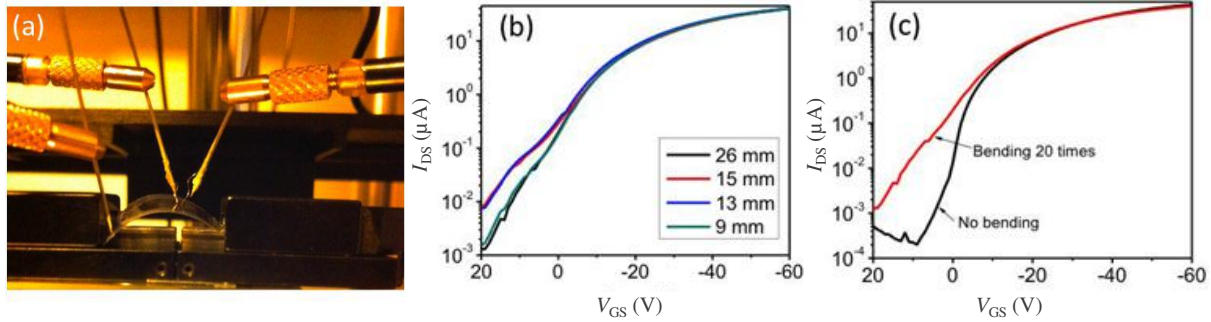
Figure 7.9. (a) A digital camera image of the OFET devices on a PET substrate in a bent configuration during electrical measurement. (b) No significant change of transfer characteristics of OFET with different bend radius values, R (26 mm, 15 mm, 13 mm, 9 mm). (c) No significant change of transfer characteristics of OFET after 20 cycles bending (R = 9 mm) are observed (before: black line, after: red line). The transfer curves are measured in the saturation regime at a drain bias of -40 V.

After achieving excellent performance on Si substrates, a series of flexible TIPS-PEN OFETs were fabricated flexible PET substrates with patterned ITO electrodes using sequentially spray-coated layers of PVP dielectric and TIPS-PEN semiconductor, as shown in the inset of Figure 7.7e. The spray-coated, flexible OFETs exhibited the maximum mobility of 0.35 cm^2/Vs, with an average mobility 0.12 ± 0.02 cm^2/Vs, a threshold voltage of 11.3 ± 2.5 V, and an on-off current ratio $>10^4$, as shown in Figures 7.7e and f. Device parameters of the TIPS-PEN OFETs fabricated on rigid and flexible substrates using sequential USC process are summarized in Table 7.1. In all cases, the mobilities and on/off ratios are consistent with those obtained in other solution-processing methods. Additionally, a bending test demonstrated no deterioration in the drain current even when the devices were bent to a bending radius as small as 9 mm. No

significant changes in the OFET performance after 20 bending cycles were observed except a slight increase in the off current (**Figure 7.9**), probably due to the polymer dielectric or TIPS-PEN degradation [181,182].

7.4 Conclusion

In summary, the ultrasonic spray-coating (USC) process was demonstrated for coating small molecule semiconductor and polymer insulator films for high-performance OFETs. Aligned, well-organized, ribbon-shaped TIPS-PEN polycrystal films were formed on both rigid and flexible substrates using the ultrasonic spray process. The spray-coated, cross-linked PVP dielectric films have smooth surfaces over large area along with excellent dielectric properties. Thus, the high-performance, flexible OFETs were fabricated using sequentially spray-coated TIPS-PEN semiconductor and PVP insulator layers on a plastic substrate at optimized processing parameters, including the choice of solvent, solution infuse rate, nozzle-substrate distance, and nozzle moving speed. The TIPS-PEN OFETs exhibited excellent device performance with a maximum hole mobility 0.36 cm^2/Vs, a low threshold voltage -1 V and on-off current ratio larger than 10^5, which are comparable or even superior to those obtained with conventional solution processing methods such as drop-casting and spin-coating. The results successfully demonstrated USC as a promising, cost-effective, and scalable technique to fabricate large-area and flexible OFETs for industrial production.

Chapter 8: Polymer Binder-Induced Crystal Growth and Its Effect on OFET Performance

In this chapter, an in-depth structure and performance study of TIPS-PEN based OFETs is discussed, where three polystyrene (PS) based insulating polymer binders with different branching architectures – linear PS, 4-arm star PS and centipede PS – were incorporated into the active layer. The phase separation profile and nanostructure in the thin blend films were characterized by a combination of complementary experimental techniques including UV-vis absorption, NR, XRD, plane-view and cross-section TEM.

8.1 Why Polymer Binder?

A promising approach to improve the solution processability of small molecule semiconductors is to add an insulating polymer binder, which acts as a wetting agent. By combining the excellent film formation capability and mechanical properties of a polymer and the high charge carrier mobility of a small molecule semiconductor, it is possible to deposit high-quality, highly-crystalline films, and fabricate high-performance OFETs. Previous studies reported that incorporating insulating polymer binders such as poly(α-methylstyrene) (PαMS), amorphous polystyrene (PS), amorphous polycarbonate (APC), or even semiconducting polymer like poly(triarylamines) (PTAA) into TIPS-PEN significantly improve the device performance uniformity without sacrificing the intrinsic high charge carrier mobility of small molecule semiconductors [183-188]. A fine control of vertical phase segregation of small molecules in the insulating polymer binder towards to the semiconductor/dielectric interface is believed to be important to achieve surprisingly superior OFET performance (mobility, on/off ratio, and threshold voltage) over those of neat small molecule system [189,190]. However, the vertical

phase separation and interplay between small molecules and polymers, due to competing effects of different interface energies and film growth kinetics, is a complex process.

Most of the previous studies mainly focused on the properties of polymer binder and effects of different solvents on morphology and device performances. For example, Kang et al. found that the molecular weight (M_w) of polymer strongly affects the phase separation in blend films [191]. Madec et al studied the effect of molecular weight of polymer binder and at the same time binary solvents on film growth and cystallinity of TIPS-PEN [192]. More recently, Cho and coworkers investigated the effect of solution viscosity and solvent properties on the phase separation [184]. However, very few studies have addressed how the structures of insulating polymer binders affect the crystallization, molecular packing, and phase separation of small molecule semiconductor, and associated electrical properties of small molecule/polymer OFETs.

This work reports the effects of different branch/chain architectures of three different polystyrene (PS) based polymer binders [193] – linear PS, 4-arm star PS, and centipede PS (**Figure 8.1**) – on the phase separation and crystallization TIPS-PEN, and resulting electrical performance of fabricated OFETs. The variations in the vertical composition profiles and order of crystallinity in the blend films explain the significant impacts of the polymer binder choice on the electrical performance of these films in the solution-processed OFETs. Although based on the same monomer, the different number of branches in each PS chain architecture impacts the diffusion process, and consequently influences the crystallization and phase separation of TIPS-PEN. Therefore, an in-depth understanding of the blend system is essential to understand whether branching is a promising approach to control the phase separation in the small molecule/polymer blend system. The capability of inducing vertical phase separation profile

rearrangement of small molecule/polymer blend through the topographic structure of polymer matrix appears to be an alternative approach to modify charge transport and OFET performance.

8.2 Experimental Section

8.2.1 Material and Solution Preparation

TIPS-PEN was separately blended with three different polymer binders, 4-arm star PS ($M_w = 483$ Kg/mol), linear PS ($M_w = 486$ Kg/mol), and centipede PS ($M_w = 540$ Kg/mol) at a weight ratio of 1:1, and dissolved in toluene at a total concentration of 5 mg/ml. Each solution was spray-coated on SiO_2/Si^{++} substrates in air using the USC process. For reference, neat TIPS-PEN solution in toluene was also spray-coated with similar conditions except a different (8 mg/ml) concentration.

8.2.2 Device Fabrication and Testing

BG/TC architecture was incorporated for the OFET fabrication. Prior to the deposition of organic thin films, heavily doped n-type silicon substrates with 250 nm thermally-grown SiO_2 dielectric layer were cleaned using the same recipe mentioned in Chapter 7. TIPS-PEN solution with or without polymer binder was directly spray-coated onto the SiO_2 surface using the following parameters: an atomizing gas pressure of 0.4 psi, a solution flow rate of 1.2 ml/min, nozzle-to-substrate distance of 4.6 cm, nozzle path speed of 8 mm/s, and a substrate tilting angle of 3°. Finally, 50 nm-thick Au source and drain electrodes were deposited by thermal evaporation at 1 Å/s using a shadow mask to complete the devices. The electrical characteristics of OFETs were measured following the procedure described in Chapter 7.

8.2.3 Thin Film Characterization

NR experiment was conducted at SNS, ORNL using the Liquids Reflectometer (Beamline-4B). To prepare films for NR measurements, 2"-diameter Si substrates were cleaned, and the solutions

were spin-coated on them at 600 rpm for 1 min. In order to account for the instrumental smearing

of NR data, the instrumental resolution provided from the beam line was convoluted with the

calculated NR curves. AFM images were acquired with a Bruker Dimension Icon operating in

tapping mode. TEM images were collected using a Zeiss Libra 120 with an in-column energy

filter or a Hitachi HF3300. Cross-section TEM with FIB was conducted at University of

Tennessee.
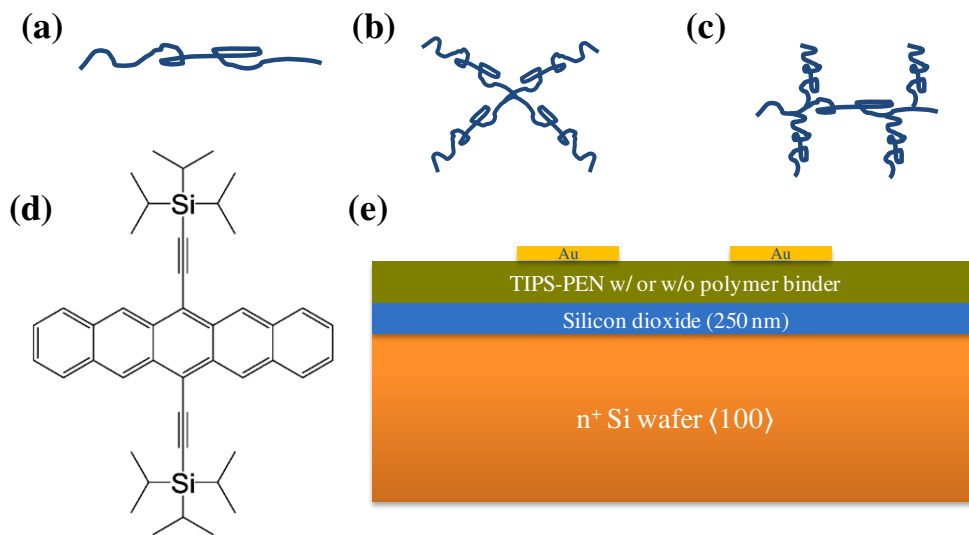
Figure 8.1. (a,b,c) Schematic of the chain architectures of the PS binders used: (a) linear PS, (b) 4-arm star PS, and (c) centipede PS. (d) Chemical structure of TIPS-PEN. (e) Schematic configuration of device cross-section.

8.3 Results and Discussion

OFETs with a BG/TC configuration (Figure 8.1e) were fabricated using neat TIPS-PEN, and

TIPS-PEN separately blended with 4-arm star PS, linear PS, and centipede PS, by using the USC

process discussed in Chapter 5 and 7. **Figure 8.2**a shows a set of typical transfer curves of

devices based on neat TIPS-PEN and TIPS-PEN:PS blend films. Figure 8.2b shows the average

mobilities based on more than 20 devices from each type of polymer binder. Neat TIPS-PEN based OFETs exhibited an average mobility of 0.1 cm^2/V-s. The addition of 4-arm star PS, linear PS, and centipede PS binders into TIPS-PEN increased the average mobility to 0.264, 0.374, and 0.446 cm^2/V-s, respectively. Detailed device performance parameters are summarized in **Table 8.1**.
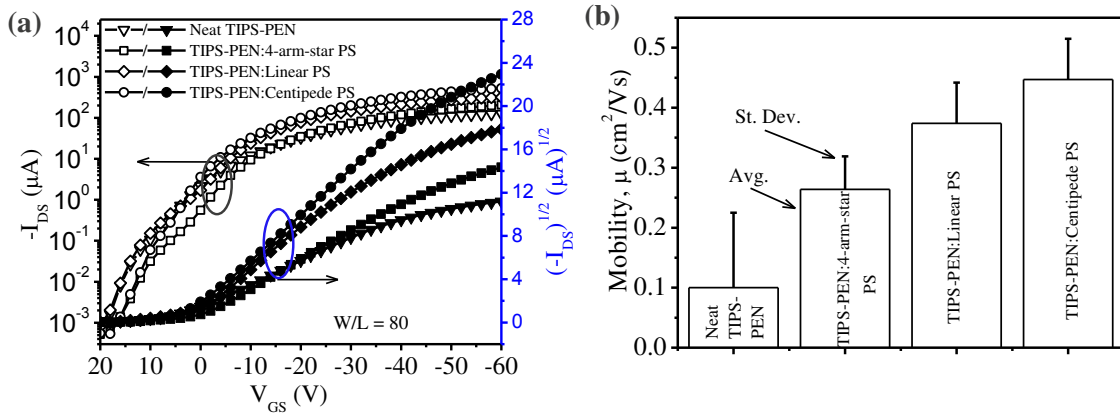
Figure 8.2. (a) Typical transfer characteristics of Neat TIPS-PEN and TIPS-PEN:PS blend devices. (b) Average mobility of devices based on TIPS-PEN and TIPS-PEN with three different polymer binders.

Table 8.1: Electrical properties of OFETs based on TIPS-PEN and TIPS-PEN:PS blend films using BG/TC device geometry. The mobilities were calculated at the saturation region at a drain bias of -40 V.

Blend type	Mobility [cm^2/V-s]	V_{Th} [V]	On-off ratio	Subthreshold Slope [V/decade]
Neat TIPS-PEN	0.099 ± 0.125	1.50	8.48×10^4	4.91
TIPS-PEN:4-arm star PS	0.264 ± 0.055	-0.60	7.75×10^5	2.23
TIPS-PEN:linear PS	0.374 ± 0.068	-1.50	6.12×10^5	1.91
TIPS-PEN:centipede PS	0.448 ± 0.068	-1.50	3.25×10^5	1.58

Notably, blending TIPS-PEN with centipede PS led to an over four-fold increase in average mobility. Moreover, the ratio of average mobility to the standard deviation of the measured mobility (μ_{Stdev}/μ_{Stdev}) was increased eight-fold, indicating a significant enhancement in device-to-device uniformity over neat TIPS-PEN, which is also illustrated by device performance histogram shown in **Figure 8.3**. This interesting simultaneous improvement of average mobility and performance uniformity is in good agreement with previous reports [191,194]. However, no significant difference was observed in device stability in air ambient induced by polymer binders, as shown in **Figure 8.4**. The excellent device stability could be attributed to the good air stability of TIPS-PEN, combined with passivating effect of polymer binders.
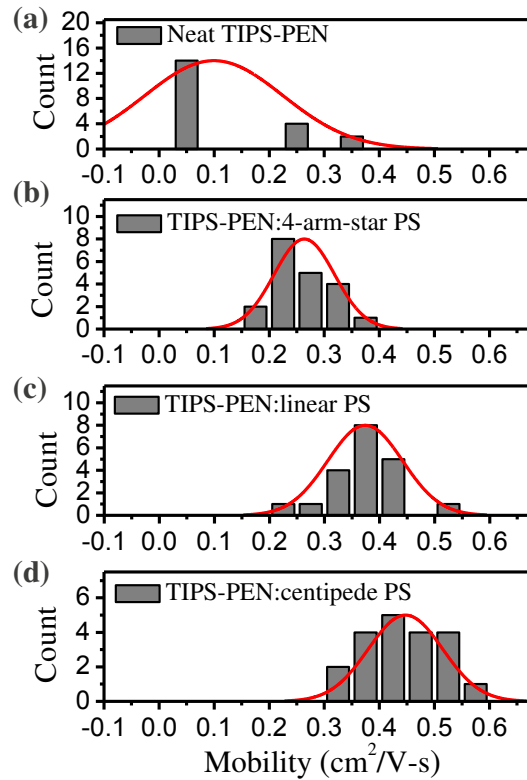
Figure 8.3. Histogram of devices performances based on neat TIPS-PEN and TIPS-PEN:PS blends. Gaussian fits are given as guide to eye.

In order to understand the performance variation among various TIPS-PEN:PS blends, the relationship between the measured OFET electrical properties and microstructure of blend films were investigated using a combination of characterization techniques. The surface morphologies of blend films of TIPS-PEN:PS were studied by AFM (**Figure 8.5**). As shown, neat TIPS-PEN film showed a step-terrace geometry, indicative of its highly crystalline nature. The step height was around 1.65 nm, which is in agreement with the vertical intermolecular spacing of (001) plane, as previous reports [173]. Similar characteristic terrace topography was also observed in TIPS-PEN:4-arm star PS and TIPS-PEN:centipede PS blend films. However, a more homogeneous topography was observed in TIPS-PEN:linear PS blend film. Therefore, it was speculated that a thin layer of PS formed on the surface of TIPS-PEN:linear PS blend film.
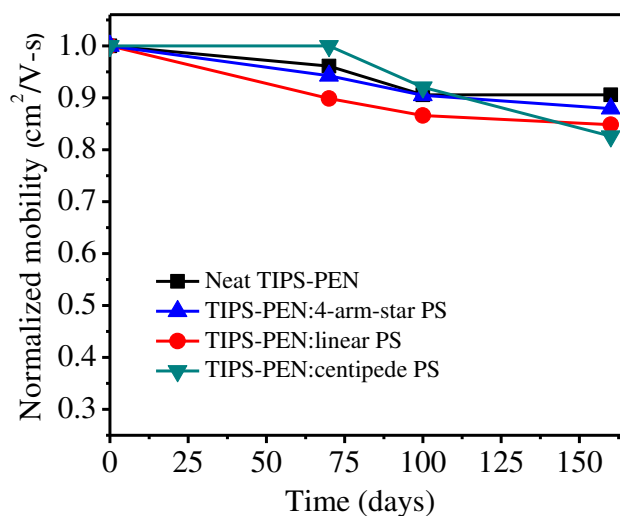
Figure 8.4. Stability test on device mobility: devices exhibit similar stability retaining 85-90% of their initial mobilities, while being stored in air.

In order to study the lateral phase morphology of TIPS-PEN:PS blend films, energy-filtered TEM was carried out, where each TIPS-PEN:PS blend film was imaged at 0 ± 5 eV and 20 ± 5

eV, as shown in **Figure 8.6**. Here, the 0 eV (elastic) image reveals the features based on electron density contrast, including mass thickness contrast and thickness variation. The 20 eV (inelastic) images correspond to the low plasmon contribution from the *p*-type organic semiconductor, in which the brighter area corresponds to TIPS-PEN rich domains and darker area corresponds to PS rich region. In the TIPS-PEN:4-arm star PS film, sharp TIPS-PEN crystal edges were observed, suggesting that there is mainly lateral phase separation between 4-arm star PS and TIPS-PEN. In contrast, fuzzy crystal edges were observed in TIPS-PEN:linear PS blend film, suggesting that phase separation is more dominant along vertical direction. And, slightly rounded TIPS-PEN edge with still recognizable crystal shapes was found in TIPS-PEN:centipede PS film. Hence, it is possible that a combination of vertical and lateral phase separation mode underwent in the blend films.
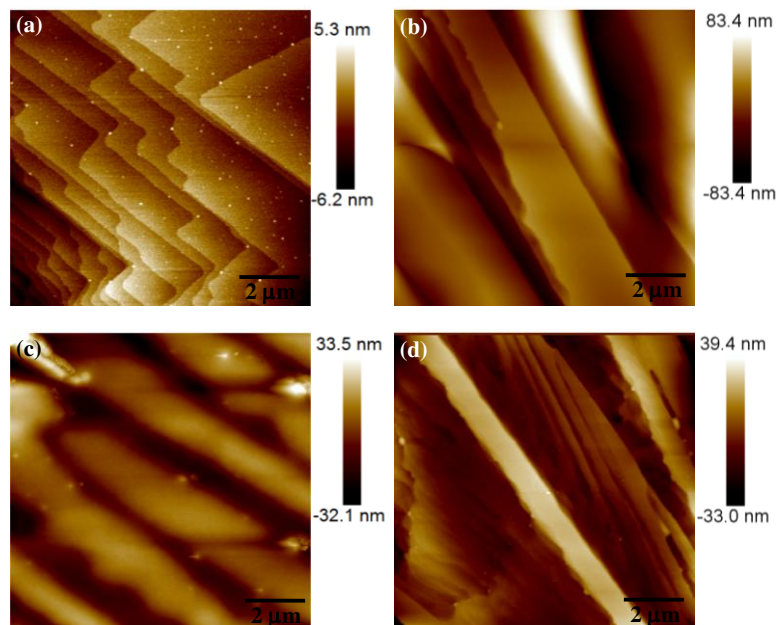
Figure 8.5. AFM images of a) neat TIPS-PEN b) TIPS-PEN:4-arm star PS, c) TIPS-PEN:linear PS, and d) TIPS-PEN:centipede PS.
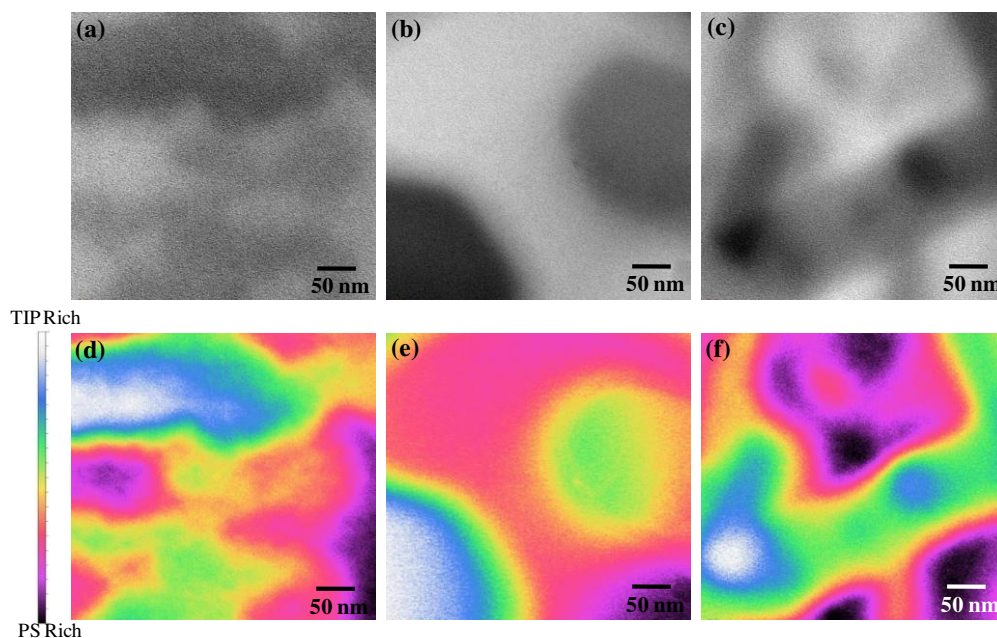
Figure 8.6. TEM images of TIPS-PEN:linear PS (a,d), TIPS-PEN:4-arm star PS (b,e), and TIPS-PEN:centipede PS (c,f) at 0 eV (a-c) and 20 eV (d-f).

In order to investigate vertical phase separation, EFTEM was employed on the cross-sections of TIPS-PEN:PS blend films (**Figure 8.7**), where the cross sections were prepared by focused ion beam (FIB). To better distinguish the small molecule TIPS-PEN and PS binder, EFTEM was used in the energy range targeted to Si to locate TIPS-PEN rich phase. In TIPS-PEN:4-arm star PS blend film, a distinct bi-layer structure was observed, with a TIPS-PEN rich layer at air interface and an underlying 4-arm star PS rich layer at the gate/dielectric interface. TIPS-PEN:linear PS blend film exhibited a tri-layer morphology in which TIPS-PEN mainly segregated towards near the gate/dielectric interface. This vertical phase separation feature is critically important for the charge carrier transport in the incorporated BG/TC OFET architecture. Unlike TIPS-PEN:4-arm star PS film, no strong TIPS-PEN aggregation was observed at the air interface in TIPS-PEN:linear PS blend film. This observation is in accordance with the AFM results revealing the presence of a thin layer of PS on top of the TIPS-PEN:linear

PS film. On the other hand, TIPS-PEN:centipede PS film did not show any clear multi-layer structure. No abrupt interface was observed in the blend layer, rather from the TEM image with Si tracing, an increased TIPS-PEN concentration gradient was found towards air interface.
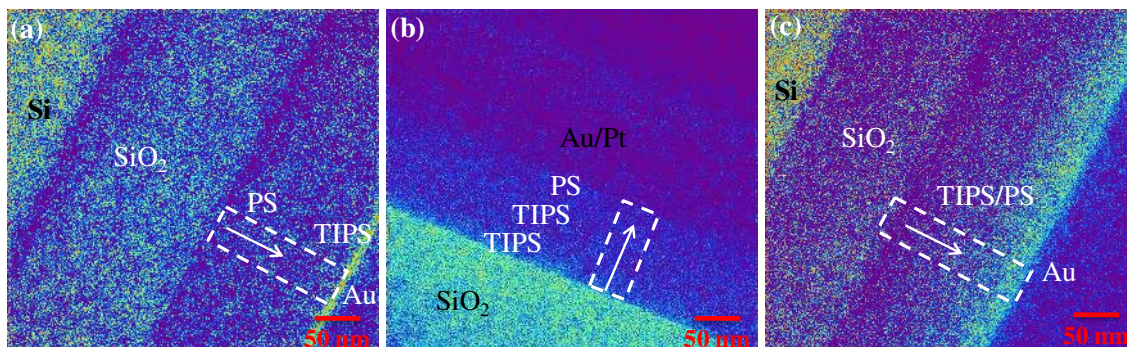
Figure 8.7. Cross-section EFTEM images for a) TIPS-PEN:4-arm star PS, b) TIPS-PEN:linear PS, and c) TIPS-PEN:centipede PS films.

Neutron reflectivity (NR) also can provide insight into vertical phase morphology, and provides quantitative information about layer thickness in nanometer resolution, presence of multi-layers, and composition gradient as well. **Figure 8.8**a shows the experimental and fitted NR curves for each blend film, where fitting to the experimental NR curves were performed using Parratt formalism [101] from which obtained neutron scattering length density (SLD) distributions and the composition distributions of TIPS-PEN ($Vol_{TIPS-PEN}$), calculated from the SLD distributions, are depicted in Figure 8.8b-c. Each blend film of TIPS-PEN exhibits high contrast, where Kiessig fringes with different frequency/period mean that different blend films have different thicknesses. Relatively high-frequency fringes in case of TIPS-PEN:linear-PS film indicates thicker film. It should be noted here that due to the requirement of smooth films for neutron reflectometry experiments, the films were prepared by spin-coating. After converting

SLDs to volume fraction profiles, we can see that TIPS-PEN:4-arm star-PS blend film has polymer rich regions at the dielectric interface and TIPS-PEN was segregated to air interface. TIPS-PEN:linear-PS blend film has the highest percentage of TIPS-PEN at the dielectric interface compared to other two blend films and its air interface is polymer rich with a decreasing volume gradient of TIPS-PEN. It is worth noting here that the segregation of TIPS-PEN molecules to the gate-dielectric interface is important for device performance as charge transport occurs within a narrow region adjacent to the dielectric layer [189].
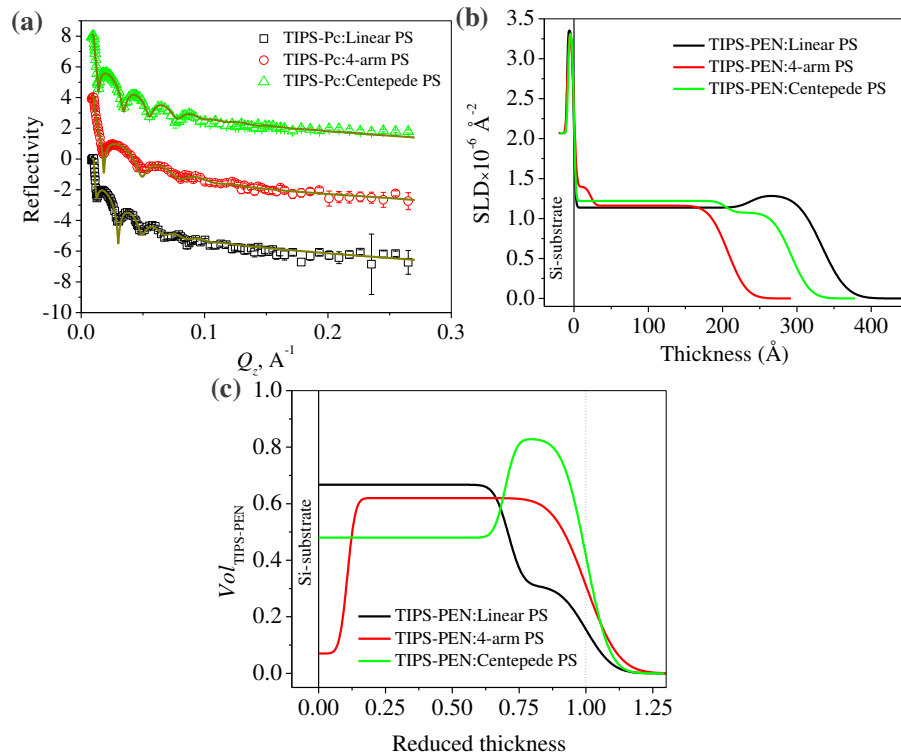
Figure 8.8. a) Experimental and modeled NR curves for TIPS-PEN films separately blended with linear PS, 4-arm star PS, and centipede PS b) The SLD profiles used to fit the NR curves shown in (a). c) Volume fraction profiles of TIPS-PEN vs. reduced distance from the substrate, $Z_{reduced}$ calculated from the SLD profiles shown in (b).

On the other hand, though centipede PS has smaller percentage of TIPS-PEN at the gate/dielectric interface compared to linear PS, the film is TIPS-PEN rich along thickness direction with a positive gradient towards the air interface, meaning that it has a better injection of charge carriers. Better injection in case of TIPS-PEN:centipede PS film was also reflected in the output characteristics of TIPS-PEN:centipede PS OFET as shown in **Figure 8.9**, unarguably explaining better device performance based on TIPS-PEN:centipede PS blend films.
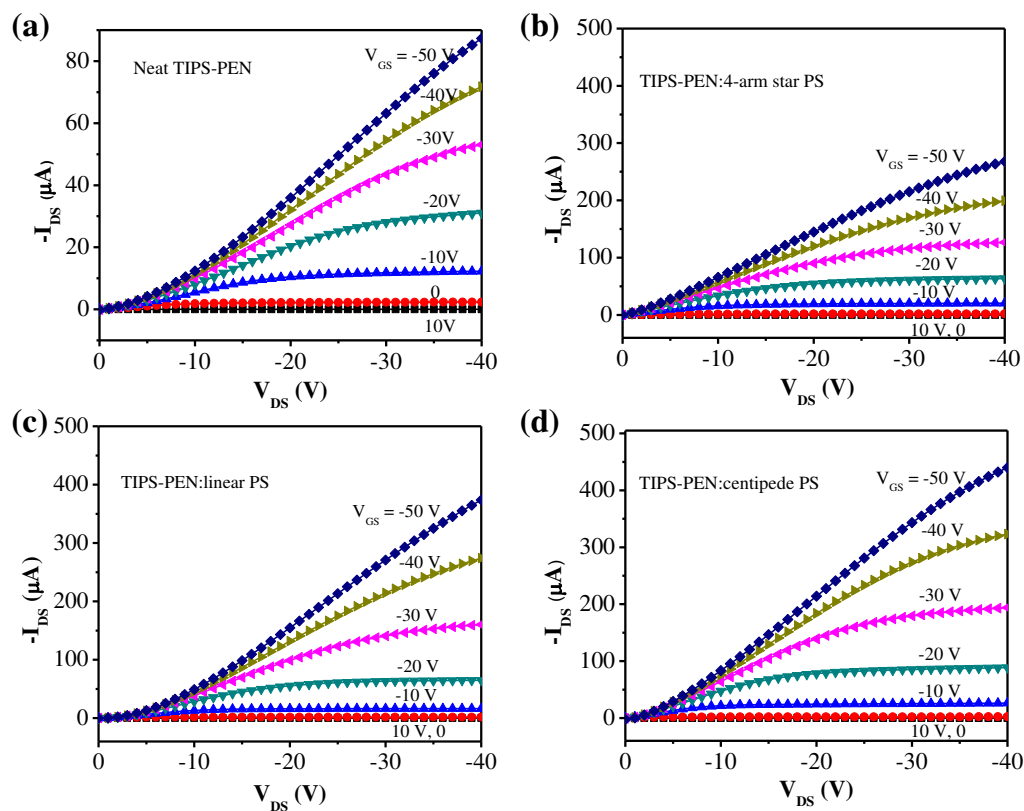
Figure 8.9. Typical output characteristics of devices based on: a) neat TIPS-PEN, b) TIPS-PEN:4-arm star PS, c) TIPS-PEN:linear PS, and d) TIPS-PEN:centipede PS. Same scale is used for the blends to illustrate the difference in charge injection.

8.4 Conclusion

In summary, the topographic effects of different branch/chain architectures of three different polystyrene based polymer binders – 4-arm star PS, linear PS, and centipede PS – on vertical and lateral phase separation, crystallinity of TIPS-PEN small molecules, and resulting OFET performances were unraveled in this work. It was demonstrated that each of these binders improves film formation capability and uniformity of TIPS-PEN, significantly enhances device performance, and minimizes device-to-device performance variation. The device performance was correlated with neutron reflectivity and cross-section TEM data, and the results were well-consistent. Overall, TIPS-PEN:centipede PS based devices exhibited the best performance with an average mobility of 0.45 cm^2/V-s and excellent charge transport.

Chapter 9: Conclusion and Future Works

9.1 Original Contributions

The original contributions of this dissertation to electronic and optoelectronic device research are briefly described as follows-

A. Interface and morphology engineering in a state-of-the-art organic photovoltaic system, PTB7:PC$_{71}$BM was presented. The higher power conversion efficiency of devices with inverted architecture compared to those with regular architecture was correlated with nanoscale structures. It has been shown that the higher performance from inverted devices is due to the diffusion of electron accepting fullerene molecules into ITO surface modifying PFN layer.

B. How the processing additive and annealing temperature affect the nanoscale morphology in small molecule solar cells is presented. The device performance was correlated with film morphology and crystallinity, providing guidelines for better solar cell design.

C. High-efficiency perovskite solar cells (PSCs) were fabricated using a roll-to-roll compatible ultrasonic spray-coating (USC) process. The spray-coating system parameters such as substrate temperature, nozzle path speed, nozzle-to-substrate distance, and spray pressure were thoroughly optimized to achieve highly uniform and dense perovskite thin films. Devices based on the obtained films exhibited PCE as high as 13.0% with an average PCE more than 10%. A unique photonic curing technique was used for the first time to anneal electron transporting TiO$_2$ compact layer on flexible PET substrates to realize flexible and mechanically robust PSCs with PCE up to 8.1%.

112

D. The photonic curing technique was further optimized to anneal TiO_2 layers on top of both glass and flexible substrates. Combined with controlled and optimized perovskite film growth by introducing moisture during annealing, photonic-cured TiO_2 films yielded PCE as high as 15.0%, comparable to the best solution-processed PSCs.

E. To demonstrate versatility of USC process, a series of high-performance small molecule (TIPS-pentacene)-based organic field-effect transistors were fabricated. The average mobility was as high as 0.35 cm^2/V-s with on-off ratio being $>10^4$.

F. TIPS-pentacene crystal growth and orientation were further optimized by using a series of polystyrene (PS)-based insulating polymers - 4-arm star, centipede, and linear PS. The devices exhibited enhanced mobility and on-off ratio with highest being 1.0 cm^2/V-s and 8.4×10^6, respectively.

9.2 Future Works

Both organic and perovskite solar cells have great potentials to see the light of commercialization and vast deployment in the future. Before that, however, certain issues need to be addressed. Following could be the research directions that will further advance these two technologies towards reality.

9.2.1 Organic Solar Cells

Reported PCE of lab based single-junction OSCs has already surpassed the widely considered commercialization threshold of 10%. However, the reported devices are too small with area in the range of 10-30 mm^2. Taking the scaling into consideration, the efficiency will be much lower due to decreased fill factor. That is why further enhancement of cell efficiency is of paramount importance, and there are certainly scopes of process and materials engineering to achieve that.

Another common concern with OSCs is their poor stability. Though development of inverted device architecture and advanced encapsulation technique led to significantly improved device stability, it still needs further improvement. Based on the works reported in this dissertation, following works could be significant.

a) We observed that the diffusion of electron accepting fullerene into ITO electrode modifying layer, PFN (which is a conjugated polymer) is the reason behind higher efficiency in inverted devices. There is a cross-linked version of PFN, called PFN-OX, which is shown to outperform PFN. It would be interesting to see whether any such diffusion occurs if this polymer is used as the ITO modifying layer. And also, study of bulk-heterojunction system based on a better performing polymer, PTB7-Th, would be quite interesting.

b) Small molecule-based OSCs show comparable efficiencies to those of polymer-based cells. Based on the results presented here, it is possible that processing additive can be optimized to further tune the active layer morphology. Interface engineering also has many scopes of study. For instance, incorporating nanoparticles (Ag, Au, etc.) into interfacial layer or absorber layer can enhance the light absorption and thus device performance. Moreover, above mentioned PFN and PFN-OX surface modifying layers can be investigated in small molecules solar cells.

9.2.2 Perovskite Solar Cells

Perovskite solar cells already reached more than 20% certified PCE. However, PSCs currently suffer from poor stability and strong J-V hysteresis, which, if not addressed in time, will prevent the timely commercialization of this technology. Moreover, there is still a great possibility to

114

push the PCE to the theoretical maximum, which is estimated to be more than 30% [195]. Hence, considering the efficiency enhancement, high reproducibility, performance stability, flexible device realization, better understanding of underlying physics, and most importantly, the scalability, following issues require strong attention:

a) First, hysteresis is one of major concerns associated with PSCs. The presence of hysteresis in current density-voltage ($J$$-$$V$) characteristics makes it difficult to reliably quantify the cell performance. Hysteresis in solar cells is usually assumed to arise from the cell capacitance – fast scanning under forward bias conditions eases the extraction of both extra-capacitive and photogenerated charges, but in case of fast scanning from short-circuit to forward bias, the photogenerated charge cannot fully charge the solar cells, reducing the amount of charge flowing through the external circuit. However, hysteresis in PSCs does not follow this trend; they show strong hysteresis effect at both faster and slower scans. Though there have already been several reported works on this issue, the origins are not clearly understood yet.

b) Second, it is critically important to understand how moisture, extended exposure to UV light, and other environmental variation (e.g., temperature variation) affect PSCs. One of the most important questions to address is how the water molecules first react with perovskite – does the reaction initiate at the air interface or in the bulk region through the grain boundaries? Better understanding of device physics, interfaces, and underlying mechanism of material decomposition and performance degradation will help designing more stable PSCs.

c) Last, one of the most important parameters that determine perovskite solar cell performance is the perovskite thin film morphology per se. Depositing highly uniform and dense perovskite thin films over large area remains a big challenge as of today. Scalable techniques such as spray-coating and ink-jet printing can be employed and optimized to enable large-scale fabrication of PSCs. ORNL's scalable ultrasonic spray-coating (USC) process was used in one of our previous works to deposit mixed halide perovskite ($CH_3NH_3PbI_{3-x}Cl_x$, E_g = 1.55 eV) thin films, where associated devices demonstrated PCE of 13%. The USC technique is capable of yielding highly uniform and dense perovskite thin films over large area with a very low density of pinholes, without requiring inert environment, which is one of the fundamental requirements for perovskite film deposition. Using lower bandgap (E_g < 1.5 eV) perovskite materials such as those using formamidinium organic cation, USC can yield photovoltaic cells with higher PCEs. Another scalable technique, ink-jet printing can be used to fabricate all-printed PSCs, without requiring expensive high-vacuum evaporation technique to deposit top metals, significantly reducing the processing and fabrication cost.

References

[1] http://www.eia.gov/tools/faqs/faq.cfm?id=427&t=3.

[2] http://www.euronuclear.org/info/encyclopedia/p/pow-gen-ger.htm.

[3] D. E. Carlson, C. R. Wronski, Amorphous silicon solar cell. *Appl. Phys. Lett.* **28**, 671-673 (1976).

[4] Y. Tawada, H. Okamoto, Y. Hamakawa, a-SiC:H/a-Si:H heterojunction solar cell having more than 7.1% conversion efficiency. *Appl. Phys. Lett.* **39**, 237-239 (1981).

[5] Y. Tawada, K. Tsuge, M. Kondo, H. Okamoto, Y. Hamakawa, Properties and structure of a-SiC:H for high-efficiency a-Si solar cell. *J. Appl. Phys.* **53**, 5273-5281 (1982).

[6] A. M. Gabor, J. R. Tuttle, D. S. Albin, M. A. Contreras, R. Noufi, A. M. Hermann, High-efficiency $CuIn_xGa_{1-x}Se_2$ solar cells made from $(In_xGa_{1-x})_2Se_3$ precursor films. *Appl. Phys. Lett.* **65**, 198-200 (1994).

[7] J. R. Tuttle, M. A. Contreras, T. J. Gillespie, K. R. Ramanathan, A. L. Tennant, J. Keane, A. M. Gabor, R. Noufi, Accelerated publication 17.1% efficient $Cu(In,Ga)Se_2$-based thin-film solar cell. *Prog. Photovolt: Res. Appl.* **3**, 235-238 (1995).

[8] T. L. Chu, S. S. Chu, C. Ferekides, C. Q. Wu, J. Britt, C. Wang, 13.4% efficient thin-film CdS/CdTe solar cells. *J. Appl. Phys.* **70**, 7608-7612 (1991).

[9] J. Britt, C. Ferekides, Thin-film CdS/CdTe solar cell with 15.8% efficiency. *Appl. Phys. Lett.* **62**, 2851-2852 (1993).

[10] W. Shockley, H. J. Queisser, Detailed Balance Limit of Efficiency of p-n Junction Solar Cells. *J. Appl. Phys.* **32**, 510-519 (1961).

[11] C. W. Tang. (Google Patents, 1979).

[12] J. M. Olson, S. R. Kurtz, A. E. Kibbler, P. Faine, A 27.3% efficient $Ga_{0.5}In_{0.5}P$/GaAs tandem solar cell. *Appl. Phys. Lett.* **56**, 623-625 (1990).

[13] B. O'Regan, M. Gratzel, A low-cost, high-efficiency solar cell based on dye-sensitized colloidal TiO_2 films. *Nature* **353**, 737-740 (1991).

[14] K. Tennakone, G. R. R. A. Kumara, A. R. Kumarasinghe, K. G. U. Wijayantha, P. M. Sirimanne, A dye-sensitized nano-porous solid-state photovoltaic cell. *Semicond. Sci. Technol.* **10**, 1689 (1995).

[15] M. C. Beard, K. P. Knutsen, P. Yu, J. M. Luther, Q. Song, W. K. Metzger, R. J. Ellingson, A. J. Nozik, Multiple Exciton Generation in Colloidal Silicon Nanocrystals. *Nano Lett.* **7**, 2506-2512 (2007).

[16] A. J. Nozik, Quantum dot solar cells. *Physica E* **14**, 115-120 (2002).

[17] A. Kojima, K. Teshima, Y. Shirai, T. Miyasaka, Organometal Halide Perovskites as Visible-Light Sensitizers for Photovoltaic Cells. *J. Am. Chem. Soc.* **131**, 6050-6051 (2009).

[18] N. J. Jeon, J. H. Noh, Y. C. Kim, W. S. Yang, S. Ryu, S. I. Seok, Solvent engineering for high-performance inorganic–organic hybrid perovskite solar cells. *Nat. Mater.* **13**, 897-903 (2014).

[19] http://www.nrel.gov/ncpv/images/efficiency_chart.jpg, accessed on August 06, 2015.

[20] J. C. Bernede, Organic photovoltaic cells: History, principles and techniques. *J. Chilean Chem. Soc.* 53, 1549–1564 (2008).

[21] J. D. Servaites, M. A. Ratner, T. J. Marks, Organic solar cells: A new look at traditional models. *Energy Environ. Sci.* **4**, 4410-4422 (2011).

[22] R. Hulstrom, R. Bird, C. Riordan, Spectral solar irradiance data sets for selected terrestrial conditions. *Sol. Cells* **15**, 365-391 (1985).

[23] P. Würfel, U. Würfel. Physics of solar cells: from basic principles to advanced concepts. *John Wiley & Sons*, 2009.

[24] M. D. McGehee, M. A. Topinka, Solar cells: Pictures from the blended zone. *Nat. Mater.* **5**, 675-676 (2006).

[25] C. W. Tang, Two-layer organic photovoltaic cell. *Appl. Phys. Lett.* **48**, 183-185 (1986).

[26]P. Peumans, S. R. Forrest, Very-high-efficiency double-heterostructure copper phthalocyanine/C60 photovoltaic cells. *Appl. Phys. Lett.* **79**, 126-128 (2001).

[27] B. Kraabel, C. H. Lee, D. McBranch, D. Moses, N. S. Sariciftci, A. J. Heeger, Ultrafast photoinduced electron transfer in conducting polymer—buckminsterfullerene composites. *Chem. Phys. Lett.* **213**, 389-394 (1993).

[28] S. E. Shaheen, C. J. Brabec, N. S. Sariciftci, F. Padinger, T. Fromherz, J. C. Hummelen, 2.5% efficient organic plastic solar cells. *Appl. Phys. Lett.* **78**, 841-843 (2001).

[29] S. Alem, R. de Bettignies, J.-M. Nunzi, M. Cariou, Efficient polymer-based interpenetrated network photovoltaic cells. *Appl. Phys. Lett.* **84**, 2178-2180 (2004).

[30] P. Schilinsky, C. Waldauf, C. J. Brabec, Recombination and loss analysis in polythiophene based bulk heterojunction photodetectors. *Appl. Phys. Lett.* **81**, 3885-3887 (2002).

[31] G. Li, V. Shrotriya, J. Huang, Y. Yao, T. Moriarty, K. Emery, Y. Yang, High-efficiency solution processable polymer photovoltaic cells by self-organization of polymer blends. *Nat. Mater.* **4**, 864-868 (2005).

[32] W. Ma, C. Yang, X. Gong, K. Lee, A. J. Heeger, Thermally Stable, Efficient Polymer Solar Cells with Nanoscale Control of the Interpenetrating Network Morphology. *Adv. Funct. Mater.* **15**, 1617-1622 (2005).

[33] M. Campoy-Quiles, T. Ferenczi, T. Agostinelli, P. G. Etchegoin, Y. Kim, T. D. Anthopoulos, P. N. Stavrinou, D. D. C. Bradley, J. Nelson, Morphology evolution via self-organization and lateral and vertical diffusion in polymer:fullerene solar cell blends. *Nat. Mater.* **7**, 158-164 (2008).

[34] T. A. Bull, L. S. C. Pingree, S. A. Jenekhe, D. S. Ginger, C. K. Luscombe, The Role of Mesoscopic PCBM Crystallites in Solvent Vapor Annealed Copolymer Solar Cells. *ACS Nano* **3**, 627-636 (2009).

[35] Y. Zhao, Z. Xie, Y. Qu, Y. Geng, L. Wang, Solvent-vapor treatment induced performance enhancement of poly(3-hexylthiophene):methanofullerene bulk-heterojunction photovoltaic cells. *Appl. Phys. Lett.* **90**, 043504 (2007).

[36] D. Chen, F. Liu, C. Wang, A. Nakahara, T. P. Russell, Bulk Heterojunction Photovoltaic Active Layers via Bilayer Interdiffusion. *Nano Lett.* **11**, 2071-2078 (2011).

[37] K. H. Lee, P. E. Schwenn, A. R. G. Smith, H. Cavaye, P. E. Shaw, M. James, K. B. Krueger, I. R. Gentle, P. Meredith, P. L. Burn, Morphology of All-Solution-Processed "Bilayer" Organic Solar Cells. *Adv. Mater.* **23**, 766-770 (2011).

[38] M. D. Irwin, D. B. Buchholz, A. W. Hains, R. P. H. Chang, T. J. Marks, *p*-Type semiconducting nickel oxide as an efficiency-enhancing anode interfacial layer in polymer bulk-heterojunction solar cells. *Proc.Natl. Acad. Sci* **105**, 2783-2787 (2008).

[39] G. Zhao, Y. He, Y. Li, 6.5% Efficiency of Polymer Solar Cells Based on poly(3-hexylthiophene) and Indene-C60 Bisadduct by Device Optimization. *Adv. Mater.* **22**, 4355-4358 (2010).

[40] C.-Y. Chang, C.-E. Wu, S.-Y. Chen, C. Cui, Y.-J. Cheng, C.-S. Hsu, Y.-L. Wang, Y. Li, Enhanced Performance and Stability of a Polymer Solar Cell by Incorporation of Vertically Aligned, Cross-Linked Fullerene Nanorods. *Angew. Chem. Int. Ed.* **50**, 9386-9390 (2011).

[41] W. Wang, H. Wu, C. Yang, C. Luo, Y. Zhang, J. Chen, Y. Cao, High-efficiency polymer photovoltaic devices from regioregular-poly(3-hexylthiophene-2,5-diyl) and [6,6]-phenyl-C61-butyric acid methyl ester processed with oleic acid surfactant. *Appl. Phys. Lett.* **90**, 183512 (2007).

[42] M. S. White, D. C. Olson, S. E. Shaheen, N. Kopidakis, D. S. Ginley, Inverted bulk-heterojunction organic photovoltaic device using a solution-derived ZnO underlayer. *Appl. Phys. Lett.* **89**, 143517 (2006).

[43] H.-H. Liao, L.-M. Chen, Z. Xu, G. Li, Y. Yang, Highly efficient inverted polymer solar cell by low temperature annealing of Cs2CO3 interlayer. *Appl. Phys. Lett.* **92**, 173303 (2008).

[44] C. Tao, S. Ruan, X. Zhang, G. Xie, L. Shen, X. Kong, W. Dong, C. Liu, W. Chen, Performance improvement of inverted polymer solar cells with different top electrodes by introducing a MoO3 buffer layer. *Appl. Phys. Lett.* **93**, 193307 (2008).

[45] G. Li, C.-W. Chu, V. Shrotriya, J. Huang, Y. Yang, Efficient inverted polymer solar cells. *Appl. Phys. Lett.* **88**, 253503 (2006).

[46] Z. He, C. Zhong, X. Huang, W.-Y. Wong, H. Wu, L. Chen, S. Su, Y. Cao, Simultaneous Enhancement of Open-Circuit Voltage, Short-Circuit Current Density, and Fill Factor in Polymer Solar Cells. *Adv. Mater.* **23**, 4636-4643 (2011).

[47] S. H. Park, A. Roy, S. Beaupre, S. Cho, N. Coates, J. S. Moon, D. Moses, M. Leclerc, K. Lee, A. J. Heeger, Bulk heterojunction solar cells with internal quantum efficiency approaching 100%. *Nat. Photonics* **3**, 297-302 (2009).

[48] J. S. Moon, J. Jo, A. J. Heeger, Nanomorphology of PCDTBT:PC$_{70}$BM Bulk Heterojunction Solar Cells. *Adv. Energy Mater.* **2**, 304-308 (2012).

[49] M. M. Wienk, J. M. Kroon, W. J. H. Verhees, J. Knol, J. C. Hummelen, P. A. van Hal, R. A. J. Janssen, Efficient Methano[70]fullerene/MDMO-PPV Bulk Heterojunction Photovoltaic Cells. *Angew. Chem. Int. Ed.* **42**, 3371-3375 (2003).

[50] L. Huo, S. Zhang, X. Guo, F. Xu, Y. Li, J. Hou, Replacing Alkoxy Groups with Alkylthienyl Groups: A Feasible Approach To Improve the Properties of Photovoltaic Polymers. *Angew. Chem. Int. Ed.* **50**, 9697-9702 (2011).

[51] X. Guo, M. Zhang, W. Ma, L. Ye, S. Zhang, S. Liu, H. Ade, F. Huang, J. Hou, Enhanced Photovoltaic Performance by Modulating Surface Composition in Bulk Heterojunction Polymer Solar Cells Based on PBDTTT-C-T/PC$_{71}$BM. *Adv. Mater.* **26**, 4043-4049 (2014).

[52] Y. Liang, Z. Xu, J. Xia, S.-T. Tsai, Y. Wu, G. Li, C. Ray, L. Yu, For the Bright Future—Bulk Heterojunction Polymer Solar Cells with Power Conversion Efficiency of 7.4%. *Adv. Mater.* **22**, E135-E138 (2010).

[53] Z. He, C. Zhong, S. Su, M. Xu, H. Wu, Y. Cao, Enhanced power-conversion efficiency in polymer solar cells using an inverted device structure. *Nat. Photonics* **6**, 591-595 (2012).

[54] S.-H. Liao, H.-J. Jhuo, P.-N. Yeh, Y.-S. Cheng, Y.-L. Li, Y.-H. Lee, S. Sharma, S.-A. Chen, Single Junction Inverted Polymer Solar Cell Reaching Power Conversion Efficiency 10.31% by Employing Dual-Doped Zinc Oxide Nano-Film as Cathode Interlayer. *Sci. Rep.* **4**, 6813 (2014).

[55] Z. He, B. Xiao, F. Liu, H. Wu, Y. Yang, S. Xiao, C. Wang, T. P. Russell, Y. Cao, Single-junction polymer solar cells with high efficiency and photovoltage. *Nat. Photonics* **9**, 174-179 (2015).

[56] J. Peet, J. Y. Kim, N. E. Coates, W. L. Ma, D. Moses, A. J. Heeger, G. C. Bazan, Efficiency enhancement in low-bandgap polymer solar cells by processing with alkane dithiols. *Nat. Mater.* **6**, 497-500 (2007).

[57] J. K. Lee, W. L. Ma, C. J. Brabec, J. Yuen, J. S. Moon, J. Y. Kim, K. Lee, G. C. Bazan, A. J. Heeger, Processing Additives for Improved Efficiency from Bulk Heterojunction Solar Cells. *J. Am. Chem. Soc.* **130**, 3619-3623 (2008).

[58] Y. Sun, G. C. Welch, W. L. Leong, C. J. Takacs, G. C. Bazan, A. J. Heeger, Solution-processed small-molecule solar cells with 6.7% efficiency. *Nat. Mater.* **11**, 44-48 (2012).

[59] A. K. K. Kyaw, D. H. Wang, D. Wynands, J. Zhang, T.-Q. Nguyen, G. C. Bazan, A. J. Heeger, Improved Light Harvesting and Improved Efficiency by Insertion of an Optical Spacer (ZnO) in Solution-Processed Small-Molecule Solar Cells. *Nano Lett.* **13**, 3796-3801 (2013).

[60] B. Kan, M. Li, Q. Zhang, F. Liu, X. Wan, Y. Wang, W. Ni, G. Long, X. Yang, H. Feng, Y. Zuo, M. Zhang, F. Huang, Y. Cao, T. P. Russell, Y. Chen, A Series of Simple Oligomer-like Small Molecules Based on Oligothiophenes for Solution-Processed Solar Cells with High Efficiency. *J. Am. Chem. Soc.* **137**, 3886-3893 (2015).

[61] M. Liu, M. B. Johnston, H. J. Snaith, Efficient planar heterojunction perovskite solar cells by vapour deposition. *Nature* **501**, 395-398 (2013).

[62] S. Pramod Kumar, R. K. Nagarale, S. P. Pandey, H. W. Rhee, B. Bhaskar, Present status of solid state photoelectrochemical solar cells and dye sensitized solar cells using PEO-based polymer electrolytes. *Adv. Nat. Sci.: Nanosci. Nanotechnol.* **2**, 023002 (2011).

[63] J.-H. Im, C.-R. Lee, J.-W. Lee, S.-W. Park, N.-G. Park, 6.5% efficient perovskite quantum-dot-sensitized solar cell. *Nanoscale* **3**, 4088-4093 (2011).

[64] S. D. Stranks, G. E. Eperon, G. Grancini, C. Menelaou, M. J. P. Alcocer, T. Leijtens, L. M. Herz, A. Petrozza, H. J. Snaith, Electron-Hole Diffusion Lengths Exceeding 1 Micrometer in an Organometal Trihalide Perovskite Absorber. *Science* **342**, 341-344 (2013).

[65] C. Wehrenfennig, G. E. Eperon, M. B. Johnston, H. J. Snaith, L. M. Herz, High charge carrier mobilities and lifetimes in organolead trihalide perovskites. *Adv. Mater.* **26**, 1584–1589 (2014).

[66] V. D'Innocenzo, G. Grancini, M. J. P. Alcocer, A. R. S. Kandada, S. D. Stranks, M. M. Lee, G. Lanzani, H. J. Snaith, A. Petrozza, Excitons versus free charges in organo-lead tri-halide perovskites. *Nat. Commun.* **5**, (2014), DOI:10.1038/ncomms4586.

[67] M. M. Lee, J. Teuscher, T. Miyasaka, T. N. Murakami, H. J. Snaith, Efficient Hybrid Solar Cells Based on Meso-Superstructured Organometal Halide Perovskites. *Science* **338**, 643-647 (2012).

[68] J. Burschka, N. Pellet, S.-J. Moon, R. Humphry-Baker, P. Gao, M. K. Nazeeruddin, M. Gratzel, Sequential deposition as a route to high-performance perovskite-sensitized solar cells. *Nature* **499**, 316-319 (2013).

[69] W. S. Yang, J. H. Noh, N. J. Jeon, Y. C. Kim, S. Ryu, J. Seo, S. I. Seok, High-performance photovoltaic perovskite layers fabricated through intramolecular exchange. *Science* **348**, 1234-1237 (2015).

[70] H. Zhou, Q. Chen, G. Li, S. Luo, T.-b. Song, H.-S. Duan, Z. Hong, J. You, Y. Liu, Y. Yang, Interface engineering of highly efficient perovskite solar cells. *Science* **345**, 542-546 (2014).

[71] N. J. Jeon, J. H. Noh, W. S. Yang, Y. C. Kim, S. Ryu, J. Seo, S. I. Seok, Compositional engineering of perovskite materials for high-performance solar cells. *Nature* **517**, 476-480 (2015).

[72] V. Gonzalez-Pedro, E. J. Juarez-Perez, W.-S. Arsyad, E. M. Barea, F. Fabregat-Santiago, I. Mora-Sero, J. Bisquert, General Working Principles of CH3NH3PbX3 Perovskite Solar Cells. *Nano Lett.* **14**, 888-893 (2014).

[73] D. Liu, T. L. Kelly, Perovskite solar cells with a planar heterojunction structure prepared using room-temperature solution processing techniques. *Nat. Photonics* **8**, 133-138 (2014).

[74] B. Conings, L. Baeten, C. De Dobbelaere, J. D'Haen, J. Manca, H.-G. Boyen, Perovskite-Based Hybrid Solar Cells Exceeding 10% Efficiency with High Reproducibility Using a Thin Film Sandwich Approach. *Adv. Mater.* **26**, 2041-2046 (2014).

[75] J. H. Heo, S. H. Im, J. H. Noh, T. N. Mandal, C.-S. Lim, J. A. Chang, Y. H. Lee, H.-j. Kim, A. Sarkar, K. NazeeruddinMd, M. Gratzel, S. I. Seok, Efficient inorganic-organic hybrid heterojunction solar cells containing perovskite compound and polymeric hole conductors. *Nat. Photonics* **7**, 486-491 (2013).

[76] J.-Y. Jeng, Y.-F. Chiang, M.-H. Lee, S.-R. Peng, T.-F. Guo, P. Chen, T.-C. Wen, CH3NH3PbI3 Perovskite/Fullerene Planar-Heterojunction Hybrid Solar Cells. *Adv. Mater.* **25**, 3727-3732 (2013).

[77] P. Docampo, J. M. Ball, M. Darwich, G. E. Eperon, H. J. Snaith, Efficient organometal trihalide perovskite planar-heterojunction solar cells on flexible polymer substrates. *Nat. Commun.* **4**, (2013), DOI:10.1038/ncomms3761.

[78] J. H. Kim, S. T. Williams, N. Cho, C.-C. Chueh, A. K. Y. Jen, Enhanced Environmental Stability of Planar Heterojunction Perovskite Solar Cells Based on Blade-Coating. *Adv. Energy Mater.* **5**, (2015), DOI: 10.1002/aenm.201401229.

[79] Y. Chen, T. Chen, L. Dai, Layer-by-Layer Growth of $CH_3NH_3PbI_{3-x}Cl_x$ for Highly Efficient Planar Heterojunction Perovskite Solar Cells. *Adv. Mater.* **27**, 1053-1059 (2015).

[80] W. Nie, H. Tsai, R. Asadpour, J.-C. Blancon, A. J. Neukirch, G. Gupta, J. J. Crochet, M. Chhowalla, S. Tretiak, M. A. Alam, H.-L. Wang, A. D. Mohite, High-efficiency solution-processed perovskite solar cells with millimeter-scale grains. *Science* **347**, 522-525 (2015).

[81] H.-S. Kim, N.-G. Park, Parameters Affecting I–V Hysteresis of $CH_3NH_3PbI_3$ Perovskite Solar Cells: Effects of Perovskite Crystal Size and Mesoporous TiO_2 Layer. *J. Phys. Chem. Lett.* **5**, 2927-2934 (2014).

[82] H. J. Snaith, A. Abate, J. M. Ball, G. E. Eperon, T. Leijtens, N. K. Noel, S. D. Stranks, J. T.-W. Wang, K. Wojciechowski, W. Zhang, Anomalous Hysteresis in Perovskite Solar Cells. *J. Phys. Chem. Lett.* **5**, 1511-1515 (2014).

[83] C. Bi, Y. Yuan, Y. Fang, J. Huang, Low-Temperature Fabrication of Efficient Wide-Bandgap Organolead Trihalide Perovskite Solar Cells. *Adv. Energy Mater.* **5**, (2015), DOI: 10.1002/aenm.201401616.

[84] J. H. Noh, S. H. Im, J. H. Heo, T. N. Mandal, S. I. Seok, Chemical Management for Colorful, Efficient, and Stable Inorganic–Organic Hybrid Nanostructured Solar Cells. *Nano Lett.* **13**, 1764-1769 (2013).

[85] N. K. Noel, S. D. Stranks, A. Abate, C. Wehrenfennig, S. Guarnera, A.-A. Haghighirad, A. Sadhanala, G. E. Eperon, S. K. Pathak, M. B. Johnston, A. Petrozza, L. M. Herz, H. J. Snaith, Lead-free organic-inorganic tin halide perovskites for photovoltaic applications. *Energy Environ. Sci.* **7**, 3061-3068 (2014).

[86] F. Hao, C. C. Stoumpos, D. H. Cao, R. P. H. Chang, M. G. Kanatzidis, Lead-free solid-state organic-inorganic halide perovskite solar cells. *Nat. Photonics* **8**, 489-494 (2014).

[87] Z. Xu, L.-M. Chen, G. Yang, C.-H. Huang, J. Hou, Y. Wu, G. Li, C.-S. Hsu, Y. Yang, Vertical Phase Separation in Poly(3-hexylthiophene): Fullerene Derivative Blends and its Advantage for Inverted Structure Solar Cells. *Adv. Funct. Mater.* **19**, 1227-1234 (2009).

[88] C.-H. Hsieh, Y.-J. Cheng, P.-J. Li, C.-H. Chen, M. Dubosc, R.-M. Liang, C.-S. Hsu, Highly Efficient and Stable Inverted Polymer Solar Cells Integrated with a Cross-Linked Fullerene Material as an Interlayer. *J. Am. Chem. Soc.* **132**, 4887-4893 (2010).

[89] M. T. Dang, L. Hirsch, G. Wantz, P3HT:PCBM, Best Seller in Polymer Photovoltaic Research. *Adv. Mater.* **23**, 3597-3602 (2011).

[90] S. K. Hau, H.-L. Yip, N. S. Baek, J. Zou, K. O'Malley, A. K.-Y. Jen, Air-stable inverted flexible polymer solar cells using zinc oxide nanoparticles as an electron selective layer. *Appl. Phys. Lett.* **92**, 253301 (2008).

[91] C. Waldauf, M. Morana, P. Denk, P. Schilinsky, K. Coakley, S. A. Choulis, C. J. Brabec, Highly efficient inverted organic photovoltaics using solution based titanium oxide as electron selective contact. *Appl. Phys. Lett.* **89**, 233517 (2006).

[92] S. K. Hau, H.-L. Yip, O. Acton, N. S. Baek, H. Ma, A. K. Y. Jen, Interfacial modification to improve inverted polymer solar cells. *J. Mater. Chem.* **18**, 5113-5119 (2008).

[93] B. Zhao, Z. He, X. Cheng, D. Qin, M. Yun, M. Wang, X. Huang, J. Wu, H. Wu, Y. Cao, Flexible polymer solar cells with power conversion efficiency of 8.7%. *J. Mater. Chem. C* **2**, 5077-5082 (2014).

[94] S. Das, J. K. Keum, J. F. Browning, G. Gu, B. Yang, O. Dyck, C. Do, W. Chen, J. Chen, I. N. Ivanov, K. Hong, A. J. Rondinone, P. C. Joshi, D. B. Geohegan, G. Duscher, K. Xiao, Correlating high power conversion efficiency of PTB7:PC$_{71}$BM inverted organic solar cells with nanoscale structures. *Nanoscale* **7**, 15576-15583 (2015).

[95] B. Yang, Y. Yuan, J. Huang, Reduced Bimolecular Charge Recombination Loss in Thermally Annealed Bilayer Heterojunction Photovoltaic Devices with Large External Quantum Efficiency and Fill Factor. *The Journal of Physical Chemistry C* **118**, 5196-5202 (2014).

[96] J. K. Keum, K. Xiao, I. N. Ivanov, K. Hong, J. F. Browning, G. S. Smith, M. Shao, K. C. Littrell, A. J. Rondinone, E. Andrew Payzant, J. Chen, D. K. Hensley, Solvent quality-induced nucleation and growth of parallelepiped nanorods in dilute poly(3-hexylthiophene) (P3HT) solution and the impact on the crystalline morphology of solution-cast thin film. *CrystEngComm* **15**, 1114-1124 (2013).

[97] M. Shao, J. K. Keum, R. Kumar, J. Chen, J. F. Browning, S. Das, W. Chen, J. Hou, C. Do, K. C. Littrell, A. Rondinone, D. B. Geohegan, B. G. Sumpter, K. Xiao, Understanding How Processing Additives Tune the Nanoscale Morphology of High Efficiency Organic Photovoltaic Blends: From Casting Solution to Spun-Cast Thin Film. *Adv. Funct. Mater.* **24**, 6647-6657 (2014).

[98] S. J. Lou, J. M. Szarko, T. Xu, L. Yu, T. J. Marks, L. X. Chen, Effects of Additives on the Morphology of Solution Phase Aggregates Formed by Active Layer Components of High-Efficiency Organic Solar Cells. *J. Am. Chem. Soc.* **133**, 20661-20663 (2011).

[99] M. R. Hammond, R. J. Kline, A. A. Herzing, L. J. Richter, D. S. Germack, H.-W. Ro, C. L. Soles, D. A. Fischer, T. Xu, L. Yu, M. F. Toney, D. M. DeLongchamp, Molecular Order in High-Efficiency Polymer/Fullerene Bulk Heterojunction Solar Cells. *ACS Nano* **5**, 8248-8257 (2011).

[100] H. Lu, B. Akgun, T. P. Russell, Morphological Characterization of a Low-Bandgap Crystalline Polymer:PCBM Bulk Heterojunction Solar Cells. *Adv. Energy Mater.* **1**, 870-878 (2011).

[101] L. G. Parratt, Surface Studies of Solids by Total Reflection of X-Rays. *Phys. Rev.* **95**, 359-369 (1954).

[102] B. A. Collins, Z. Li, J. R. Tumbleston, E. Gann, C. R. McNeill, H. Ade, Absolute Measurement of Domain Composition and Nanoscale Size Distribution Explains Performance in PTB7:PC71BM Solar Cells. *Adv. Energy Mater.* **3**, 65-74 (2013).

[103] G. He, Z. Li, X. Wan, J. Zhou, G. Long, S. Zhang, M. Zhang, Y. Chen, Efficient small molecule bulk heterojunction solar cells with high fill factors via introduction of π-stacking moieties as end group. *J. Mater. Chem. A* **1**, 1801-1809 (2013).

[104] A. K. K. Kyaw, D. H. Wang, V. Gupta, W. L. Leong, L. Ke, G. C. Bazan, A. J. Heeger, Intensity Dependence of Current–Voltage Characteristics and Recombination in High-Efficiency Solution-Processed Small-Molecule Solar Cells. *ACS Nano* **7**, 4569-4577 (2013).

[105] J. Zhou, Y. Zuo, X. Wan, G. Long, Q. Zhang, W. Ni, Y. Liu, Z. Li, G. He, C. Li, B. Kan, M. Li, Y. Chen, Solution-Processed and High-Performance Organic Solar Cells Using Small Molecules with a Benzodithiophene Unit. *J. Am. Chem. Soc.* **135**, 8484-8487 (2013).

[106] B. Walker, C. Kim, T.-Q. Nguyen, Small Molecule Solution-Processed Bulk Heterojunction Solar Cells. *Chem. Mater.* **23**, 470-482 (2011).

[107] A. Mishra, P. Bäuerle, Small Molecule Organic Semiconductors on the Move: Promises for Future Solar Energy Technology. *Angew. Chem. Int. Ed.* **51**, 2020-2067 (2012).

[108] J. Zhou, X. Wan, Y. Liu, Y. Zuo, Z. Li, G. He, G. Long, W. Ni, C. Li, X. Su, Y. Chen, Small Molecules Based on Benzo[1,2-b:4,5-b′]dithiophene Unit for High-Performance Solution-Processed Organic Solar Cells. *J. Am. Chem. Soc.* **134**, 16345-16351 (2012).

[109] L.-C. Chi, H.-F. Chen, W.-Y. Hung, Y.-H. Hsu, P.-C. Feng, S.-H. Chou, Y.-H. Liu, K.-T. Wong, Donor-acceptor small molecule with coplanar and rigid π-bridge for efficient organic solar cells. *Sol. Energy Mater. Sol. Cells* **109**, 33-39 (2013).

[110] Y. Lin, Y. Li, X. Zhan, Small molecule semiconductors for high-efficiency organic photovoltaics. *Chem. Soc. Rev.* **41**, 4245-4272 (2012).

[111] A. Viterisi, N. F. Montcada, C. V. Kumar, F. Gispert-Guirado, E. Martin, E. Escudero, E. Palomares, Unambiguous determination of molecular packing in crystalline donor domains of small molecule solution processed solar cell devices using routine X-ray diffraction techniques. *J. Mater. Chem. A* **2**, 3536-3542 (2014).

[112] O. K. Kwon, J.-H. Park, D. W. Kim, S. K. Park, S. Y. Park, An All-Small-Molecule Organic Solar Cell with High Efficiency Nonfullerene Acceptor. *Adv. Mater.* **27**, 1951-1956 (2015).

[113] N. Herath, S. Das, J. K. Keum, J. Zhu, R. Kumar, I. N. Ivanov, B. G. Sumpter, J. F. Browning, K. Xiao, G. Gu, P. Joshi, S. Smith, V. Lauter, Peculiarity of Two Thermodynamically-Stable Morphologies and Their Impact on the Efficiency of Small Molecule Bulk Heterojunction Solar Cells. *Sci. Rep.* **5**, 13407 (2015).

[114] W. Ma, J. R. Tumbleston, L. Ye, C. Wang, J. Hou, H. Ade, Quantification of Nano- and Mesoscale Phase Separation and Relation to Donor and Acceptor Quantum Efficiency, Jsc, and FF in Polymer:Fullerene Solar Cells. *Adv. Mater.* **26**, 4234-4241 (2014).

[115] S. Sweetnam, K. R. Graham, G. O. Ngongang Ndjawa, T. Heumüller, J. A. Bartelt, T. M. Burke, W. Li, W. You, A. Amassian, M. D. McGehee, Characterization of the Polymer Energy Landscape in Polymer:Fullerene Bulk Heterojunctions with Pure and Mixed Phases. *J. Am. Chem. Soc.* **136**, 14078-14088 (2014).

[116] P. H. Wöbkenberg, D. D. C. Bradley, D. Kronholm, J. C. Hummelen, D. M. de Leeuw, M. Cölle, T. D. Anthopoulos, High mobility n-channel organic field-effect transistors based on soluble C60 and C70 fullerene derivatives. *Synth. Met.* **158**, 468-472 (2008).

[117] J. W. Kiel, M. E. Mackay, B. J. Kirby, B. B. Maranville, C. F. Majkrzak, Phase-sensitive neutron reflectometry measurements applied in the study of photovoltaic films. *J. Chem. Phys.* **133**, 074902 (2010).

[118] Z. Sun, K. Xiao, J. K. Keum, X. Yu, K. Hong, J. Browning, I. N. Ivanov, J. Chen, J. Alonzo, D. Li, B. G. Sumpter, E. A. Payzant, C. M. Rouleau, D. B. Geohegan, PS-b-P3HT Copolymers as P3HT/PCBM Interfacial Compatibilizers for High Efficiency Photovoltaics. *Adv. Mater.* **23**, 5529-5535 (2011).

[119] J. W. Kiel, B. J. Kirby, C. F. Majkrzak, B. B. Maranville, M. E. Mackay, Nanoparticle concentration profile in polymer-based solar cells. *Soft Matter* **6**, 641-646 (2010).

[120] Li, W. *et al.* The Effect of additive on performance and shelf-stability of HSX-1/PCBM photovoltaic devices. *Organ. Elect.* **12**, 1544-1551 (2011).

[121] W. L. Leong, G. C. Welch, J. Seifter, J. H. Seo, G. C. Bazan, A. J. Heeger, Understanding the Role of Thermal Processing in High Performance Solution Processed Small Molecule Bulk Heterojunction Solar Cells. *Adv. Energy Mater.* **3**, 356-363 (2013).

[122] P. A. Staniec, A. J. Parnell, A. D. F. Dunbar, H. Yi, A. J. Pearson, T. Wang, P. E. Hopkinson, C. Kinane, R. M. Dalgliesh, A. M. Donald, A. J. Ryan, A. Iraqi, R. A. L. Jones, D. G. Lidzey, The Nanoscale Morphology of a PCDTBT:PCBM Photovoltaic Blend. *Adv. Energy Mater.* **1**, 499-504 (2011).

[123] F. C. Spano, The Spectral Signatures of Frenkel Polarons in H- and J-Aggregates. *Acc. Chem. Res.* **43**, 429-439 (2010).

[124] L. A. Perez, K. W. Chou, J. A. Love, T. S. van der Poll, D.-M. Smilgies, T.-Q. Nguyen, E. J. Kramer, A. Amassian, G. C. Bazan, Solvent Additive Effects on Small Molecule Crystallization in Bulk Heterojunction Solar Cells Probed During Spin Casting. *Adv. Mater.* **25**, 6380-6384 (2013).

[125] U. Rau, Reciprocity relation between photovoltaic quantum efficiency and electroluminescent emission of solar cells. *Phys. Rev. B* **76**, 085303 (2007).

[126] C.-W. Chen, H.-W. Kang, S.-Y. Hsiao, P.-F. Yang, K.-M. Chiang, H.-W. Lin, Efficient and Uniform Planar-Type Perovskite Solar Cells by Simple Sequential Vacuum Deposition. *Adv. Mater.* **26**, 6647-6652 (2014).

[127] O. Malinkiewicz, A. Yella, Y. H. Lee, G. M. Espallargas, M. Graetzel, M. K. Nazeeruddin, H. J. Bolink, Perovskite solar cells employing organic charge-transport layers. *Nat. Photonics* **8**, 128-132 (2014).

[128] G. E. Eperon, V. M. Burlakov, P. Docampo, A. Goriely, H. J. Snaith, Morphological Control for High Performance, Solution-Processed Planar Heterojunction Perovskite Solar Cells. *Adv. Funct. Mater.* **24**, 151-157 (2014).

[129] Z. Xiao, Q. Dong, C. Bi, Y. Shao, Y. Yuan, J. Huang, Solvent Annealing of Perovskite-Induced Crystal Growth for Photovoltaic-Device Efficiency Enhancement. *Adv. Mater.* **26**, 6503-6509 (2014).

[130] Q. Chen, H. Zhou, Z. Hong, S. Luo, H.-S. Duan, H.-H. Wang, Y. Liu, G. Li, Y. Yang, Planar Heterojunction Perovskite Solar Cells via Vapor-Assisted Solution Process. *J. Am. Chem. Soc.* **136**, 622-625 (2014).

[131] H. Sirringhaus, T. Kawase, R. H. Friend, T. Shimoda, M. Inbasekaran, W. Wu, E. P. Woo, High-Resolution Inkjet Printing of All-Polymer Transistor Circuits. *Science* **290**, 2123-2126 (2000).

[132] K. X. Steirer, M. O. Reese, B. L. Rupert, N. Kopidakis, D. C. Olson, R. T. Collins, D. S. Ginley, Ultrasonic spray deposition for production of organic solar cells. *Sol. Energy Mater. Sol. Cells* **93**, 447-453 (2009).

[133] F. C. Krebs, S. A. Gevorgyan, J. Alstrup, A roll-to-roll process to flexible polymer solar cells: model studies, manufacture and operational stability studies. *J. Mater. Chem.* **19**, 5442-5451 (2009).

[134] Z. Wei, H. Chen, K. Yan, S. Yang, Inkjet Printing and Instant Chemical Transformation of a $CH_3NH_3PbI_3$/Nanocarbon Electrode and Interface for Planar Perovskite Solar Cells. *Angew. Chem.* **126**, 13455-13459 (2014).

[135] D. Vak, K. Hwang, A. Faulks, Y.-S. Jung, N. Clark, D-Y. Kim, G. J. Wilson, S. E. Watkins, 3D Printer Based Slot-Die Coater as a Lab-to-Fab Translation Tool for Solution-Processed Solar Cells. *Adv. Energy Mater.* **5**, (2015), DOI: 10.1002/aenm.201401539.

[136] C. N. Hoth, S. A. Choulis, P. Schilinsky, C. J. Brabec, High Photovoltaic Performance of Inkjet Printed Polymer:Fullerene Blends. *Adv. Mater.* **19**, 3973-3978 (2007).

[137] C. N. Hoth, P. Schilinsky, S. A. Choulis, C. J. Brabec, Printing Highly Efficient Organic Solar Cells. *Nano Lett.* **8**, 2806-2813 (2008).

[138] J. Ju, Y. Yamagata, T. Higuchi, Thin-Film Fabrication Method for Organic Light-Emitting Diodes Using Electrospray Deposition. *Adv. Mater.* **21**, 4343-4347 (2009).

[139] R. C. Tenent, T. M. Barnes, J. D. Bergeson, A. J. Ferguson, B. To, L. M. Gedvilas, M. J. Heben, J. L. Blackburn, Ultrasmooth, Large-Area, High-Uniformity, Conductive Transparent Single-Walled-Carbon-Nanotube Films for Photovoltaics Produced by Ultrasonic Spraying. *Adv. Mater.* **21**, 3210-3216 (2009).

[140] C. Girotto, D. Moia, B. P. Rand, P. Heremans, High-Performance Organic Solar Cells with Spray-Coated Hole-Transport and Active Layers. *Adv. Funct. Mater.* **21**, 64-72 (2011).

[141] S. F. Tedde, J. Kern, T. Sterzl, J. Fürst, P. Lugli, O. Hayden, Fully Spray Coated Organic Photodiodes. *Nano Lett.* **9**, 980-983 (2009).

[142] M. Shao, S. Das, K. Xiao, J. Chen, J. K. Keum, I. N. Ivanov, G. Gu, W. Durant, D. Li, D. B. Geohegan, High-performance organic field-effect transistors with dielectric and active layers printed sequentially by ultrasonic spraying. *J. Mater. Chem. C* **1**, 4384-4390 (2013).

[143] M. Lefort, G. Popa, E. Seyrek, R. Szamocki, O. Felix, J. Hemmerlé, L. Vidal, J.-C. Voegel, F. Boulmedais, G. Decher, P. Schaaf, Spray-On Organic/Inorganic Films: A General Method for the Formation of Functional Nano- to Microscale Coatings. *Angew. Chem. Int. Ed.* **49**, 10110-10113 (2010).

[144] T. Ishikawa, M. Nakamura, K. Fujita, T. Tsutsui, Preparation of organic bulk heterojunction photovoltaic cells by evaporative spray deposition from ultradilute solution. *Appl. Phys. Lett.* **84**, 2424-2426 (2004).

[145] A. T. Barrows, A. J. Pearson, C. K. Kwak, A. D. F. Dunbar, A. R. Buckley, D. G. Lidzey, Efficient planar heterojunction mixed-halide perovskite solar cells deposited via spray-deposition. *Energy Environ. Sci.* **7**, 2944-2950 (2014).

[146] S. Das, B. Yang, G. Gu, P. C. Joshi, I. N. Ivanov, C. M. Rouleau, T. Aytug, D. B. Geohegan, K. Xiao, High-Performance Flexible Perovskite Solar Cells by Using a Combination of Ultrasonic Spray-Coating and Low Thermal Budget Photonic Curing. *ACS Photonics* **2**, 680-686 (2015).

[147] M. Xiao, F. Huang, W. Huang, Y. Dkhissi, Y. Zhu, J. Etheridge, A. Gray-Weale, U. Bach, Y.-B. Cheng, L. Spiccia, A Fast Deposition-Crystallization Procedure for Highly Efficient Lead Iodide Perovskite Thin-Film Solar Cells. *Angew. Chem.* **126**, 10056-10061 (2014).

[148] K. Wojciechowski, S. D. Stranks, A. Abate, G. Sadoughi, A. Sadhanala, N. Kopidakis, G. Rumbles, C.-Z. Li, R. H. Friend, A. K. Y. Jen, H. J. Snaith, Heterojunction Modification for Highly Efficient Organic–Inorganic Perovskite Solar Cells. *ACS Nano* **8**, 12701-12709 (2014).

[149] W. H. Nguyen, C. D. Bailie, E. L. Unger, M. D. McGehee, Enhancing the Hole-Conductivity of Spiro-OMeTAD without Oxygen or Lithium Salts by Using Spiro(TFSI)$_2$ in Perovskite and Dye-Sensitized Solar Cells. *J. Am. Chem. Soc.* **136**, 10996-11001 (2014).

[150] J. D. K. Rivard, A. S. Sabau, C. A. Blue, E. K. Ohriner, N. Jayaraman, Thermophysical properties of roll-compacted nickel sheet for high-density infrared sheet fabrication. *Metall. Mater. Trans. A* **34**, 3043-3054 (2003).

[151] A. Sabau, P. Kadolkar, R. Dinwiddie, R. Ott, C. Blue, Process Parameters for Infrared Processing of FePt Nanoparticle Films. *Metall. Mater. Trans. A* **38**, 788-797 (2007).

[152] B. Yang, O. Dyck, J. Poplawsky, J. Keum, A. Puretzky, S. Das, I. Ivanov, C. Rouleau, G. Duscher, D. Geohegan, K. Xiao, Perovskite Solar Cells with Near 100% Internal Quantum Efficiency Based on Large Single Crystalline Grains and Vertical Bulk Heterojunctions. *J. Am. Chem. Soc.* **137**, 9210-9213 (2015).

[153] T. Leijtens, G. E. Eperon, S. Pathak, A. Abate, M. M. Lee, H. J. Snaith, Overcoming ultraviolet light instability of sensitized TiO$_2$ with meso-superstructured organometal tri-halide perovskite solar cells. *Nat. Commun.* **4**, (2013), DOI:10.1038/ncomms3885.

[154] B. Wu, K. Fu, N. Yantara, G. Xing, S. Sun, T. C. Sum, N. Mathews, Charge Accumulation and Hysteresis in Perovskite-Based Solar Cells: An Electro-Optical Analysis. *Adv. Energy. Mat.* **5**, (2015), DOI: 10.1002/aenm.201500829.

[155] Y. Kutes, L. Ye, Y. Zhou, S. Pang, B. D. Huey, N. P. Padture, Direct Observation of Ferroelectric Domains in Solution-Processed CH$_3$NH$_3$PbI$_3$ Perovskite Thin Films. *J. Phys. Chem. Lett.* **5**, 3335-3339 (2014).

[156] E. L. Unger, E. T. Hoke, C. D. Bailie, W. H. Nguyen, A. R. Bowring, T. Heumuller, M. G. Christoforo, M. D. McGehee, Hysteresis and transient behavior in current-voltage measurements of hybrid-perovskite absorber solar cells. *Energy Environ. Sci.* **7**, 3690-3698 (2014).

[157] S. Pathak, A. Sepe, A. Sadhanala, F. Deschler, A. Haghighirad, N. Sakai, K. C. Goedel, S. D. Stranks, N. Noel, M. Price, S. Hüttner, N. A. Hawkins, R. H. Friend, U. Steiner, H. J. Snaith, Atmospheric Influence upon Crystallization and Electronic Disorder and Its Impact on the Photophysical Properties of Organic–Inorganic Perovskite Solar Cells. *ACS Nano* **9**, 2311-2320 (2015).

[158] J. You, Y. Yang, Z. Hong, T.-B. Song, L. Meng, Y. Liu, C. Jiang, H. Zhou, W.-H. Chang, G. Li, Y. Yang, Moisture assisted perovskite film growth for high performance solar cells. *Appl. Phys. Lett.* **105**, 183902 (2014).

[159] H. Yan, Z. Chen, Y. Zheng, C. Newman, J. R. Quinn, F. Dotz, M. Kastler, A. Facchetti, A high-mobility electron-transporting polymer for printed transistors. *Nature* **457**, 679-686 (2009).

[160] H. N. Tsao, D. M. Cho, I. Park, M. R. Hansen, A. Mavrinskiy, D. Y. Yoon, R. Graf, W. Pisula, H. W. Spiess, K. Müllen, Ultrahigh Mobility in Polymer Field-Effect Transistors by Design. *J. Am. Chem. Soc.* **133**, 2605-2612 (2011).

[161] H. Minemawari, T. Yamada, H. Matsui, J. Tsutsumi, S. Haas, R. Chiba, R. Kumai, T. Hasegawa, *Nature* 2011, **475**, 364-367.

[162] G. H. Gelinck, H. E. A. Huitema, E. van Veenendaal, E. Cantatore, L. Schrijnemakers, J. B. P. H. van der Putten, T. C. T. Geuns, M. Beenhakkers, J. B. Giesbers, B.-H. Huisman, E. J. Meijer, E. M. Benito, F. J. Touwslager, A. W. Marsman, B. J. E. van Rens, D. M. de Leeuw, Flexible active-matrix displays and shift registers based on solution-processed organic transistors. *Nat. Mater.* **3**, 106-110 (2004).

[163] T. Sekitani, T. Yokota, U. Zschieschang, H. Klauk, S. Bauer, K. Takeuchi, M. Takamiya, T. Sakurai, T. Someya, Organic Nonvolatile Memory Transistors for Flexible Sensor Arrays. *Science* **326**, 1516-1519 (2009).

[164] L. Li, L. Jiang, W. Wang, C. Du, H. Fuchs, W. Hu, L. Chi, High-Performance and Stable Organic Transistors and Circuits with Patterned Polypyrrole Electrodes. *Adv. Mater.* **24**, 2159-2164 (2012).

[165] J. Li, Y. Zhao, H. S. Tan, Y. Guo, C.-A. Di, G. Yu, Y. Liu, M. Lin, S. H. Lim, Y. Zhou, H. Su, B. S. Ong, A stable solution-processed polymer semiconductor with record high-mobility for printed transistors. *Sci. Rep.* **2**, 754 (2012).

[166] A. Lv, S. R. Puniredd, J. Zhang, Z. Li, H. Zhu, W. Jiang, H. Dong, Y. He, L. Jiang, Y. Li, W. Pisula, Q. Meng, W. Hu, Z. Wang, High Mobility, Air Stable, Organic Single Crystal Transistors of an n-Type Diperylene Bisimide. *Adv. Mater.* **24**, 2626-2630 (2012).

[167] P. F. Moonen, I. Yakimets, J. Huskens, Fabrication of Transistors on Flexible Substrates: from Mass-Printing to High-Resolution Alternative Lithography Strategies. *Adv. Mater.* **24**, 5526-5541 (2012).

[168] N. Stutzmann, R. H. Friend, H. Sirringhaus, Self-Aligned, Vertical-Channel, Polymer Field-Effect Transistors. *Science* **299**, 1881-1884 (2003).

[169] G. Giri, E. Verploegen, S. C. B. Mannsfeld, S. Atahan-Evrenk, D. H. Kim, S. Y. Lee, H. A. Becerril, A. Aspuru-Guzik, M. F. Toney, Z. Bao, Tuning charge transport in solution-sheared organic semiconductors using lattice strain. *Nature* **480**, 504-508 (2011).

[170] T. L. Breen, P. M. Fryer, R. W. Nunes, M. E. Rothwell, Patterning Indium Tin Oxide and Indium Zinc Oxide Using Microcontact Printing and Wet Etching. *Langmuir* **18**, 194-197 (2002).

[171] A. Abdellah, B. Fabel, P. Lugli, G. Scarpa, Spray deposition of organic semiconducting thin-films: Towards the fabrication of arbitrary shaped organic electronic devices. *Org. Electron.* **11**, 1031-1038 (2010).

[172] K. Xiao, Y. Liu, T. Qi, W. Zhang, F. Wang, J. Gao, W. Qiu, Y. Ma, G. Cui, S. Chen, X. Zhan, G. Yu, J. Qin, W. Hu, D. Zhu, A Highly π-Stacked Organic Semiconductor for Field-Effect Transistors Based on Linearly Condensed Pentathienoacene. *J. Am. Chem. Soc.* **127**, 13281-13286 (2005).

[173] J. E. Anthony, Functionalized Acenes and Heteroacenes for Organic Electronics. *Chem. Rev.* **106**, 5028-5048 (2006).

[174] S. K. Park, T. N. Jackson, J. E. Anthony, D. A. Mourey, High mobility solution processed 6,13-bis(triisopropyl-silylethynyl) pentacene organic thin film transistors. *Appl. Phys. Lett.* **91**, 063514 (2007).

[175] J. A. Lim, W. H. Lee, H. S. Lee, J. H. Lee, Y. D. Park, K. Cho, Self-Organization of Ink-jet-Printed Triisopropylsilylethynyl Pentacene via Evaporation-Induced Flows in a Drying Droplet. *Adv. Funct. Mater.* **18**, 229-234 (2008).

[176] S. C. B. Mannsfeld, M. L. Tang, Z. Bao, Thin Film Structure of Triisopropylsilylethynyl-Functionalized Pentacene and Tetraceno[2,3-b]thiophene from Grazing Incidence X-Ray Diffraction. *Adv. Mater.* **23**, 127-131 (2011).

[177] J. Chen, C. K. Tee, M. Shtein, J. Anthony, D. C. Martin, Grain-boundary-limited charge transport in solution-processed 6,13 bis(tri-isopropylsilylethynyl) pentacene thin film transistors. *J. Appl. Phys.* **103**, 114513 (2008).

[178] C. S. Kim, S. Lee, E. D. Gomez, J. E. Anthony, Y.-L. Loo, Solvent-dependent electrical characteristics and stability of organic thin-film transistors with drop cast bis(triisopropylsilylethynyl) pentacene. *Appl. Phys. Lett.* **93**, 103302 (2008).

[179] K. Lee, J. Kim, K. Shin, Y. S. Kim, Micropatterned crystalline organic semiconductors via direct pattern transfer printing with PDMS stamp. *J. Mater. Chem.* **22**, 22763-22768 (2012).

[180] M. Halik, H. Klauk, U. Zschieschang, G. Schmid, W. Radlik, W. Weber, Polymer Gate Dielectrics and Conducting-Polymer Contactsfor High-Performance Organic Thin-Film Transistors. *Adv. Mater.* **14**, 1717-1722 (2002).

[181] H. Y. Noh, Y. G. Seol, N.-E. Lee, Improved electrical stability in cyclically bent organic thin film transistors with nanocomposite gate dielectrics and surface passivation. *Appl. Phys. Lett.* **95**, 113302 (2009).

[182] T. Sekitani, U. Zschieschang, H. Klauk, T. Someya, Flexible organic transistors and circuits with extreme bending stability. *Nat. Mater.* **9**, 1015-1022 (2010).

[183] Y. S. Chung, N. Shin, J. Kang, Y. Jo, V. M. Prabhu, S. K. Satija, R. J. Kline, D. M. DeLongchamp, M. F. Toney, M. A. Loth, B. Purushothaman, J. E. Anthony, D. Y. Yoon, Zone-Refinement Effect in Small Molecule−Polymer Blend Semiconductors for Organic Thin-Film Transistors. *J. Am. Chem. Soc.* **133**, 412-415 (2011).

[184] S. Y. Cho, J. M. Ko, J. Lim, J. Y. Lee, C. Lee, Inkjet-printed organic thin film transistors based on TIPS pentacene with insulating polymers. *J. Mater. Chem. C* **1**, 914-923 (2013).

[185] J. Smith, M. Heeney, I. McCulloch, J. N. Malik, N. Stingelin, D. D. C. Bradley, T. D. Anthopoulos, Percolation behaviour in high mobility p-channel polymer/small-molecule blend organic field-effect transistors. *Org. Electron.* **12**, 143-147 (2011).

[186] M.-B. Madec, D. Crouch, G. R. Llorente, T. J. Whittle, M. Geoghegan, S. G. Yeates, Organic field effect transistors from ambient solution processed low molar mass semiconductor-insulator blends. *J. Mater. Chem.* **18**, 3230-3236 (2008).

[187] D. K. Hwang, C. Fuentes-Hernandez, J. D. Berrigan, Y. Fang, J. Kim, W. J. Potscavage, H. Cheun, K. H. Sandhage, B. Kippelen, Solvent and polymer matrix effects on TIPS-pentacene/polymer blend organic field-effect transistors. *J. Mater. Chem.* **22**, 5531-5537 (2012).

[188] W. H. Lee, D. Kwak, J. E. Anthony, H. S. Lee, H. H. Choi, D. H. Kim, S. G. Lee, K. Cho, The Influence of the Solvent Evaporation Rate on the Phase Separation and Electrical Performances of Soluble Acene-Polymer Blend Semiconductors. *Adv. Funct. Mater.* **22**, 267-281 (2012).

[189] N. Shin, J. Kang, L. J. Richter, V. M. Prabhu, R. J. Kline, D. A. Fischer, D. M. DeLongchamp, M. F. Toney, S. K. Satija, D. J. Gundlach, B. Purushothaman, J. E. Anthony, D. Y. Yoon, Vertically Segregated Structure and Properties of Small Molecule–Polymer Blend Semiconductors for Organic Thin-Film Transistors. *Adv. Funct. Mater.* **23**, 366-376 (2013).

[190] R. Ruiz, A. Papadimitratos, A. C. Mayer, G. G. Malliaras, Thickness Dependence of Mobility in Pentacene Thin-Film Transistors. *Adv. Mater.* **17**, 1795-1798 (2005).

[191] J. Kang, N. Shin, D. Y. Jang, V. M. Prabhu, D. Y. Yoon, Structure and Properties of Small Molecule−Polymer Blend Semiconductors for Organic Thin Film Transistors. *J. Am. Chem. Soc.* **130**, 12273-12275 (2008).

[192] M.-B. Madec, P. J. Smith, A. Malandraki, N. Wang, J. G. Korvink, S. G. Yeates, Enhanced reproducibility of inkjet printed organic thin film transistors based on solution processable polymer-small molecule blends. *J. Mater. Chem.* **20**, 9155-9160 (2010).

[193] J. M. Torres, C. M. Stafford, D. Uhrig, B. D. Vogt, Impact of chain architecture (branching) on the thermal and mechanical behavior of polystyrene thin films. *J. Polym. Sci., Part B: Polym. Phys.* **50**, 370-377 (2012).

[194] T. Ohe, M. Kuribayashi, R. Yasuda, A. Tsuboi, K. Nomoto, K. Satori, M. Itabashi, J. Kasahara, Solution-processed organic thin-film transistors with vertical nanophase separation. *Appl. Phys. Lett.* **93**, 053303 (2008).

[195] W. E. I. Sha, X. Ren, L. Chen, W. C. H. Choy, The efficiency limit of CH3NH3PbI3 perovskite solar cells. *Appl. Phys. Lett.* **106**, 221104 (2015).

Vita

Sanjib Das was born in Chittagong, a major port city of Bangladesh, and got his B. Sc. degree in electrical and electronic engineering (EEE) from Bangladesh University of Engineering and Technology, Dhaka, Bangladesh in October, 2009.

Sanjib joined Dr. Gong Gu's research group in August, 2011 to pursue PhD at the University of Tennessee (UT). During his PhD, he worked at the Center for Nanophase Materials Sciences (CNMS), Oak Ridge National Laboratory under the joint supervision of Dr. Gong Gu from UT and Dr. Kai Xiao from CNMS. His research interests include emerging organic/hybrid photovoltaics, light emitting diodes, thin film transistors, and two-dimensional materials.